Aus dem Institut für Experimentelle Ultrahochfeld Magnet Resonanz
der Medizinischen Fakultät Charité – Universitätsmedizin Berlin

DISSERTATION

Development of Diffusion Weighted Magnetic Resonance
Methodology and its Application in Renal Imaging

zur Erlangung des akademischen Grades
Doctor rerum medicinalium (Dr. rer. medic.)

vorgelegt der Medizinischen Fakultät
Charité – Universitätsmedizin Berlin

von

João dos Santos Periquito

aus Santarém, Portugal

Datum der Promotion: 26.06.2022

Contents

List of abbreviations

ADC	Apparent diffusion coefficient
AKI	Acute kidney injury
B_0	Static magnetic field
BD	Border displacement
CKD	Chronic kidney disease
COR	Cortex
DW-SE	Diffusion-weighted spin-echo
DWI	Diffusion-weighted imaging
EPI	Echo planar imaging
FLASH	Fast low angle shot
IM	Inner medulla
ITV	Increased tubular volume fraction
IVIM	Intravoxel incoherent motion
LS	Least squares
MAPE	Mean absolute percentage error
MR	Magnetic resonance
MRI	Magnetic resonance imaging
NNLS	Non-negative least squares
OM	Outer medulla
RARE	Rapid acquisition relaxation enhancement
RF	Radio-frequency
ROI	Region of interest
SE	Spin-echo
SI	Signal intensity
SNR	Signal to noise ratio
Ss	Single-shot
T	Tesla
TLCO	Twelve-layer concentric objects

List of Images

Abstract

Introduction

Kidney diseases are a major health issue. To address this clinical need, non-invasive imaging may provide markers to inform on the different stages of pathophysiology.

Diffusion-weighted magnetic resonance imaging (DWI) is a non-invasive imaging technique sensitive to tissue water movement and can be used to differentiate between tissue properties. DWI studies commonly make use of single-shot Echo-Planar Imaging (ss-EPI) techniques that are prone to suffering from geometric distortion. Fast spin-echo imaging techniques (e.g. Rapid Acquisition Relaxation Enhancement - RARE) are less susceptible image distortions and can be an alternative to ss-EPI.

Renal-DWI studies commonly use a mono or bi-exponential signal decay model which does not differentiate between the different water diffusion sources.

Firstly, this thesis focuses in the implementation of a novel image acquisition technique: diffusion sensitized split-echo RARE technique. Secondly, show the feasibility of a novel image analysis approach: continuum modeling, using non-negative least squares (NNLS) for separate the different renal water diffusion sources.

Methods

The *Stejskal-Tanner* preparation was used to introduce diffusion sensitization to a RARE variant to ensure renal-DWI free-of-geometric distortion for high field preclinical DWI at 9.4 T. Validation studies in standard liquids and *in vivo* were performed to validate the implementation of DW split-echo RARE.

Numerical simulations were conducted to gauge the performance of the data-driven NNLS approach using conventional least square fitting (LS) as reference. The simulations aimed at optimizing renal DWI protocols (number of b-values, SNR, b-value range) for separate the different renal water diffusion sources for different physiological conditions (increased tubular volume fraction and fibrosis).

Results

Validation studies provided diffusion coefficients consistent with reported values from the literature.

Split-echo RARE outperformed conventional ss-EPI, with ss-EPI showing a 3.5-times larger border displacement (2.60 vs. 0.75).

NNLS showed the same high degree of reliability as the non-linear LS. Mean absolute percentage error (MAPE) of the tubular volume fraction ($f_{tubules}$) decreased with: increasing SNR, increasing the number of

b-values and using b-range$_{large}$. Fixing D_{blood} and D_{tissue} significantly reduced MAPE$_{ftubules.}$ NNLS was able to detect the (fourth) fibrotic compartment and to distinguish between 10% versus 30% fibrosis.

Conclusion

In this thesis, I demonstrated the feasibility of the split-echo RARE as an alternative to the common ss-EPI technique in DWI studies.

This work demonstrates the feasibility of continuum modelling using NNLS, a data-driven approach for renal DWI to separate the different renal water diffusion sources under different (patho)physiological conditions including increased tubular volume fraction and different degrees of fibrosis.

Zusammenfassung

Einleitung

Nierenerkrankungen sind ein großes Gesundheitsproblem. Um diesen dringenden, ungedeckten klinischen Bedarf zu decken, kann die nicht-invasive Bildgebung Marker liefern, die über die verschiedenen Stadien der Pathophysiologie informieren.

Die Diffusionsgewichtete Bildgebung (DWI) ist ein nicht-invasives Verfahren, das auf die Wasserbewegung im Gewebe reagiert. Die DWI kann zur Differenzierung von Gewebeeigenschafte beitragen.

Bei DWI-Studien werden üblicherweise *single-shot-echo-planar-imaging* (ss-EPI)-Techniken verwendet, die anfällig für geometrische Verzerrungen sind. Schnelle *Spin-Echo*-Bildgebungstechniken (z. B. *Rapid Acquisition Relaxation Enhancement* - RARE) sind weniger anfällig für B_0-Inhomogenitäts-bedingte Bildverzerrungen und können eine gute Alternative zu ss-EPI sein.

Nieren-DWI-Studien verwenden üblicherweise ein mono- oder bi-exponentielles Signalabklingmodell, das nicht zwischen den verschiedenen Wasserdiffusionsquellen unterscheidet.

Diese Arbeit konzentriert sich erstens auf die Implementierung einer neuartigen Bildaufnahmetechnik: die diffusionssensibilisierte *Split-Echo*-RARE-Technik. Zweitens wird die Machbarkeit eines neuartigen Bildanalyseansatzes aufgezeigt: Kontinuumsmodellierung unter Verwendung der *non-negative least squares* (NNLS) zur Trennung der verschiedenen renalen Wasserdiffusionsquellen.

Methoden

Die *Stejskal-Tanner*-Vorbereitung wurde verwendet, um eine Diffusionssensibilisierung in eine *RARE*-Variante einzuführen, die eine Nieren *DWI* frei von geometrischer Verzerrung für präklinisches *DWI* im Hochfeld bei 9.4 T ermöglicht.

Es wurden Validierungsstudien in Standardflüssigkeiten und in vivo durchgeführt, um die Implementierung von *DW Split-Echo RARE* zu validieren.

Es wurden numerische Simulationen durchgeführt, um die Leistung des datengesteuerten NNLS-Ansatzes unter Verwendung der konventionellen *least-square* Anpassung (LS) als Referenz zu bewerten. Die Simulationen zielten darauf ab, die renalen DWI Protokolle (Anzahl der Messpunkte auf dem Signalabfall, *SNR*, *Stärke der letzten Diffusionswichtung*) für die Trennung der verschiedenen renalen Wasserdiffusionsquellen für zwei physiologische Bedingungen zu bewerten.

Ergebnisse

Validierungsstudien lieferten Diffusionskoeffizienten, die mit den berichteten Werten aus der Literatur übereinstimmen.

Die *Split-Echo-RARE* übertraf den konventionellen *ss-EPI*, wobei der *ss-EPI* eine 3.5-mal größere geometrische Verzerrung (2.60 vs. 0.75) hat.

Die *NNLS* zeigte den gleichen hohen Grad an Zuverlässigkeit wie die LS, da sie in der Lage ist, die drei wichtigsten renalen Wasserdiffusionsquellen zu trennen. Der mittlere relative Fehler (*MAPE*) der tubulären Volumenfraktion (f_{tubuli}) nahm mit zunehmendem *SNR* ab. Die Fixierung D_{blood} und D_{tissue} reduzierte die Unsicherheiten der Volumenfraktionen sehr stark. NNLS in der Lage, das (vierte) fibrotische Kompartiment zu erkennen und zwischen 10 % und 30 % Fibrose zu unterscheiden.

Fazit

In dieser Arbeit habe ich die Machbarkeit des *Split-Echo-RARE* als Alternative zur üblichen *ss-EPI* Technik in *DWI* Studien demonstriert.

Diese Arbeit demonstriert die Durchführbarkeit der Kontinuummodellierung mit *NNLS*, einem datengesteuerten Ansatz für renale *DWI* als eine Alternative zur Trennung der verschiedenen renalen Wasserdiffusionsquellen unter verschiedenen (patho)physiologischen Bedingungen, einschließlich eines erhöhten tubulären Volumenanteils und verschiedener Fibrosegrade.

1. Introduction

Part of this thesis is based on the work published on Periquito, et al. 2019 (1) and Periquito, et al. "Continuous diffusion spectrum computation for diffusion-weighted magnetic resonance imaging of the kidney tubule system." Quantitative Imaging in Medicine and Surgery 11.7 (2021): 3098-3119.; therefore, it contains direct passages from both publications.

Kidney diseases are a major health issue, with increasing incidence and an estimated two million deaths per year worldwide due to acute kidney injury (AKI) and chronic kidney disease (CKD) and its incidence continues to grow (2-7). While several biomarkers are currently being investigated for renal diagnosis, to date clinical point-of-care biomarkers are still lacking(8-11). To address this urgent unmet clinical need, MRI may provide non-invasive imaging markers to inform on the different stages of pathophysiology, improve prediction and interception of disease progression and evaluate treatment of kidney diseases (6, 12).

1.1   Diffusion-weighted MRI

Diffusion-weighted MRI (DWI) allows non-invasive quantitative measurements that reflect micro-morphological and physiological changes in renal tissues. The relevance and applicability of renal DWI has been demonstrated in numerous preclinical and clinical studies, which used it either as a diagnostic tool or to assess treatment response. Applications include AKI (13) and characterization of renal masses (14), tumors (15-18), lesions (19, 20) and cysts (21), as well as the assessment of renal fibrosis (22-25), allograft pathophysiology (26, 27) diabetic nephropathy (28), and functional changes in CKD (29, 30).

1.1.1   Diffusion-weighted Echo Planar Imaging (EPI)

The most commonly employed DWI technique is single shot echo planar imaging (ss-EPI) because of its fast imaging speed. It is currently the standard method on preclinical MR systems that is suitable for in vivo studies. It offers excellent temporal resolution, insensitivity to bulk motion and provides reasonable spatial resolution. Notwithstanding these advantages, ss-EPI is prone to magnetic susceptibility artifacts that present themselves as signal loss, image distortion and off-resonance effects. These detrimental effects are even more severe at ultrahigh magnetic field (B_0) strengths, and particularly pronounced in regions with a poor B_0 homogeneity. Hence, diffusion weighted ss-EPI in kidney regions adjacent to bowels or in close proximity to skin/fat/muscle boundaries is particularly challenging and prone to loss of anatomical integrity due to geometric distortions.

Geometric distortions caused by ss-EPI may have serious consequences for the quantitative analysis of renal MRI data. Manual definition of regions-of-interest (ROI) can be extremely challenging when these image distortions are present, as it requires clear distinctions between the renal layers. Semi-automated ROI analysis techniques, such as concentric object analysis (31, 32) or the morphology-based ROI-placement (33, 34) can be severely compromised by geometric distortions.

1.1.2 Diffusion-weighted Rapid Acquisition with Relaxation Enhancement (RARE)

Fast spin-echo imaging techniques are largely insensitive to B_0 inhomogeneity related image distortions and hence present a valuable alternative to EPI particularly at (ultra)high magnetic field strengths (35-42). This makes diffusion sensitized fast spin-echo imaging a promising approach for improving anatomical integrity in renal DWI. The suitability of single-shot Rapid Acquisition with Relaxation Enhancement (ss-RARE) (43) for DWI has been shown for the human kidney at typical clinical field strengths of 1.5 T (44) and 3.0 T (45).

1.2 Separate renal water diffusion sources with continuum modelling: IVIM-NNLS

The renal tubules are a unique anatomical compartment of the kidney, comprising a large fraction of the renal volume. The tubular volume fraction can change due to (i) changes in the glomerular filtration rate, (ii) alterations in tubular outflow towards and beyond the renal pelvis, (iii) modulation of the transmural pressure gradient and (iv) changes in tubular fluid resorption (34). Hence, MR-based assessments of (changes in) the tubular volume fraction are of high relevance in elucidating renal pathophysiological mechanisms.

As mentioned, DWI provides a method for *in vivo* evaluation of water mobility. In the kidneys water mobility may be linked to three different sources: i) tissue water diffusion, ii) blood flow, and iii) tubular flow. To account for the tubular volume fraction in renal diffusion assessment the commonly used mono/bi-exponential intravoxel incoherent motion (IVIM) modelling, was recently extended to a tri-exponential approach (46). Nevertheless, the use of these rigid multi-exponential models in DWI acquisition and analysis protocols is common practice for IVIM MRI of the kidney. The data are forced to conform to *a priori* assumptions of simplified multi-exponential models, however these approaches may not accurately reflect the renal microstructure. The performance of these rigid multi-exponential models is often highly dependent on starting values (47).

Here, I explored the feasibility of separating the different renal water diffusion sources and assessing tubular volume fraction changes with continuum modelling using the non-negative least squares (NNLS)

approach that is data-driven and requires no *a priori* knowledge (number of exponential components, starting values, fixed coefficients).

1.3   Goal of this doctoral work

The goal of this doctoral work is firstly to implement and adapt a diffusion sensitized split-echo RARE technique (48). Validate the proposed technique thoroughly in phantom studies and confirm the hypothesis that DW split-echo RARE outperforms the conventional DW ss-EPI in terms of anatomical integrity and variability of measurements in an *in vivo* DWI study in rats.

The second goal of this work is to show the feasibility and investigate the performance of continuum modelling using NNLS algorithm as a data-driven alternative to rigid models for IVIM techniques to disentangle the different renal water diffusion sources and assess tubular volume fraction changes in different pathophysiological conditions.

2. Materials and Methods

2.1 DW split-echo RARE implementation

A *Stejskal-Tanner* preparation scheme was used to introduce diffusion sensitization (**Figure 1**) to a RARE variant (35): diffusion gradients were placed around the first refocusing pulse and split-echo RARE acquisition was implemented to avoid destructive interferences between even and odd echoes (48). Dummy RF pulses (n=4) were applied prior to data acquisition to balance the signal amplitude between odd and even echo groups (49). A central phase encoding scheme was employed to reduce the time between the diffusion sensitization module and the acquisition of the central k-space region. For comparison, the commonly used diffusion weighted spin-echo (SE) echo-planar imaging (EPI) method was used. A single-shot set-up was chosen, because of the excellent temporal resolution it provides, which is essential for *in vivo* studies of functional dynamics, such as those involving short and reversible physiological stimuli (50).
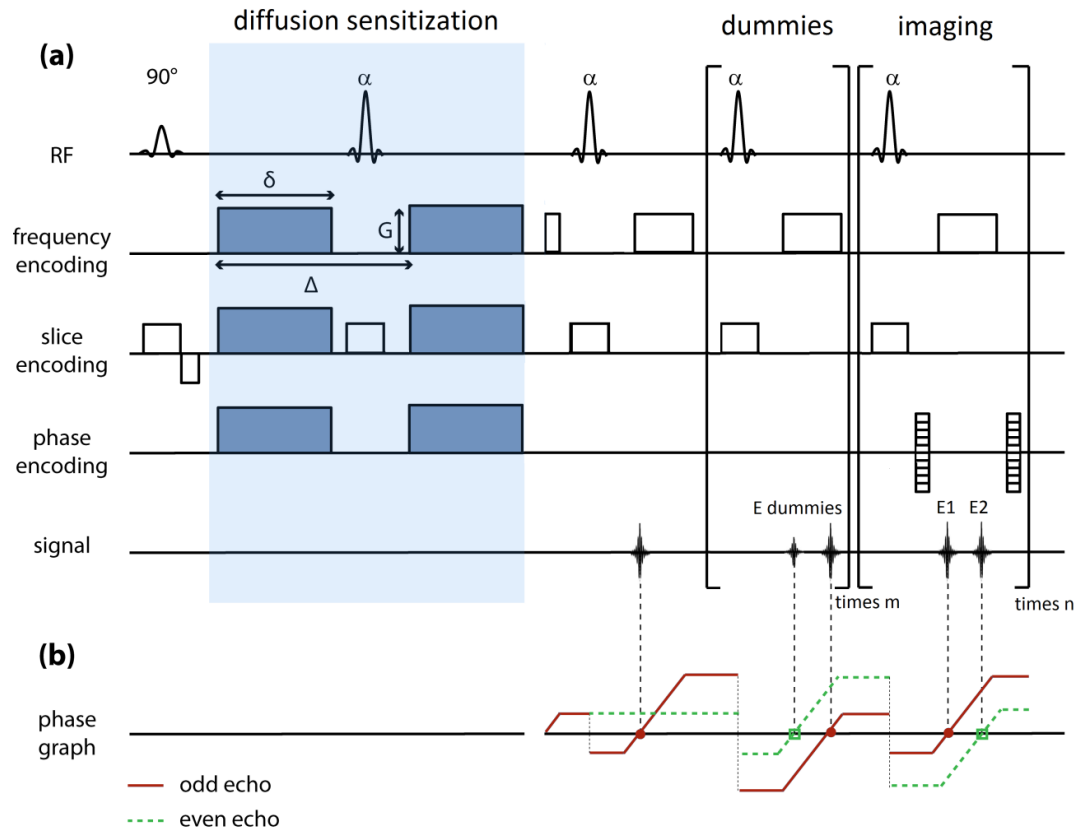
Figure 1: Pulse sequence diagram. a): Basic scheme of the diffusion-sensitized split-echo RARE sequence (48) showing the RF pulse train, the frequency encoding, phase encoding and the slice selection gradients. The dephasing frequency encoding gradient prior to the second refocusing RF pulse α is unbalanced, i.e. the 0th moment of this gradient does not equal half the 0th moment of the readout gradient. Unipolar diffusion sensitization gradients of amplitude G and duration δ, separated by the delay between the onset of the gradient pulses (Δ), surround the first refocusing pulse in phase, frequency and slice encoding. After the third refocusing pulse, the odd (E1) and the even (E2) echo are generated for the first time. The odd (E1) and the even (E2) echoes are acquired within each echo spacing, reconstructed separately, with the resulting images being added afterwards. **b):** The evolution of the magnetization is illustrated in the extended phase graph. Only the two pathways contributing to the signal are shown: the odd echo (red solid line) and the even echo (green dashed line) (1).

2.1.1 Phantoms studies

A phantom containing different substances with known diffusion properties was prepared in order to (i) validate the measured diffusion parameters and furthermore to (ii) examine the propensity of DW ss-EPI and DW split-echo RARE to geometric distortions. The custom-made phantom consisted of three tubes (outer diameter: 7.8 mm) filled with vegetable oil (sunflower oil), de-ionized water, and acetone, respectively. These tubes were placed in a larger cylindrical tube (outer diameter: 30 mm) filled with a 5% solution of agarose to facilitate the imaging, achieve a sensible loading of the RF coil, and reduce macroscopic distortions of the magnetic field B_0.

13

2.1.2 Animal studies

All investigations were approved by the Animal Welfare Department of Berlin's State Office of Health and Social Affairs (LaGeSo) in accordance with the German Animal Protection Law. The procuration of animals, husbandry and experiments conformed to the European Convention for the Protection of Vertebrate Animals used for Experimental and other Scientific Purposes (Council of Europe No 123, Strasbourg 1985). The animals had *ad libitum* access to food (standard diet) and water and were housed under standard conditions with environmental enrichment. Female Wistar rats (aged 12-13 weeks, body weight 288-330 g, n = 7; Harlan-Winkelmann, Borchen, Germany) underwent MRI under isoflurane anesthesia (2.0% in air). Core body temperature was monitored by means of a rectal fiber-optic temperature probe (AccuSens, Opsens, Québec City, Canada). Body temperature was maintained at 37°C with a pad containing circulating warm water connected to a water-bath. Respiration rate was monitored throughout the experiment using a small balloon placed on the chest of the animal (Model 1025, SA Instruments, Stony Brook, NJ, USA) and served for triggering the MRI data acquisition.

2.1.3 MR imaging

All MRI measurements were carried out on a 9.4 Tesla small animal MR system (Bruker Biospec 94/20; Bruker Biospin, Ettlingen, Germany). For phantom experiments, a quadrature transceiver birdcage radiofrequency (RF) volume resonator (inner diameter: 72 mm; Bruker Biospin, Ettlingen, Germany) was employed. *In vivo* studies used a curved 4-channel surface RF coil array (rat heart RF coil, Bruker Biospin, Ettlingen, Germany) for signal reception in conjunction with the above birdcage volume resonator for signal transmission.

I compared the proposed DW split-echo RARE approach against the DW spin-echo EPI method, commonly used in rodents. Images obtained from a DW spin-echo (SE) sequence were used as reference for the phantom assessments. *In vivo*, a gradient-echo sequence (FLASH) served as anatomical reference to measure geometric distortions, since the very long acquisition time of DW SE imaging render this method unfeasible for *in vivo* MRI. These comparisons aimed to validate the measured diffusion parameters and also to examine the propensity of DW ss-EPI and DW split-echo RARE for geometric distortions.

DWI was performed on the phantom and on four Wistar rats *in vivo* using the imaging parameters summarized in **Table 1**. Acquisition parameters were chosen such that both DW ss-EPI and DW split-echo RARE had the same acquisition time. Apart from the fast single-shot protocols, a multi-shot protocol was also used for DW split-echo RARE to demonstrate the image quality achievable at higher spatial resolution. Such protocols for diffusion sensitized split-echo RARE kidney MRI would be of interest for experiments in

which high temporal resolution is not essential, such as in chronic kidney disease (CKD) where pathological changes are rather sluggish.

Table 1: Summary of DWI acquisition parameters for the three set-ups used in the experiments (1).

Experimental set-up	(1) phantom, (2) *in vivo*		(3) *in vivo* (high-resolution)
DWI technique	ss-EPI	split-echo RARE	split-echo RARE
Receiver Bandwidth	300 kHz	131 kHz	131 kHz
Echo time (TE)	25 ms	16 ms	20 ms
Repetition time (TR)	approx. 2.3 s (respiration triggered)		
Field of view	(45x45) mm^2		
Effective Acquisition matrix	96 x 192		128 x 256
Spatial resolution	0.47 x 0.23		0.35 x 0.18
Slice thickness	1.5 mm		1.5 mm
segments / Echo train length (ETL)	1 / 192		4 / 64
Averages	8		8
Acquisition time per b-value	18 s		73 s
Total acquisition time (5x3 b-values)	4 min 30 s		18 min 15 s

Diffusion weighting was achieved using the following b-values: 0, 200, 300, 500 and 700 s/mm^2. In the homogenous phantom one diffusion direction was used. To account for diffusion anisotropy effects in the kidney, each of these acquisitions was performed in three orthogonal diffusion directions, yielding 15 (5 b-values × 3 directions) acquisitions in total. Respiratory motion artifacts were reduced by triggering the data acquisition based on the respiratory signal trace.

2.2   Quantification of water diffusion

2.2.1   Phantom studies

Diffusion coefficient maps were generated for the diffusion phantom by a pixel-wise linear fitting performed after taking the logarithm of the signal intensities obtained at the 5 b-values.

$$S(b) = S_0 . e^{-bD} \qquad \text{[Eq. 1]}$$

where *S* is the signal intensity and S_0 is defined as the signal intensity at b=0 s/mm^2. *D* is the diffusion coefficient also referred to as the "apparent diffusion coefficient" (ADC), recognizing that is depends on

both, the nature of the media studied and on experimental conditions. ROI analysis was performed to determine the mean diffusion coefficient for the three compounds, which were benchmarked against literature values.

2.2.2   Rat kidney *in vivo*

The IVIM approach was used. This consists of a two compartment bi-exponential model, in order to obtain pure diffusion values, without contamination from pseudo-diffusion (i.e. incoherent movement of water by blood perfusion). According to the IVIM approach, the relation between signal intensity and the b-values can be described as:

$$S(b) = S_0(fe^{-bD_p} + (1-f)e^{-bD}) \qquad [Eq. 2]$$

where S is the signal intensity, D_p is pseudo-diffusion coefficient, f is flow fraction and D is slow diffusion (pure diffusion) coefficient. S_0 is defined as the signal intensity at b=0 s/mm^2. For b ≥ 200 s/mm^2 no contribution from D_p is assumed because the signal decay of D_p is much faster than D ($D_p \gg D$). Therefore, I calculated the pure diffusion coefficient from a non-linear least square fit to the signal intensities at b ≥ 200 s/mm^2, which allowed us to use the simplified Equation 1. All three directions were averaged to account for diffusion anisotropy.

ROIs were defined according to the morphological features of the kidney using semi-automated kidney segmentation. ROIs were defined on a coronal kidney image: 5 in the renal cortex (COR), 5 in the outer medulla (OM) and 3 in the inner medulla (IM) as previously described (33). The mean diffusion coefficient of each renal layer (COR, OM, IM) was computed as the average of all ROIs within the layer.

2.2.3   Quantification of geometric distortion

Contours drawn around the cylindrical structures of the phantom in the spin-echo (DW-SE) images were defined as the distortion-free reference. For *in vivo* DWI, a contour drawn around the kidney on a gradient-echo image was used instead. To illustrate the extent of geometric distortions in DW ss-EPI and DW split-echo RARE, I used color-coded difference-maps between the contours drawn in these images and the reference contour.

Geometric distortions were quantified using an in-house developed method of border displacement analysis (program written in MATLAB; The Mathworks, Natick, MA, USA). The metric border displacement between two contours was based on their symmetric difference. For the simple case of two identical contours, there are no pixels outside their intersection; hence the symmetric difference is zero. The

greater the geometric difference between contours A and B, the larger the number of pixels outside their intersection shown in **Figure 2**
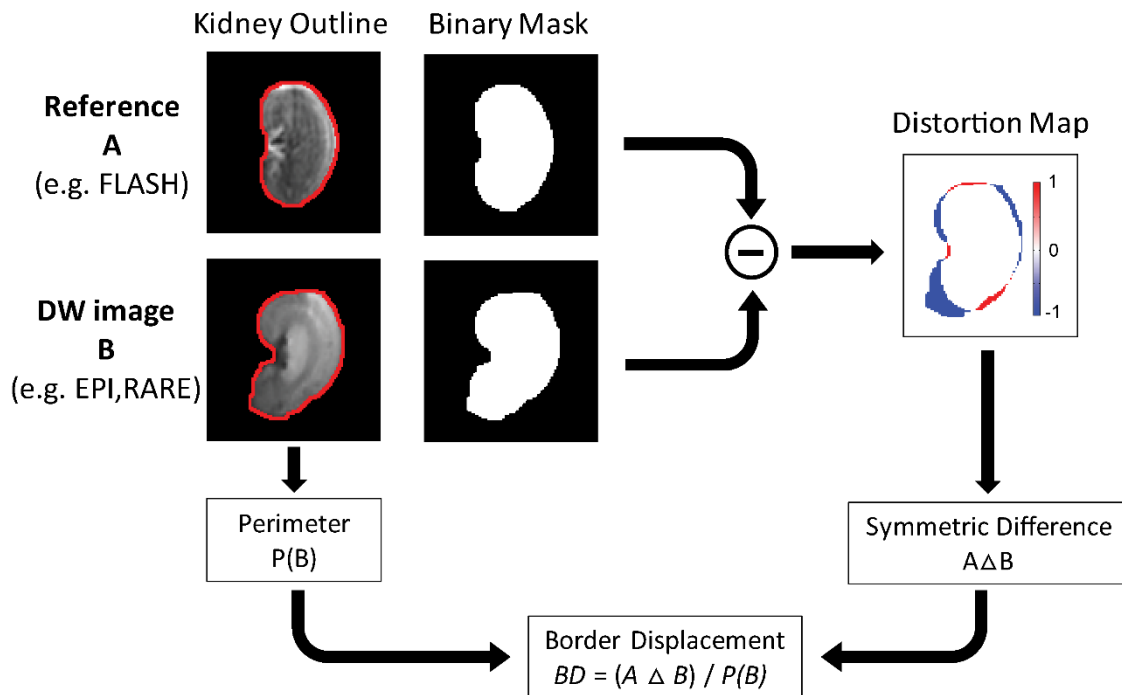
Figure 2: Assessing geometric distortion. The kidney outline (red contour - border of the kidney) was created for the reference image and the DW image. Binary masks were generated for each image using the kidney outline. The distortions maps were calculated by subtracting the binary mask of the DW image to the binary mask of the reference image, a pseudo-colour scale [-1 1] was used from blue (-1) via white to red (1). The red pixels of the distortion map represent missing pixels, and the blue pixels are pixels, which should not exist with respect to the reference mask. Border displacement was calculated by dividing the number of pixels of the distortion map (A △ B) by the perimeter (P(B)) of the kidney outline of the DW Image (1).

2.2.4 Statistics

A normal distribution of the calculated border displacements and diffusion coefficients cannot be assumed, because the susceptibility-induced image distortions influence both in an unpredictable manner. To this end, the results are given as the median together with the minimum to maximum value range (rather than the commonly used mean ± standard deviation). For testing statistical differences, I used the non-parametric Mann-Whitney U test with a significance level of 5%. This test does not make any assumptions about the form of the distributions, requiring only that both groups have the same distributions under the null hypothesis.

2.3 Separate renal water diffusion sources with continuum modelling: IVIM-NNLS

2.3.1 IVIM-NNLS implementation

A multi-exponential analysis based on the NNLS algorithm of Lawson and Hanson (51) was used. The NNLS MATLAB (Mathworks, Natwik, USA) implementation was adapted from the open-source software AnalyzeNNLS from Bjarnason and Mitchell, developed for a multi-exponential analysis of T_2 relaxation of the brain allowing quantification of sub-voxel structures due to water compartmentalization (52).

The output of NNLS is a diffusion coefficient distribution with distinct log-normal-like peaks. Each peak corresponds to a major (pseudo-)diffusion compartment. These peaks can be characterized by i) area under the curve fraction; ii) geometric mean D coefficient.

2.3.2 NNLS numerical simulations

All numerical simulations were implemented in MATLAB. The ground truth signal was created assuming a three compartment IVIM model using the follow equation:

$$SI = f_{tissue} * \exp(-b * D_{tissue}) + f_{tubules} * \exp(-b * D_{tubules}) + f_{blood} * \exp(-b * D_{blood}) \quad \text{[Eq. 3]}$$

where SI is the signal intensity as a function of b (b-value), f_{tissue} the signal fraction of the tissue component, D_{tissue} the diffusion coefficient of restricted water diffusion in renal tissue, $f_{tubules}$ the signal fraction of the tubular component, $D_{tubules}$ the pseudo-diffusion coefficient of the tubular fluid component, f_{blood} the signal fraction of the blood component, and D_{blood} the pseudo-diffusion coefficient of the blood component.

Since the number of compartments might change in pathophysiological conditions of the kidney including the development of fibrosis, a fourth compartment was applied.

$$SI = f_{fibrosis}e^{-b\,D_{fibrosis}} + f_{tissue}e^{-b\,D_{tissue}} + f_{tubules}e^{-b\,D_{tubules}} + f_{blood}e^{-b\,D_{blood}} \quad \text{[Eq. 4]}$$

where $f_{fibrosis}$ is the signal fraction of the fibrotic component, $D_{fibrosis}$ the diffusion coefficient of restricted water diffusion in fibrotic tissue.

The ground truth signal was created assuming a three-compartment or a four-compartment model [eq. 3 and eq. 4] using three sets of parameters:

- The first parameter set was used to represent baseline conditions.

- The second parameter set was used to represent pathophysiological conditions of increased tubular volume fraction ($f_{tubules}$).

- The third parameter set was used to represent pathophysiological conditions of two degrees of renal fibrosis ($f_{fibrosis}$).

Table 2: Summary of multi-exponential parameters used for the generation of the synthetic diffusion decay data.

Parameters	Baseline (46)	Increase of tubular volume fraction	Fibrotic conditions 10%	Fibrotic conditions 30%
Fraction blood (f_{blood})	0.10	0.05	0.10	0.10
Fraction tubules ($f_{tubules}$)	0.30	0.50	0.30	0.30
Fraction tissue (f_{tissue})	0.60	0.45	0.50	0.30
Fraction fibrotic tissue ($f_{fibrosis}$)	0.00	0.00	0.10	0.30
Diffusion blood (D_{blood})	180.0×10^{-3} mm^2/s			
Diffusion tubules ($D_{tubules}$)	5.80×10^{-3} mm^2/s			
Diffusion tissue (D_{tissue})	1.50×10^{-3} mm^2/s			
Diffusion fibrotic tissue ($D_{fibrosis}$)	8×10^{-5} mm^2/s			

Figure 3 describes the workflow from simulation of these parameters to visualization and mean absolute percentage error assessment (MAPE). Admittedly, these parameters obtained from the literature (46) provide a fair approximation but do not fully reflect the complexity and heterogeneity of the renal architecture. All parameters used for (i) baseline, (ii) increased $f_{tubules}$ and (iii) fibrosis conditions are presented in **Table 2**.

For each b-value, Rician noise was added to the signal. The signal [eq. 3 and eq. 4] was then fitted using the NNLS implementation and the common non-linear least square fitting routine (LS). The process was repeated N=500 times for each variation: physiological condition (baseline and increased $f_{tubules}$), b-value range (small range [0-800 mm^2/s] and large range [0-2180 mm^2/s] where SNR [40 80 120 160 200 280 360 440 520 640 760 880 1000] and number of b-values [10 15 20 25 30 35 40 45 50] were varied.

The effect of fixing the diffusion coefficients D_{tissue} and D_{blood} was also studied. Fixing fitting parameters to improve the robustness of the fit is common practice (47), especially when dealing with multi-exponential functions, where at least six parameters are needed.

2.3.3 Mean absolute percentage error (MAPE)

The mean absolute percentage error (MAPE) was used to show the percentage difference between the calculated value and the true value, for the 9 × 13 matrix of b- and SNR values (**Figure 3**). MAPE is defined as:

$$MAPE = \frac{|x^{'} - x|}{x} \cdot 100 \qquad\qquad \text{[Eq. 5]}$$
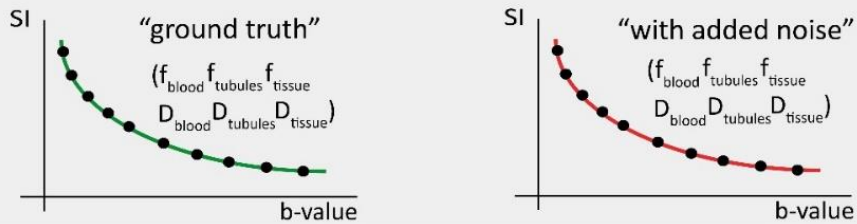
where x' is the calculated parameter and x the true-value.

Definition of Simulation Parameters

(Patho)physiological Condition	Baseline	Increased Tubular Fraction
b-value Range	Small [0 - 800 s/mm²]	Large [0 - 2500 s/mm²]
Fixation of D_{blood}, D_{tissue}	Fixed	Not-fixed
Number of b-values	10 15 20 25 30 35 40 45 50	
SNR	40 80 120 160 200 280 360 440 520 640 760 880 1000	

STEP 1 refers to the rows above.

Diffusion Decay Simulations
(for each parameter combination + 3-compartment model)
n=500 curves

STEP 2

SI — "ground truth"
(f_{blood} $f_{tubules}$ f_{tissue} D_{blood} $D_{tubules}$ D_{tissue})
b-value

SI — "with added noise"
(f_{blood} $f_{tubules}$ f_{tissue} D_{blood} $D_{tubules}$ D_{tissue})
b-value

Fitting: Parameter Calculation

STEP 3

Levenberg-Marquardt (LS)
(f^{LS}_{blood} $f^{LS}_{tubules}$ f^{LS}_{tissue} D^{LS}_{blood} $D^{LS}_{tubules}$ D^{LS}_{tissue})

NNLS-IVIM
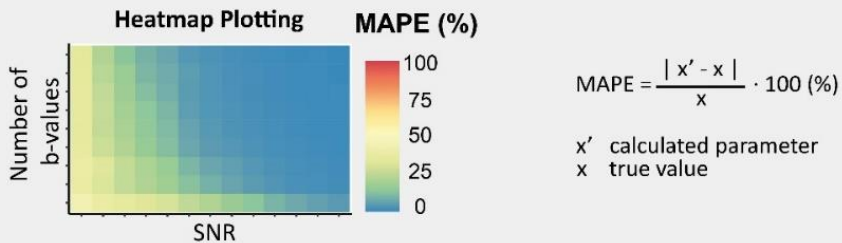(f^{NNLS}_{blood} $f^{NNLS}_{tubules}$ f^{NNLS}_{tissue} D^{NNLS}_{blood} $D^{NNLS}_{tubules}$ D^{NNLS}_{tissue})

Determination of Mean Absolute Percentage Error (MAPE)
(for each of the 6 parameters: f_{blood} $f_{tubules}$ f_{tissue} D_{blood} $D_{tubules}$ D_{tissue} for both fitting methods)
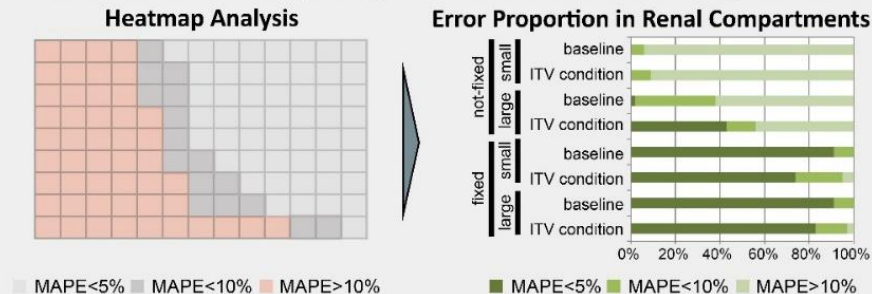
STEP 4

Heatmap Plotting — MAPE (%)

Number of b-values vs SNR

$$MAPE = \frac{|x' - x|}{x} \cdot 100 \ (\%)$$

x' calculated parameter
x true value

Heatmap and Statistical Analysis
(parameter combinations yielding MAPE≤10% and ≤5% for both fitting methods)

STEP 5

Heatmap Analysis

■ MAPE<5% ■ MAPE<10% ■ MAPE>10%

Error Proportion in Renal Compartments

not-fixed: baseline, ITV condition (small); baseline, ITV condition (large)
fixed: baseline, ITV condition (small); baseline, ITV condition (large)

0% 20% 40% 60% 80% 100%

■ MAPE<5% ■ MAPE<10% ■ MAPE>10%

Figure 3: Workflow for assessment and parameter optimization for NNLS analysis of DWI-MRI of the kidney. Numerical simulations were performed and analysed using the NNLS algorithm and the common non-linear least square fit using Levenberg-Marquardt algorithm on different physiological conditions (baseline and challenge - "increased tubular volume fraction"), range of b-values (small range limited to b-value$_{max}$ = 0 – 800 s/mm² and large range covering b-values = 0 – 2500 s/mm²) and parameter fixation (free parameters and fixed D_{blood} and D_{tissue}). MAPE

was calculated (average N=500) using the true-value as a reference. The results were displayed using a MAPE heat map showing the difference between the ground truth and the data obtained from NNLS or LS for each condition. From the MAPE heat map the percentage of combinations (SNR/number of b-values) with a difference between the ground truth and the NNLS data or the LS data of less than 5% or less than 10% were quantified and plotted in an error proportion plot. (*MAPE*: mean absolute percentage error, f_{blood}: volume fraction of blood, $f_{tubules}$: volume fraction of tubules, f_{tissue}: volume fraction of tissue, $f_{fibrosis}$: volume fraction of fibrosis, D_{blood}: diffusion coefficient of blood, $D_{tubules}$: diffusion coefficient of tubules, D_{tissue}: diffusion coefficient of tissue, $D_{fibrosis}$: diffusion coefficient of fibrosis, *b-value*: diffusion weighting, *SNR*: signal-to-noise ratio)

2.3.4 Statistics

The Shapiro-Wilk test was used to assess for Gaussian distribution. MAPE values did not conform to a Gaussian distribution, thus non-parametric statistical tests were used including the paired Wilcoxon signed-rank test, the Kruskal-Wallis test and Dunn's post-hoc procedure. Differences in MAPE obtained for fixing vs. not-fixing the D_{blood} and D_{tissue} diffusion parameters, for the b-value ranges used (0-800 mm^2/s vs. 0-2180 mm^2/s), and for the physiological state (baseline vs. increased tubular volume fraction) were tested independently using the paired Wilcoxon signed-rank test. Differences in MAPE among the 2^3 permutations of the independent variables volume fraction, b-value and fixation state – with each variable having two levels – were assessed with the Kruskal-Wallis non-parametric ANOVA test. The Kruskal-Wallis test was used to compare the area under the curve (AUC) of the fibrotic compartment between the simulated conditions of 30%, 10% and no fibrosis.

3. Results

3.1 DW split-echo RARE measurements

To validate the diffusion weighting of the split-echo RARE, phantom experiments were conducted at room temperature using a cylindrical phantom containing 3 tubes each loaded with water, vegetable oil and acetone. For a quantitative comparison, the diffusion coefficients derived from these measurements are shown in **Figure 4**, together with the literature values. I observed a good agreement between all three DW approaches. However, the DW split-echo RARE method resulted in diffusion coefficients (for water and acetone) that were closer to the literature values than those obtained with the DW ss-EPI and even reference DW-SE method.
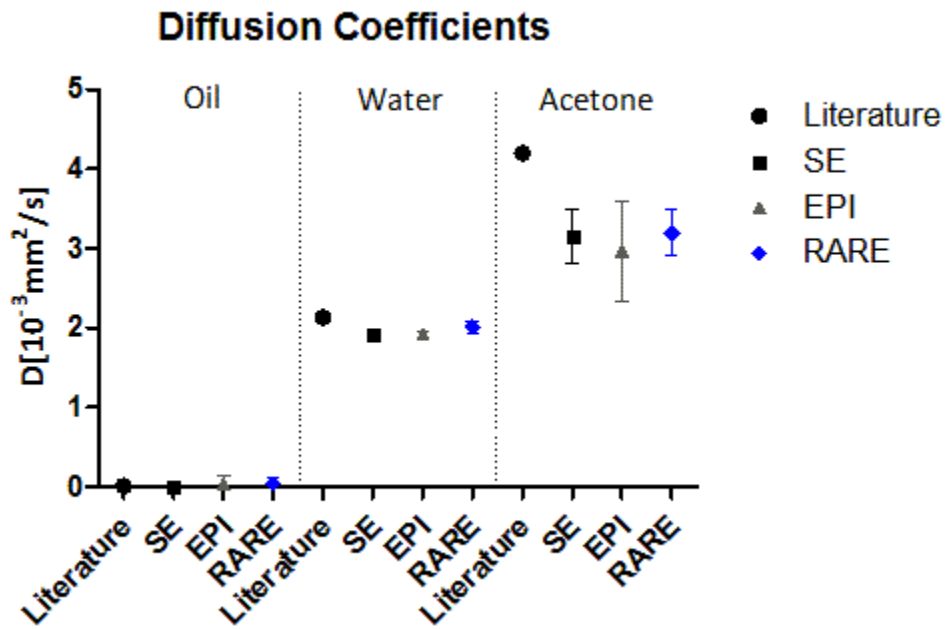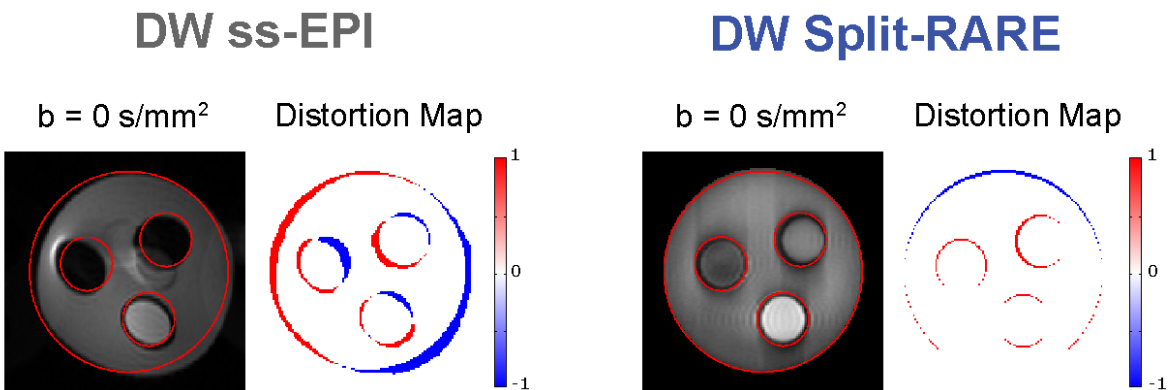

Figure 4: Validation of measured diffusion coefficients for a phantom with known diffusion properties. The diffusion coefficient for vegetable oil, water, and acetone were measured using three diffusion-weighted acquisition techniques: spin-echo (SE; reference, 0.011 ±0.019, 1.91 ±0.07 and 3.15 ±0.34 10-3 mm2/s), ss-EPI (0.041 ±0.10, 1.92 ±0.05 and 2.97 ±0.63 10^{-3} mm^2/s), and split-echo RARE (0.035 ±0.074, 2.01 ±0.07 and 3.19 ±0.29 10^{-3} mm^2/s). Results are compared against literature diffusion coefficients values of vegetable oil (0.010 10^{-3} mm^2/s) water (2.13 10^{-3} mm^2/s) and acetone (4.21 10^{-3} mm^2/s). Diffusion coefficient are in units of 10^{-3} mm^2/s (mean over ROIs ± standard deviation) for ROIs placed in the diffusion coefficient maps for each respective material (1).

### 3.1.1 Geometric fidelity assessment of DWI in phantom experiments

To examine the geometric fidelity of the DWI approaches, the border displacement (BD) analysis was applied to the phantom images of DW split-echo RARE and DW ss-EPI, without diffusion weighting (b = 0 s/mm^2) (**Figure 5**). Red contours derived from the DW-SE reference image were superimposed onto the DW split-echo RARE and DW ss-EPI images (**Figure 5**). Difference (distortion) maps showed that DW split-echo RARE yields close to distortion-free images at 9.4 T with a border displacement of 0.50 [0.31; 0.73] (median of 4 circles [minimum; maximum]. On the other hand, pronounced displacements 1.87 [1.37; 2.41] were observed for DW ss-EPI.


Figure 5: Assessment of geometric fidelity in the test phantom. Images obtained for a structured phantom consisting of three small cylinders within one large one at 9.4T using DW ss-EPI (left panel) and DW split-echo RARE (right panel). The overlaid red contour represents the geometry of the DW SE reference image, which was acquired with the same spatial resolution and matrix size. The color-coded difference maps with respect to the DW SE reference visually demonstrate the amount of distortion, a pseudo-color scale [-1 1] was used from blue (-1) via white to red (1). The artifacts along the phase encoding direction obtained for split-echo RARE are due to the very sharp boundaries and strong signal intensity changes in the phantom and the length of the echo train (192 x 3.2 ms) (1).

3.1.2 Anatomical integrity assessment on *in vivo* renal DWI

To access anatomical distortions *in vivo*, coronal slices of the rat kidney were acquired using ss-EPI and split-echo RARE, as well as FLASH (as an anatomical reference). Similar to the phantom experiments, split-echo RARE provided almost distortion-free images at 9.4 T as demonstrated by the distortion maps (**Figure 6**). Border displacement analysis yielded BD = 0.79 [0.63; 1.17] pixels for split-echo RARE. In contrast, the border displacement for ss-EPI was significantly (p = 0.013) higher: 2.66 [1.31; 3.61] pixels (**Figure 7**).
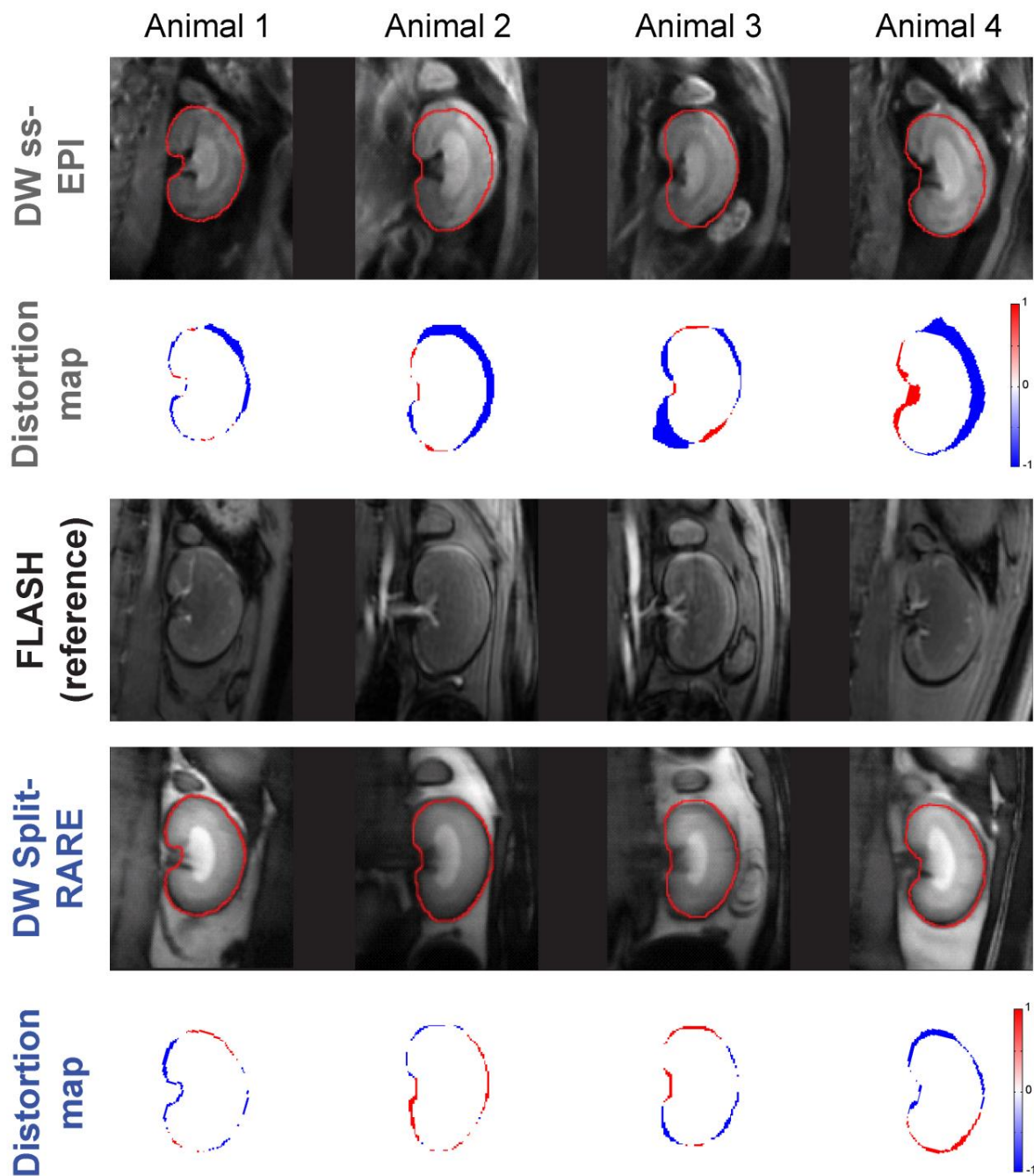
Figure 6: Assessment of geometric distortions in vivo. Coronal images of rat kidneys obtained in four animals in vivo at 9.4T using, DW ss-EPI (b=0mm/s^2) (top row), FLASH (third row) and DW split-echo RARE (b=0 mm/s^2) (fourth row). The respective distortion map (compared to the FLASH reference) is shown below each MR image (third and fifth row), a pseudo-color scale [-1 1] was used from blue (-1) via white to red (1). The red contour represents the border of the kidney in the FLASH reference images, which have high geometric fidelity. Border displacement was markedly smaller with split-echo RARE than with ss-EPI (1).
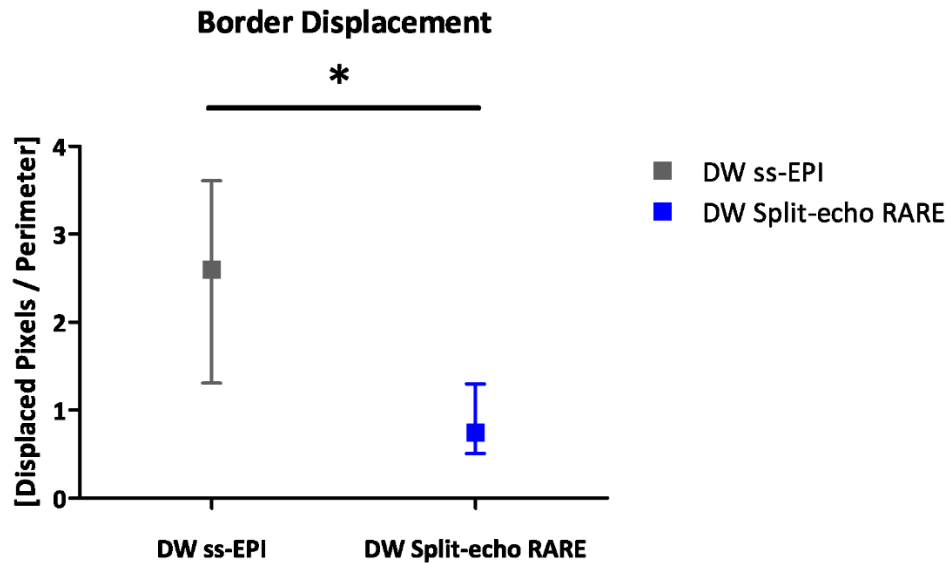
Figure 7: Quantification of border displacement analysis and comparison between DW methods. The median of the measured border displacement (arbitrary units) for ss-EPI was significantly larger (p<0.05) than that for the proposed split-echo RARE approach, the error bars indicate minimum and maximum value (1).

3.1.3 Renal *in vivo* diffusion measurements

The *in vivo* MR images (with varying b values) and corresponding parameter maps obtained with the split-echo RARE method were of markedly better quality and showed fewer artefacts (e.g. susceptibility distortion) than those obtained with the ss-EPI (**Figure 8**). Renal IVIM analysis of the *in vivo* DW Split-echo RARE data from seven animals yielded a diffusion coefficient of D_{COR}= 1.61 [1.34; 2.07] × 10^{-3} mm^2/s for the renal cortex, D_{OM}= 1.78 [1.50; 2.01] × 10^{-3} mm^2/s for the outer medulla and D_{IM}= 1.88 [1.75; 2.27] × 10^{-3} mm^2/s for the inner medulla. The results obtained with DW ss-EPI were similar, but varied much more between subjects, as is evident from the larger difference of [minimum, maximum]: D_{COR}= 1.57 [1.05; 2.13] × 10^{-3} mm^2/s, D_{OM}= 1.50 [1.17; 2.02] × 10^{-3} mm^2/s and D_{IM}= 1.84 [1.72; 2.62] × 10^{-3} mm^2/s.

The high resolution protocol provided excellent image quality (**Figure 9**), which revealed the more subtle structures of the cortico-medullary transition with better contrast.
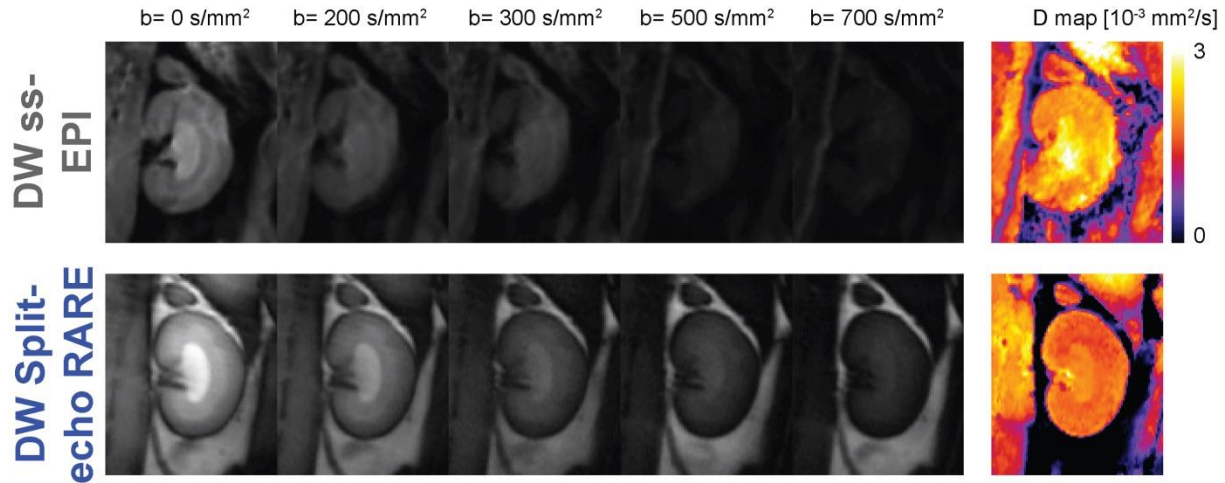
Figure 8: Diffusion weighted images examples and corresponding apparent diffusion coefficient (ADC) maps. Images of a rat kidney acquired at 9.4 T with diffusion weightings raging from (0 to 700 s/mm^2) using the conventional DW ss-EPI (top row) or the DW split-echo RARE (bottom row) method within a total acquisition time of 4.5 minutes. Respective parameter maps of the diffusion coefficient are shown in the right column, a pseudo-color scale [0 3] was used from black (0) via purple, red, orange, yellow to white (3). The quality of the MR images and parameter map was markedly better with split-echo RARE compared with ss-EPI in all four animals (1).
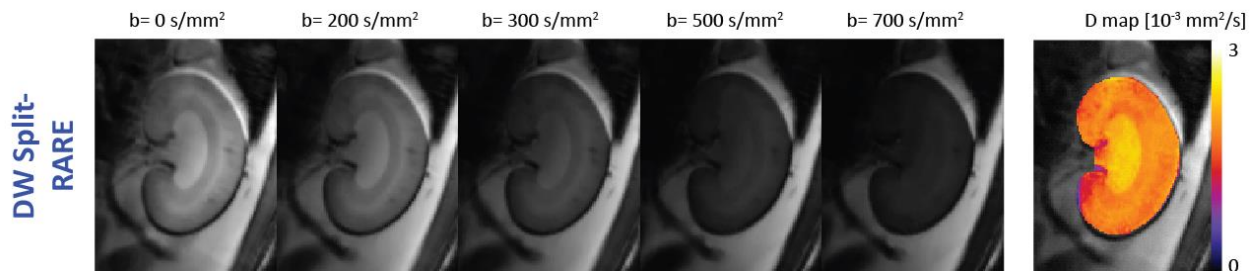
Figure 9: High-spatial resolution diffusion weighted images and apparent diffusion coefficient map 10^{-3}mm^2/s. DW split-echo RARE images of a rat kidney acquired in vivo at 9.4 T using the high spatial resolution protocol and diffusion weightings of b=0 to 700 s/mm^2, together with the respective D map, a pseudo-color scale [0 3] was used from black (0) via purple, red, orange, yellow to white (3). The excellent image/map quality obtained with this 18-minute scan makes the diffusion sensitized split-echo RARE approach attractive for renal steady-state MRI experiments, such as in CKD models (1).

3.2   Continuum modelling: IVIM-NNLS

Analysis of the simulated data with the NNLS continuum modelling resulted in a distribution of diffusion coefficients covering the full range expected for the three components.

3.2.1   MAPE of tubular volume fraction, blood and renal tissue

MAPE was used as a metric to assess which combination of SNR/number of b-values provides less than 5% and 10% error from the true value. **Figure 10.A** shows heat maps of the individual MAPE of the tubular volume fraction for all simulations. As expected, the error decreases with increasing SNR. Increasing the

number of b-values is also beneficial for volume fraction quantification, although this influence is less pronounced than that of SNR. Furthermore, the benefit of additional b-values diminishes with each addition. From 25 b-values onwards, the benefit becomes less apparent. A pronounced increase in the precision is also discernible when using a larger range of b-values (limited versus non-limited). However, in all cases the results are dramatically improved when reducing the number of determined parameters from 6 to 4 by fixing the (pseudo)-diffusion coefficients of blood and tissue. **Figure 10.B** highlights the combinations of SNR/number of b-values that provide a MAPE below 5% and 10% for the tubular volume fraction. Counts of these successful combinations were used to express each of the MAPE heat maps as the percent of combinations with MAPE below 5% and 10%. The number of combinations with an error below 10% with no fixation used was 0% for baseline-small b-value range, 3% for baseline-large b-value range, 10% for increased tubular fraction-small b-value range and 58% for increased tubular fraction-large b-value range. In non-fixed cases, an error below 5% was only found for increased tubular fraction-large b-value range (44% of combinations). The fraction of combinations below 10% error when fixation of D_{blood} and D_{tissue} was used was 91% for baseline and 97% for increased tubular fraction (for both small and large range). An error below 5% was observed in 68% of baseline-small b-value range, 75% of baseline-large b-value range, 81% of increased tubular volume fraction-small b-value range and 86% of increased tubular volume fraction-large b-value range combinations.

Figure 11 shows the percentages of excellent (MAPE<5%), good (MAPE<10%) and unsuitable (MAPE>10%) simulation results for each of the 8 combination of parameters for the renal blood, tubules and tissue compartments. Here I compare LS with NNLS continuum modelling with respect to different MAPE stratifications for each simulated permutation. By fixing the value of blood diffusion coefficient D_{blood} and tissue diffusion coefficient D_{tissue}, more than 60% of all combinations yielded an error below 10% for all parameters and more than 40% provided an error below 5% for all parameters using NNLS continuum modelling. For LS the use of fixation yielded for more than 70% of all combinations an error below 10% for all parameters. More than 50% of the combinations showed an error below 5% for all parameters.
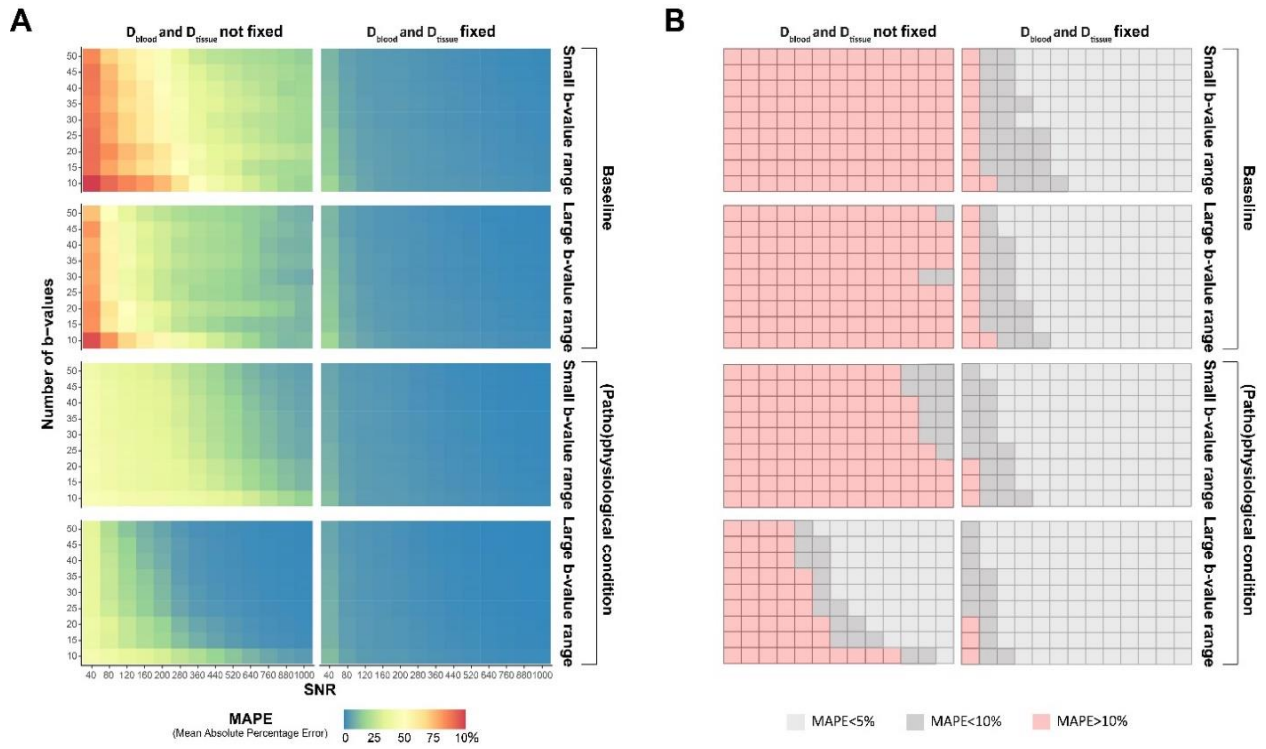
Figure 10: MAPE heat maps for tubular volume fraction for all simulations. A) MAPE heat maps related to tubular fraction for all NNLS simulations. Left column: no parameter fixation; right column: parameter fixation was used (D_{blood} and D_{tissue} were fixed). B) Highlight of the MAPE heat maps related to tubular fraction for all NNLS simulations showing MAPE <5%, <10% and >10%.
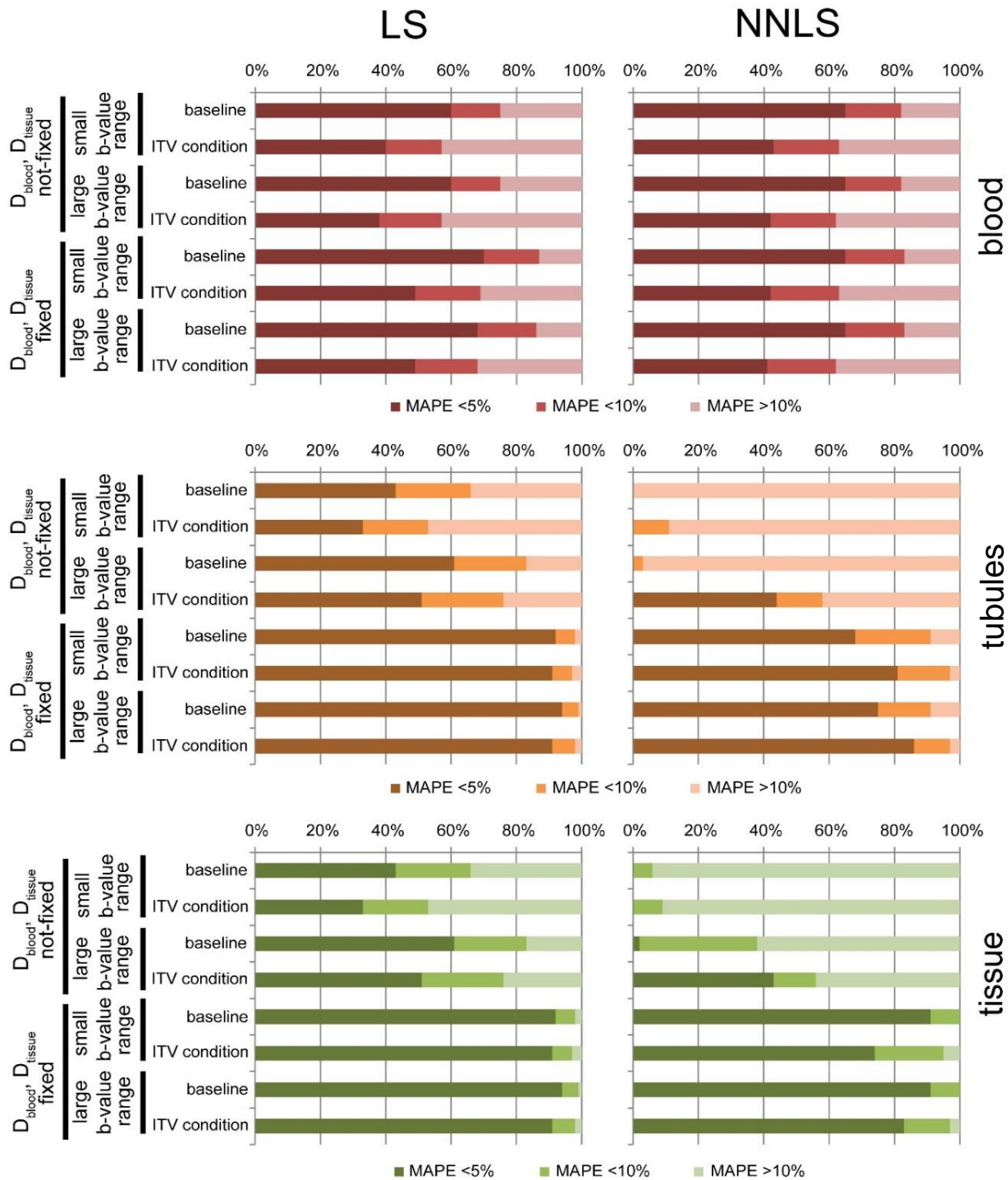
Figure 11: Survey of the results obtained from error analysis. The error proportion plots show the percentage of combinations with the MAPE below 5%/10% using the common non-linear LS fitting routine (left column) and the NNLS method (right column) for all fractions: blood fraction, tubular fraction and tissue fraction.

3.2.2 MAPE of pathophysiological condition of increased tubular volume fraction

For the first pathophysiological condition, I studied the impact of an increase in the tubular volume fraction. This condition does not alter the number of compartments. Increasing tubular volume fraction

significantly reduced the MAPE in this compartment, compared to baseline (p=2.15×10^{-78}, Wilcoxon signed-rank test). When considering differences among all permutations of the three simulation conditions (i.e. baseline vs. increased tubular volume fraction, smallest vs. largest b-value range, fixation of D_{blood} and D_{tissue} vs. no fixation – three conditions with two levels each, 2^3=8), the error values differed significantly (Kruskal-Wallis statistic=621.1, eta^2 effect size=0.662, which was independent of the number of simulations, p=7.07×10^{-130}) (**Figure 12**).
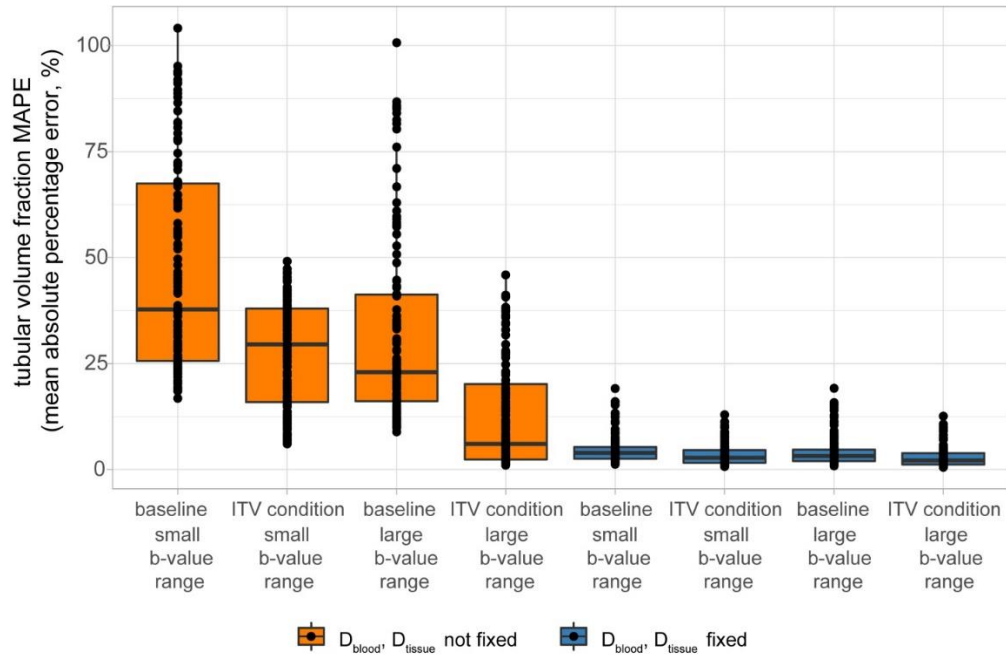
Figure 12: Statistical comparison of the effects of (i) fixation of D_{blood} and D_{tissue} (not-fixed versus fixed), (ii) of the (p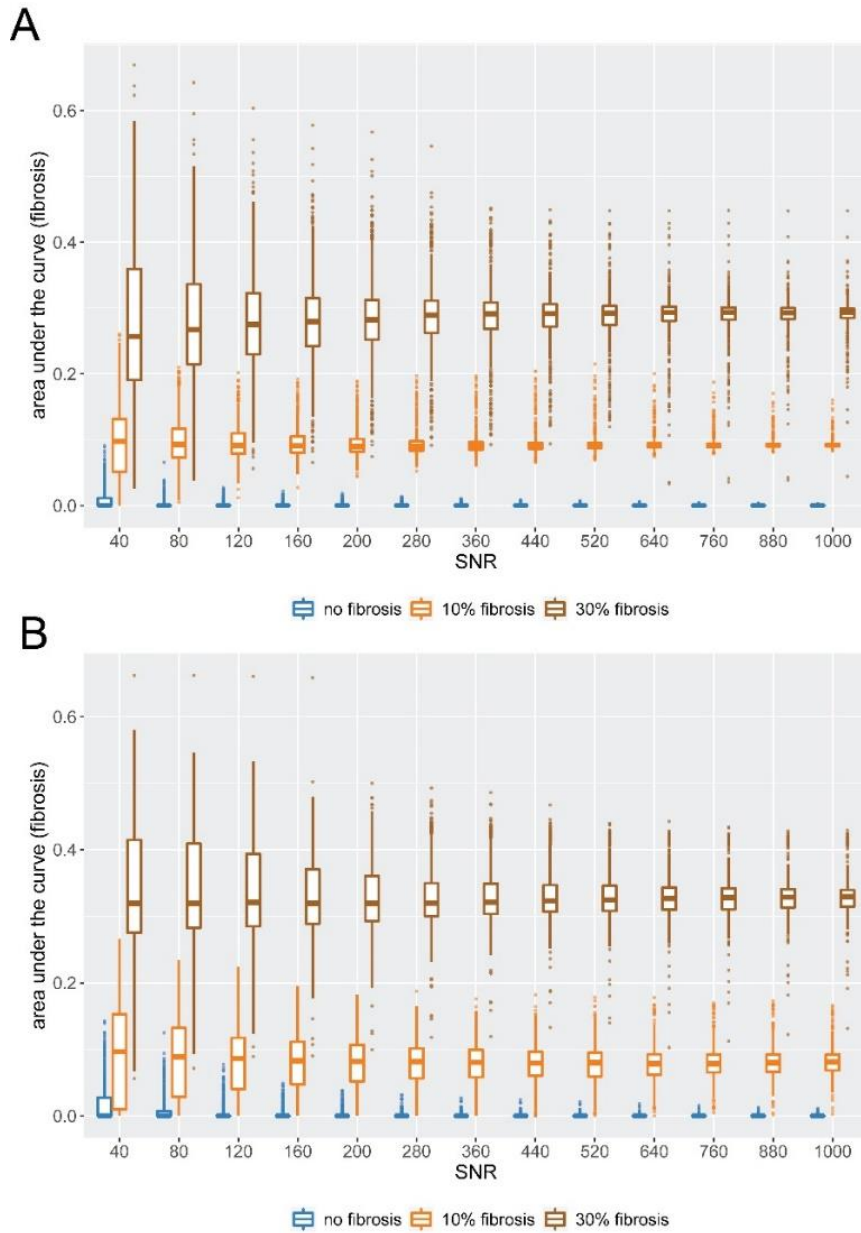atho)physiological condition (baseline versus increased tubular volume) and (iii) of the b-value range (small versus large b-value range). MAPE analysis of the tubular volume fraction from NNLS continuum modelling was compared between all permutations of the simulation conditions: fixation of D_{blood} and D_{tissue} (fixed or not-fixed), (patho)physiological condition (baseline vs. increase in tubular volume) and range of b-values (small b-value range over large b-value range). Each of these three factors had significant effects on the error values when considered independently. Comparing among the permutations showed significant differences in MAPE (p=7.07×10^{-130}, Kruskal-Wallis non-parametric ANOVA, followed by Dunn's procedure with Holm's correction for multiple comparisons).

3.2.3 MAPE of pathophysiological condition of fibrosis

Next I simulated pathophysiological conditions that mimic grade I (mild, 10%) and low grade II (moderate, 30%) interstitial renal fibrosis, thereby adding another component that may be considered as an additional renal compartment ($f_{fibrosis}$). Using data with the maximum b-value range of 0-2180 s/mm^2 (50 b-values), NNLS continuum modelling was able to detect the diffusion component of the fibrotic compartment, to differentiate it from the other three diffusion components, and to distinguish 10% from 30% fibrosis (**Figure 13A**). Furthermore, this was also the case when the medium b-value range of 0-1380 s/mm^2 (15 b-values) was used (**Figure 13B**).

31

Figure 13: NNLS detection of simulated fibrosis component. The simulations included baseline (no fibrosis) and a pathophysiological condition to mimic fibrosis, thus adding a fourth renal compartment. (A) NNLS could readily detect this additional compartment, when using a large b-value range of 0-2180 s/mm^2. (B) This result was also true when a medium b-value range of 0-1380 s/mm^2 was used. For both the large and medium b-value ranges, the area under the curve (signal intensity) of the fibrotic compartment was significantly greater under both the simulated conditions of grade I (mild) and grade II (moderate) fibrosis (affecting 10% and 30% of the renal area, respectively) compared to the non-fibrosis condition. The signal intensities obtained for grade II were significantly higher than for grade I. This distinction improved with increasing SNR (p<2.2×10^{-16}, Kruskal-Wallis non-parametric ANOVA, followed by Dunn's procedure with Holm's correction for multiple comparisons; whiskers denote ± 1.5 x interquartile range).

4. Discussion and Conclusion

Firstly, in this thesis I demonstrate the feasibility of DW Split-echo RARE for renal diffusion weighted imaging (DWI) in small rodents at 9.4 T. I confirmed my hypothesis that DW Split-echo RARE outperforms the conventional DW ss-EPI method in terms of geometrical/anatomical integrity and measurement variability, especially in the *in vivo* experiments.

IVIM analysis of the DW Split-echo RARE data yielded mean diffusion coefficients of 1.65×10^{-3} mm^2/s in the cortex, 1.75×10^{-3} mm^2/s in the outer medulla, and 1.96×10^{-3} mm^2/s in the inner medulla. These values are consistent with those reported in the literature when using DW-EPI (53-55). Results obtained from ss-EPI images were similar to those derived from DW Split-echo RARE but showed a larger variability, especially in the outer and inner medulla. This is probably due to the image artifacts that are observed with ss-EPI. The lower variability and variance in the diffusion coefficients increases the effect size (standardized mean difference between two groups) and hence the statistical power to detect small pathophysiological changes, e.g., in x-ray contrast medium-induced AKI, or during initial stages of diabetic kidney disease.

Anatomical integrity was excellent for the Split-echo RARE technique, and far superior to the ss-EPI approach, which resulted in 3.5-fold larger border displacements for ss-EPI. Severe geometric distortions in the presence of magnet field inhomogeneities are expected with EPI, due to its low effective readout bandwidth in phase encoding direction. Echo-planar imaging variants are commonly used for renal DWI but are prone to magnetic susceptibility artifacts induced by the air-filled bowels, cavities and tissue interfaces surrounding the kidneys. Susceptibility artifacts compromise the anatomical integrity of DWI EPI kidney images and are even prevalent at lower magnetic field strengths (45). Typically, images with severe distortions that cannot be corrected have to be eliminated from analyses. Due to complexity of non-linear geometric distortions, it is conceivable that such distortions might introduce errors when using (semi)automated analysis techniques that assume a certain kidney morphology (e.g. the morphology-based placement of ROIs (33, 34) or the Twelve-Layer Concentric Objects (TLCO) technique (32)). Yet, these detrimental effects may be reduced when large ROIs are used. Taken together, anatomical distortions can lead to increased variability and even unusable data, which in turn hamper intra- and inter-subject comparisons, and may compromise the statistical power of group analyses. Hence, keeping a good anatomical integrity in DWI is critical in order to achieve reliable results in the healthy as well as diseased kidneys – this is the forte of spin-echo-based techniques such as RARE.

Secondly, my results demonstrate the feasibility of the NNLS-IVIM continuum modelling for renal DWI as a less constrained, data-driven alternative for separating the different renal water diffusion sources and monitoring changes in the tubular volume fraction. The numerical simulations demonstrate the impact of SNR, the number of b-values needed for characterization of the diffusion signal decay and the range of diffusion sensitization on NNLS continuum modelling-based renal DWI applications. I show that while the error inherent to the NNLS continuum modelling is not superior to conventional fitting approaches using rigid multi-exponential models *per se,* it strongly depends on the specific parameter combinations applied during renal DWI. The simulations present DWI-MRI parameters that ensure an error of less than 10% and 5%, respectively, for NNLS continuum modelling of the tubular volume fraction when compared to the ground truth given by the tri-exponential model.

A cutoff of 10% error level in acquisition and/or processing methods is a mandatory precondition for guaranteeing robust results in any MR experiment. Error levels below 5% are considered superior, further enhancing robustness and reliability, thereby reducing misinterpretations. Increasing the tubular volume results in greater signal for the tubule-related compartment than at baseline. Consequently, the error of the tubular volume fraction is less for the (patho)physiological condition of increased tubular volume fraction versus baseline. Measuring tubular volume fraction using common acquisition protocols (b=0-800 s/mm^2), resulted in only a small proportion (11%) of the SNR/number of b-values combination having an acceptable error (<10%) under the condition of increased tubular fraction. None of the parameter combinations achieved an acceptable error level under baseline conditions. By extending the acquisition protocols to include a range of b-values up to 2180 s/mm^2 was possible to increase the proportion of parameter combinations with acceptable error levels under the condition of increased tubular fraction to 58%, and obtained a small fraction of 3% for baseline conditions. Nevertheless, a large proportion of combinations still yielded an unacceptable error (97%) for the latter condition. Increasing the number of b-values yielded only a modest improvement in the accuracy to discriminate between the baseline and increased tubular volume fraction conditions based on the tubular volume fraction signal intensity. Therefore, increasing the b-value range alone is not sufficient to ensure reliable measurements of the tubular volume fraction.

In order to address this limitation, I fixed the blood diffusion coefficient D_{blood} and the tissue diffusion coefficient D_{tissue}. With this approach I obtained superior results, compared to the non-fixed value approach. Acceptable errors levels (<10%) were achieved in the majority of the combinations studied (>89%). Data superiority (errors levels <5%) was achieved in more than 60% of the SNR/number of b-values combinations, in both (patho)physiological conditions and when using small and large b-value ranges.

This work also provides potential insights for translational research into MR-based diagnostic tools, as changes in the tubular volume fraction are present in a multitude of kidney disorders. Such changes are prominent in AKI as induced by disturbed systemic hemodynamics, by intravascular administration of x-ray contrast media, and by obstructions of the urinary tract and diabetic nephropathy (4, 8, 56, 57). CKD of most origins is marked by fibrosis in addition to reduced glomerular filtration, which contributes to a decrease in the tubular volume fraction (58). In addition to pathological changes in the tubular volume, our simulations revealed that NNLS continuum modelling for renal DWI may also be useful for detection and treatment monitoring of renal fibrosis, which is an important biomarker of CKD and a powerful predictor of renal outcome (59, 60). These same considerations likely apply to pathologies such as kidney lesions, polycystic kidney disease, or tumors.

To conclude, this work demonstrates that Split-echo RARE has the capability to acquire distortion-free diffusion-weighted images of the rat kidney at ultrahigh magnetic field strengths. Improving anatomical integrity in DWI is a further step towards advancing the capabilities and robustness of parametric imaging of the kidney.

Our results demonstrate the IVIM-NNLS is able to separate the different water diffusion sources and monitor changes in tubular volume fraction with specific acquisition and data processing protocols to warrant results with less than 5%. This work provides the methodological foundation for future investigation into the assessment of renal diffusion properties.

5. References

1.   Periquito JDS, Paul K, Huelnhagen T, Ku MC, Ji Y, Cantow K, Gladytz T, Grosenick D, Flemming B, Seeliger E, Waiczies S, Niendorf T, Pohlmann A. Diffusion-weighted Renal MRI at 9.4 Tesla Using RARE to Improve Anatomical Integrity. Scientific reports. 2019;9(1):19723.
2.   Hoste EAJ, Kellum JA, Selby NM, Zarbock A, Palevsky PM, Bagshaw SM, Goldstein SL, Cerda J, Chawla LS. Global epidemiology and outcomes of acute kidney injury. Nature reviews Nephrology. 2018;14(10):607-25.
3.   Selby NM, Taal MW. Long-term outcomes after AKI-a major unmet clinical need. Kidney international. 2019;95(1):21-3.
4.   Zuk A, Bonventre JV. Recent advances in acute kidney injury and its consequences and impact on chronic kidney disease. Current opinion in nephrology and hypertension. 2019;28(4):397-405.
5.   Glassock RJ, Warnock DG, Delanaye P. The global burden of chronic kidney disease: estimates, variability and pitfalls. Nature reviews Nephrology. 2017;13(2):104-14.
6.   Fortrie G, de Geus HRH, Betjes MGH. The aftermath of acute kidney injury: a narrative review of long-term mortality and renal function. Crit Care. 2019;23(1):24.
7.   Levin A, Tonelli M, Bonventre J, Coresh J, Donner JA, Fogo AB, Fox CS, Gansevoort RT, Heerspink HJL, Jardine M, Kasiske B, Kottgen A, Kretzler M, Levey AS, Luyckx VA, Mehta R, Moe O, Obrador G, Pannu N, Parikh CR, Perkovic V, Pollock C, Stenvinkel P, Tuttle KR, Wheeler DC, Eckardt KU. Global kidney health 2017 and beyond: a roadmap for closing gaps in care, research, and policy. Lancet. 2017;390(10105):1888-917.
8.   Fahling M, Seeliger E, Patzak A, Persson PB. Understanding and preventing contrast-induced acute kidney injury. Nature reviews Nephrology. 2017;13(3):169-80.
9.   van Duijl TT, Ruhaak LR, de Fijter JW, Cobbaert CM. Kidney Injury Biomarkers in an Academic Hospital Setting: Where Are We Now? The Clinical biochemist Reviews. 2019;40(2):79-97.
10.   Luft FC. Biomarkers and predicting acute kidney injury. Acta Physiol (Oxf). 2020:e13479.
11.   Schrezenmeier EV, Barasch J, Budde K, Westhoff T, Schmidt-Ott KM. Biomarkers in acute kidney injury - pathophysiological basis and clinical performance. Acta Physiol (Oxf). 2017;219(3):554-72.
12.   Simms R, Sourbron S. Recent findings on the clinical utility of renal magnetic resonance imaging biomarkers. Nephrology, dialysis, transplantation : official publication of the European Dialysis and Transplant Association - European Renal Association. 2020;35(6):915-9.
13.   Hueper K, Rong S, Gutberlet M, Hartung D, Mengel M, Lu X, Haller H, Wacker F, Meier M, Gueler F. T2 relaxation time and apparent diffusion coefficient for noninvasive assessment of renal pathology after acute kidney injury in mice: comparison with histopathology. Investigative radiology. 2013;48(12):834-42.
14.   Kang SK, Zhang A, Pandharipande PV, Chandarana H, Braithwaite RS, Littenberg B. DWI for Renal Mass Characterization: Systematic Review and Meta-Analysis of Diagnostic Test Performance. AJR Am J Roentgenol. 2015;205(2):317-24.
15.   Aslan M, Aslan A, Arıöz Habibi H, Kalyoncu Uçar A, Özmen E, Bakan S, Kuruğoğlu S, Adaletli İ. Diffusion-weighted MRI for differentiating Wilms tumor from neuroblastoma. Diagn Interv Radiol. 2017;23(5):403-6.
16.   Lei Y, Wang H, Li HF, Rao YW, Liu JH, Tian SF, Ju Y, Li Y, Chen AL, Chen LH, Liu AL, Sun ML. Diagnostic Significance of Diffusion-Weighted MRI in Renal Cancer. Biomed Res Int. 2015;2015:172165.
17.   Hauge A, Wegner CS, Gaustad JV, Simonsen TG, Andersen LMK, Rofstad EK. Diffusion-weighted MRI-derived ADC values reflect collagen I content in PDX models of uterine cervical cancer. Oncotarget. 2017;8(62):105682-91.
18.   Zhu Q, Zhu W, Ye J, Wu J, Chen W, Hao Z. Value of intravoxel incoherent motion for differential diagnosis of renal tumors. Acta Radiol. 2019;60(3):382-7.

19.   Attariwala R, Picker W. Whole body MRI: improved lesion detection and characterization with diffusion weighted techniques. Journal of magnetic resonance imaging : JMRI. 2013;38(2):253-68.

20.   Zhang YL, Yu BL, Ren J, Qu K, Wang K, Qiang YQ, Li CX, Sun XW. EADC Values in Diagnosis of Renal Lesions by 3.0 T Diffusion-Weighted Magnetic Resonance Imaging: Compared with the ADC Values. Appl Magn Reson. 2013;44(3):349-63.

21.   Franke M, Baeßler B, Vechtel J, Dafinger C, Höhne M, Borgal L, Göbel H, Koerber F, Maintz D, Benzing T, Schermer B, Persigehl T. Magnetic resonance T2 mapping and diffusion-weighted imaging for early detection of cystogenesis and response to therapy in a mouse model of polycystic kidney disease. Kidney international. 2017;92(6):1544-54.

22.   Friedli I, Crowe LA, Berchtold L, Moll S, Hadaya K, de Perrot T, Vesin C, Martin PY, de Seigneux S, Vallee JP. New Magnetic Resonance Imaging Index for Renal Fibrosis Assessment: A Comparison between Diffusion-Weighted Imaging and T1 Mapping with Histological Validation. Scientific reports. 2016;6:30088.

23.   Zhao J, Wang ZJ, Liu M, Zhu J, Zhang X, Zhang T, Li S, Li Y. Assessment of renal fibrosis in chronic kidney disease using diffusion-weighted MRI. Clinical radiology. 2014;69(11):1117-22.

24.   Mao W, Zhou J, Zeng M, Ding Y, Qu L, Chen C, Ding X, Wang Y, Fu C, Gu F. Intravoxel incoherent motion diffusion-weighted imaging for the assessment of renal fibrosis of chronic kidney disease: A preliminary study. Magnetic resonance imaging. 2018;47:118-24.

25.   Cai XR, Yu J, Zhou QC, Du B, Feng YZ, Liu XL. Use of intravoxel incoherent motion MRI to assess renal fibrosis in a rat model of unilateral ureteral obstruction. Journal of magnetic resonance imaging : JMRI. 2016;44(3):698-706.

26.   Hueper K, Khalifa AA, Bräsen JH, Vo Chieu VD, Gutberlet M, Wintterle S, Lehner F, Richter N, Peperhove M, Tewes S, Weber K, Haller H, Wacker F, Gwinner W, Gueler F, Hartung D. Diffusion-Weighted imaging and diffusion tensor imaging detect delayed graft function and correlate with allograft fibrosis in patients early after kidney transplantation. Journal of magnetic resonance imaging : JMRI. 2016;44(1):112-21.

27.   Xie Y, Li Y, Wen J, Li X, Zhang Z, Li J, Zhao Y, Wang P, Zhang J, Tian Y, Zhang LJ, Lu GM. Functional Evaluation of Transplanted Kidneys with Reduced Field-of-View Diffusion-Weighted Imaging at 3T. Korean J Radiol. 2018;19(2):201-8.

28.   Feng YZ, Chen XQ, Yu J, Liu XL, Cheng ZY, Ren WW, Feng L, Cai XR. Intravoxel incoherent motion (IVIM) at 3.0 T: evaluation of early renal function changes in type 2 diabetic patients. Abdom Radiol (NY). 2018;43(10):2764-73.

29.   Liang L, Chen WB, Chan KW, Li YG, Zhang B, Liang CH, Liu GS, Zhang SX. Using intravoxel incoherent motion MR imaging to study the renal pathophysiological process of contrast-induced acute kidney injury in rats: Comparison with conventional DWI and arterial spin labelling. Eur Radiol. 2016;26(6):1597-605.

30.   Mao W, Zhou J, Zeng M, Ding Y, Qu L, Chen C, Ding X, Wang Y, Fu C. Chronic kidney disease: Pathological and functional evaluation with intravoxel incoherent motion diffusion-weighted imaging. Journal of magnetic resonance imaging : JMRI. 2018;47(5):1251-9.

31.   Piskunowicz M, Hofmann L, Zuercher E, Bassi I, Milani B, Stuber M, Narkiewicz K, Vogt B, Burnier M, Pruijm M. A new technique with high reproducibility to estimate renal oxygenation using BOLD-MRI in chronic kidney disease. Magnetic resonance imaging. 2015;33(3):253-61.

32.   Milani B, Ansaloni A, Sousa-Guimaraes S, Vakilzadeh N, Piskunowicz M, Vogt B, Stuber M, Burnier M, Pruijm M. Reduction of cortical oxygenation in chronic kidney disease: evidence obtained with a new analysis method of blood oxygenation level-dependent magnetic resonance imaging. Nephrology, dialysis, transplantation : official publication of the European Dialysis and Transplant Association - European Renal Association. 2017;32(12):2097-105.

33.   Pohlmann A, Hentschel J, Fechner M, Hoff U, Bubalo G, Arakelyan K, Cantow K, Seeliger E, Flemming B, Waiczies H, Waiczies S, Schunck WH, Dragun D, Niendorf T. High temporal resolution parametric MRI monitoring of the initial ischemia/reperfusion phase in experimental acute kidney injury. PloS one. 2013;8(2):e57411.

34.   Pohlmann A, Cantow K, Huelnhagen T, Grosenick D, Dos Santos Periquito J, Boehmert L, Gladytz T, Waiczies S, Flemming B, Seeliger E, Niendorf T. Experimental MRI Monitoring of Renal Blood Volume Fraction Variations En Route to Renal Magnetic Resonance Oximetry. Tomography. 2017;3(4):188-200.

35.   Norris DG. Ultrafast low-angle RARE: U-FLARE. Magn Reson Med. 1991;17(2):539-42.

36.   Norris DG, Börnert P, Reese T, Leibfritz D. On the application of ultra-fast RARE experiments. Magn Reson Med. 1992;27(1):142-64.

37.   Norris DG, Bornert P. Coherence and interference in ultrafast RARE experiments. Journal of Magnetic Resonance, Series A. 1993;105(2):123-7.

38.   Niendorf T, Norris DG, Leibfritz D. Detection of apparent restricted diffusion in healthy rat brain at short diffusion times. Magn Reson Med. 1994;32(5):672-7.

39.   Niendorf T. On the application of susceptibility-weighted ultra-fast low-angle RARE experiments in functional MR imaging. Magn Reson Med. 1999;41(6):1189-98.

40.   Niendorf T, Dijkhuizen RM, Norris DG, van Lookeren Campagne M, Nicolay K. Biexponential diffusion attenuation in various states of brain tissue: implications for diffusion-weighted imaging. Magn Reson Med. 1996;36(6):847-57.

41.   Heinrichs U, Utting JF, Frauenrath T, Hezel F, Krombach GA, Hodenius MA, Kozerke S, Niendorf T. Myocardial T2* mapping free of distortion using susceptibility-weighted fast spin-echo imaging: a feasibility study at 1.5 T and 3.0 T. Magn Reson Med. 2009;62(3):822-8.

42.   Utting JF, Kozerke S, Luechinger R, Schnitker R, Vohn R, Bhanniny R, Tilbian M, Niendorf T. Feasibility of k-t BLAST for BOLD fMRI with a spin-echo based acquisition at 3 T and 7 T. Investigative radiology. 2009;44(9):495-502.

43.   Hennig J, Nauerth A, Friedburg H. RARE imaging: a fast imaging method for clinical MR. Magn Reson Med. 1986;3(6):823-33.

44.   Jin N, Deng J, Zhang L, Zhang Z, Lu G, Omary RA, Larson AC. Targeted single-shot methods for diffusion-weighted imaging in the kidneys. Journal of magnetic resonance imaging : JMRI. 2011;33(6):1517-25.

45.   Hilbert F, Wech T, Neubauer H, Veldhoen S, Bley TA, Köstler H. Comparison of Turbo Spin Echo and Echo Planar Imaging for intravoxel incoherent motion and diffusion tensor imaging of the kidney at 3Tesla. Z Med Phys. 2017;27(3):193-201.

46.   van Baalen S, Leemans A, Dik P, Lilien MR, Ten Haken B, Froeling M. Intravoxel incoherent motion modeling in the kidneys: Comparison of mono-, bi-, and triexponential fit. Journal of magnetic resonance imaging : JMRI. 2017;46(1):228-39.

47.   van der Bel R, Gurney-Champion OJ, Froeling M, Stroes ESG, Nederveen AJ, Krediet CTP. A tri-exponential model for intravoxel incoherent motion analysis of the human kidney: In silico and during pharmacological renal perfusion modulation. European journal of radiology. 2017;91:168-74.

48.   Williams CF, Redpath TW, Norris DG. A novel fast split-echo multi-shot diffusion-weighted MRI method using navigator echoes. Magn Reson Med. 1999;41(4):734-42.

49.   Alsop DC. Phase insensitive preparation of single-shot RARE: application to diffusion imaging in humans. Magn Reson Med. 1997;38(4):527-33.

50.   Pohlmann A, Arakelyan K, Hentschel J, Cantow K, Flemming B, Ladwig M, Waiczies S, Seeliger E, Niendorf T. Detailing the relation between renal T2* and renal tissue pO2 using an integrated approach of parametric magnetic resonance imaging and invasive physiological measurements. Investigative radiology. 2014;49(8):547-60.

51.   Lawson CL, Hanson R. Solving least squares problems prentice-hall. Englewood Cliffs. 1974.

52.   Bjarnason TA, Mitchell JR. AnalyzeNNLS: magnetic resonance multiexponential decay image analysis. J Magn Reson. 2010;206(2):200-4.

53.   Notohamiprodjo M, Chandarana H, Mikheev A, Rusinek H, Grinstead J, Feiweier T, Raya JG, Lee VS, Sigmund EE. Combined intravoxel incoherent motion and diffusion tensor imaging of renal diffusion and flow anisotropy. Magn Reson Med. 2015;73(4):1526-32.

54.	Zhang X, Ingo C, Teeuwisse WM, Chen Z, van Osch MJP. Comparison of perfusion signal acquired by arterial spin labeling-prepared intravoxel incoherent motion (IVIM) MRI and conventional IVIM MRI to unravel the origin of the IVIM signal. Magn Reson Med. 2018;79(2):723-9.

55.	Zhang B, Dong Y, Guo B, Chen W, Ouyang F, Lian Z, Liu J, Zhang S. Application of noninvasive functional imaging to monitor the progressive changes in kidney diffusion and perfusion in contrast-induced acute kidney injury rats at 3.0 T. Abdom Radiol (NY). 2018;43(3):655-62.

56.	Premaratne E, Verma S, Ekinci EI, Theverkalam G, Jerums G, MacIsaac RJ. The impact of hyperfiltration on the diabetic kidney. Diabetes & metabolism. 2015;41(1):5-17.

57.	Barasch J, Zager R, Bonventre JV. Acute kidney injury: a problem of definition. Lancet. 2017;389(10071):779-81.

58.	Nezamzadeh M. Diffusion time dependence of magnetic resonance diffusion signal decays: an investigation of water exchange in human brain in vivo. MAGMA. 2012;25(4):285-96.

59.	Ferguson CM, Eirin A, Abumoawad A, Saad A, Jiang K, Hedayat AF, Misra S, Glockner J, Textor SC, Lerman LO. Renal fibrosis detected by diffusion-weighted magnetic resonance imaging remains unchanged despite treatment in subjects with renovascular disease. Scientific reports. 2020;10(1):16300.

60.	Hysi E, Yuen DA. Imaging of renal fibrosis. Current opinion in nephrology and hypertension. 2020;29(6):599-607.

6. Statutory Declaration

"I, João dos Santos Periquito, by personally signing this document in lieu of an oath, hereby affirm that I prepared the submitted dissertation on the topic "Development of Diffusion Weighted Magnetic Resonance Methodology and its Application in Renal Imaging", independently and without the support of third parties, and that I used no other sources and aids than those stated.

All parts which are based on the publications or presentations of other authors, either in letter or in spirit, are specified as such in accordance with the citing guidelines. The sections on methodology (in particular regarding experimental work, data collection and analysis) and results (in particular regarding figures, charts and tables) are exclusively my responsibility.

I further affirm that I have correctly marked data, data analysis and conclusions generated in collaboration with others and have correctly marked my own contribution as well as the contributions of others (see share declaration). I have correctly marked texts or parts of texts that were created or used jointly with others. My contributions to any publications to this dissertation correspond to those stated in the below joint declaration made together with the first supervisor. All publications created within the scope of the dissertation comply with the guidelines of the ICMJE (International Committee of Medical Journal Editors; www.icmje.org) on authorship. In addition, I declare that I am aware of the regulations of Charité – Universitätsmedizin Berlin on ensuring good scientific practice and that I commit to comply with these regulations.

Further, I affirm that I have not already submitted this dissertation in the same or similar form to another faculty.

The significance of this statutory declaration and the consequences of a false statutory declaration under criminal law (Sections 156, 161 of the German Criminal Code) are known to me."

Date   Signature

40

7. Declaration of own contribution

João dos Santos Periquito contributed the following to the below publications:

Publication: Periquito, J.d.S., Paul, K., Huelnhagen, T. et al. Diffusion-weighted Renal MRI at 9.4 Tesla Using RARE to Improve Anatomical Integrity. Sci Rep 9, 19723 (2019). https://doi.org/10.1038/s41598-019-56184-6

Periquito, et al. "Continuous diffusion spectrum computation for diffusion-weighted magnetic resonance imaging of the kidney tubule system." Quantitative Imaging in Medicine and Surgery 11.7 (2021): 3098-3119

Contribution:

• Researched the literature

• Understanding the current state of the art

• Development of the study concept/protocol

• Development and Implementation of diffusion-weighted split-echo RARE technique for renal diffusion at 9.4 Tesla

• Validation of diffusion-weighted split-echo RARE on phantoms and in vivo studies

• Primary data acquisition

• Development, implementation, evaluation and application of the non-negative least squares (NNLS) approach for the analysis of renal DWI-MRI data

• Data analysis and its critical interpretation

• Creation of all diagrams and all figures

• Writing and revising the manuscript

_____

Signature, date and stamp of first supervising university professor / lecturer

_____

Signature of doctoral candidate

8. Extract from the Journal Summary List

Journal Data Filtered By: **Selected JCR Year: 2017** Selected Editions: SCIE,SSCI
Selected Categories: **"MULTIDISCIPLINARY SCIENCES"** Selected Category
Scheme: WoS

Gesamtanzahl: 64 Journale

Rank	Full Journal Title	Total Cites	Journal Impact Factor	Eigenfactor Score
1	NATURE	710,766	41.577	1.355810
2	SCIENCE	645,132	41.058	1.127160
3	Nature Communications	178,348	12.353	0.926560
4	Science Advances	10,194	11.511	0.057080
5	PROCEEDINGS OF THE NATIONAL ACADEMY OF SCIENCES OF THE UNITED STATES OF AMERICA	637,268	9.504	1.108220
6	National Science Review	952	9.408	0.004340
7	GigaScience	1,694	7.267	0.011030
8	Scientific Data	1,567	5.305	0.008550
9	Journal of Advanced Research	1,843	4.327	0.003820
10	Annals of the New York Academy of Sciences	46,160	4.277	0.033270
11	Science Bulletin	1,952	4.136	0.005900
12	Scientific Reports	192,841	4.122	0.718960
13	Journal of the Royal Society Interface	11,357	3.355	0.030960
14	Research Synthesis Methods	1,374	3.218	0.006030
15	PLoS One	582,877	2.766	1.862350
16	PHILOSOPHICAL TRANSACTIONS OF THE ROYAL SOCIETY A-MATHEMATICAL PHYSICAL AND ENGINEERING SCIENCES	17,807	2.746	0.028220
17	Royal Society Open Science	2,145	2.504	0.009260
18	PROCEEDINGS OF THE ROYAL SOCIETY A-MATHEMATICAL PHYSICAL AND ENGINEERING SCIENCES	17,157	2.410	0.018270
19	PeerJ	7,377	2.118	0.031600
20	NPJ Microgravity	94	2.000	0.000350
21	SCIENCE AND ENGINEERING ETHICS	1,496	1.859	0.002520
22	COMPLEXITY	1,369	1.829	0.002380
23	Science of Nature	324	1.789	0.001260

9. Copy of the paper

OPEN

Diffusion-weighted Renal MRI at 9.4 Tesla Using RARE to Improve Anatomical Integrity

João dos Santos Periquito[1], Katharina Paul[1], Till Huelnhagen[1], Min-Chi Ku[1], Yiyi Ji[1], Kathleen Cantow[2], Thomas Gladytz[3], Dirk Grosenick[3], Bert Flemming[2], Erdmann Seeliger[2], Sonia Waiczies[1], Thoralf Niendorf[1,4,5] & Andreas Pohlmann[1]*

Diffusion-weighted magnetic resonance imaging (DWI) is a non-invasive imaging technique sensitive to tissue water movement. By enabling a discrimination between tissue properties without the need of contrast agent administration, DWI is invaluable for probing tissue microstructure in kidney diseases. DWI studies commonly make use of single-shot Echo-Planar Imaging (ss-EPI) techniques that are prone to suffering from geometric distortion. The goal of the present study was to develop a robust DWI technique tailored for preclinical magnetic resonance imaging (MRI) studies that is free of distortion and sensitive to detect microstructural changes. Since fast spin-echo imaging techniques are less susceptible to B_0 inhomogeneity related image distortions, we introduced a diffusion sensitization to a split-echo Rapid Acquisition with Relaxation Enhancement (RARE) technique for high field preclinical DWI at 9.4 T. Validation studies in standard liquids provided diffusion coefficients consistent with reported values from the literature. Split-echo RARE outperformed conventional ss-EPI, with ss-EPI showing a 3.5-times larger border displacement (2.60 vs. 0.75) and a 60% higher intra-subject variability (cortex = 74%, outer medulla = 62% and inner medulla = 44%). The anatomical integrity provided by the split-echo RARE DWI technique is an essential component of parametric imaging on the way towards robust renal tissue characterization, especially during kidney disease.

The prevalence of kidney diseases poses a major public health challenge. Acute kidney injury (AKI) is one of the leading causes of death with an estimated two million deaths per year. Chronic kidney disease (CKD) affects > 10% of the population and its incidence continues to grow[1–4]. There is still a critical need for translational approaches that study renal disease and renoprotective strategies[5–8]. The lack of these approaches underscores the importance of developing biomedical imaging techniques that probe different stages of kidney disorders to better understand the spatio-temporal changes of renal physiology in AKI or CKD and the underlying disease mechanisms[9,10]. It is becoming increasingly evident that quantitative MRI methods can provide vital biomarkers with respect to diagnosis, prognosis and disease prediction, as well as monitoring treatment response. Thereby MRI could improve acute and chronic renal disease management[11] – either alone or as a complement to blood-, urine or tissue-based biomarkers[12].

Diffusion-weighted MRI (DWI) allows quantitative measurements that reflect micro-morphological and physiological changes in renal tissues. Renal DWI requires further investigation before application to routine clinical use. Challenges that need to be overcome in order for research results of renal DWI to be translated to clinical practice, include the harmonization of the acquisition protocols, data post-processing and image analysis[11]. To facilitate the standardization and validation of renal DWI, consensus-based technical recommendations are currently being developed by an international, multidisciplinary group of renal imaging researchers as part of the European Cooperation in Science and Technology (COST) action 'PARENCHIMA' (www.renalmri.org). This is motivated by the relevance of renal DWI having been demonstrated in numerous preclinical and clinical studies with applications such as AKI[13], characterization of renal masses[14], tumors[15–18], lesions[19,20] and cysts[21], as

[1]Berlin Ultrahigh Field Facility (B.U.F.F.), Max Delbrück Center for Molecular Medicine in the Helmholtz Association, Berlin, Germany. [2]Institute of Physiology, Charité Universitätsmedizin Berlin, Campus Mitte, and Center for Cardiovascular Research, Berlin, Germany. [3]Physikalisch-Technische-Bundesanstalt (PTB), Berlin, Germany. [4]Experimental and Clinical Research Center, a joint cooperation between the Charité Medical Faculty and the Max Delbrück Center for Molecular Medicine in the Helmholtz Association, Berlin, Germany. [5]German Centre for Cardiovascular Research (DZHK), partner site Berlin, Germany. *email: andreas.pohlmann@mdc-berlin.de

43

well as the assessment of renal fibrosis[22–25], allograft pathophysiology[26,27], diabetic nephropathy[28], and functional changes in AKI and CKD[29,30].

The most commonly employed DWI technique is single-shot echo planar imaging (ss-EPI) because of its fast imaging speed. It is currently the standard method on preclinical MR systems that is suitable for *in vivo* studies. It offers excellent temporal resolution, insensitivity to bulk motion and provides reasonable spatial resolution. Notwithstanding these advantages, ss-EPI is prone to magnetic susceptibility artifacts that present themselves as T_2^* induced signal loss or even signal voids in areas with very high B_0 gradients, low-phase encoding bandwidth related image distortion and off-resonance effects caused by ΔB_0 induced frequency dispersions[31]. Hence, diffusion weighted ss-EPI in kidney regions adjacent to bowels or in close proximity to skin/fat/muscle boundaries is particularly challenging and prone to loss of anatomical integrity due to geometric distortions.

Geometric distortions caused by ss-EPI may have serious consequences for the quantitative analysis of renal MRI data. Manual definition of regions-of-interest (ROI) can be extremely challenging when these image distortions are present, as it requires clear distinctions between the renal layers. Semi-automated ROI analysis techniques, such as concentric object analysis[32,33] or the morphology-based ROI-placement[34,35] can be severely compromised by geometric distortions.

Fast spin-echo imaging techniques are largely insensitive to B_0 inhomogeneity related image distortions and hence present a valuable alternative to EPI particularly at (ultra)high magnetic field strengths[36–43]. This makes diffusion-sensitized fast spin-echo imaging a promising approach for improving anatomical integrity in renal DWI. The suitability of single-shot Rapid Acquisition with Relaxation Enhancement (ss-RARE[44]) for DWI has been shown for the human kidney at typical clinical field strengths of 1.5 T[45] and 3.0 T[46].

Motivated by the translational prospects of renal DWI along with the signal sensitivity gain at high magnetic fields, this work demonstrates the performance and reliability of a variant of diffusion-sensitized ultrafast RARE[36–44] for DWI of the rodent kidney at 9.4 T. To meet this goal we implemented and adapted a diffusion-sensitized split-echo RARE (DW Split-echo RARE) technique[47]. First, we validated the proposed technique thoroughly in phantom studies. Then, we confirmed the hypothesis that DW Split-echo RARE outperforms the conventional DW ss-EPI in terms of anatomical integrity and variability of measurements in an *in vivo* DWI study in rats.

Materials and Methods

Implementation and optimization of the Split-echo RARE DWI technique.
A Stejskal-Tanner preparation scheme was used to introduce diffusion sensitization to a RARE variant[48]: Diffusion gradients were placed around the first refocusing pulse and Split-echo RARE acquisition was implemented to avoid destructive interferences between even and odd echoes[47]. Further details on the pulse sequence (a pulse sequence diagram) are provided as Supplementary Information. Dummy RF pulses (n = 4) were applied prior to data acquisition to balance the signal amplitude between odd and even echo groups[49]. A central phase encoding scheme was employed to reduce the time between the diffusion sensitization module and the acquisition of the central k-space region. For comparison, the commonly used diffusion weighted spin-echo (SE) echo-planar imaging (EPI) method was used. A single-shot set-up was chosen, because of the excellent temporal resolution it provides, which is essential for *in vivo* studies of functional dynamics, such as those involving short and reversible physiological stimuli[50] or the characterization of early pathophysiological events in AKI[34].

Phantoms.
A phantom containing different substances with known diffusion properties was prepared in order to (i) validate the measured diffusion parameters and to (ii) examine the propensity of DW ss-EPI and DW Split-echo RARE to geometric distortions. The custom-made phantom consisted of three tubes (outer diameter: 7.8 mm) filled with vegetable oil (sunflower oil), de-ionized water, and acetone, respectively. These tubes were placed in a larger cylindrical tube (outer diameter: 30 mm) filled with a 5% solution of agarose to facilitate the imaging, achieve a sensible loading of the RF coil, and reduce macroscopic distortions of the magnetic field B_0.

Animals.
All investigations were approved by the Animal Welfare Department of Berlin's State Office of Health and Social Affairs (*LaGeSo*) in accordance with the German Animal Protection Law. The procuration of animals, husbandry and experiments conformed to the European Convention for the Protection of Vertebrate Animals used for Experimental and other Scientific Purposes (Council of Europe No 123, Strasbourg 1985). The animals had ad libitum access to food (standard diet) and water and were housed under standard conditions with environmental enrichment. Female Wistar rats (aged 12–13 weeks, body weight 288–330 g, n = 7; Harlan-Winkelmann, Borchen, Germany) underwent MRI under isoflurane anesthesia (2.0% in air). All animals scanned were included in the data analysis. Core body temperature was monitored by means of a rectal fiber-optic temperature probe (AccuSens, Opsens, Québec City, Canada). Body temperature was maintained at 37 °C with a pad containing circulating warm water connected to a water-bath. Respiration rate was monitored throughout the experiment using a small balloon placed on the chest of the animal (Model 1025, SA Instruments, Stony Brook, NJ, USA) and served for triggering the MRI data acquisition.

Magnetic resonance imaging.
All MRI measurements were carried out on a 9.4 Tesla small animal MR system (Bruker Biospec 94/20; Bruker Biospin, Ettlingen, Germany). For phantom experiments, a quadrature transceiver birdcage radiofrequency (RF) volume resonator (inner diameter: 72 mm; Bruker Biospin, Ettlingen, Germany) was employed. *In vivo* studies used a curved 4-channel surface RF coil array (rat heart RF coil, Bruker Biospin, Ettlingen, Germany) for signal reception in conjunction with the above birdcage volume resonator for signal transmission.

We compared the proposed DW Split-echo RARE approach against the DW spin-echo EPI method commonly used in rodents. Images obtained from a DW spin-echo (SE) sequence were used as reference for the phantom assessments. *In vivo*, a gradient-echo sequence (FLASH) served as anatomical reference to assess geometric

44

Experimental set-up	(1) phantom, (2) *in vivo*		(3) *in vivo* (high-resolution)
DWI technique	ss-EPI	Split-echo RARE	Split-echo RARE
Receiver Bandwidth	300 kHz	131 kHz	131 kHz
Echo time (TE)	25 ms	16 ms	20 ms
Repetition time (TR)	approx. 2.3 s (respiration triggered)		
Field of view	(45 × 45) mm²		
Effective Acquisition matrix	96 × 192		128 × 256
Spatial resolution	0.47 × 0.23		0.35 × 0.18
Slice thickness	1.5 mm		1.5 mm
segments/Echo train length (ETL)	1/192		4/64
Averages	8		8
Acquisition time per b-value	18 s		73 s
Total acquisition time (5 × 3 b-values)	4 min 30 s		18 min 15 s

Table 1. Summary of DWI acquisition parameters for the three set-ups used in the experiments.

distortions, since the very long acquisition time of DW SE imaging render this method unfeasible for *in vivo* MRI. These comparisons aimed to validate the measured diffusion parameters and also to examine the propensity of DW ss-EPI and DW Split-echo RARE for geometric distortions.

DWI was performed on the phantom and on seven Wistar rats *in vivo* using the imaging parameters summarized in Table 1. Acquisition parameters were chosen such that both DW ss-EPI and DW Split-echo RARE had the same acquisition time. Apart from the fast single-shot protocols, a multi-shot protocol was also used for DW Split-echo RARE to demonstrate the image quality achievable at higher spatial resolution. Such protocols for diffusion sensitized Split-echo RARE kidney MRI would be of interest for experiments in which high temporal resolution is not essential, such as in chronic kidney disease (CKD) where pathological changes are rather sluggish.

Diffusion weighting was achieved using b-values of 0, 200, 300, 500 and 700 s/mm². In the homogenous phantom one diffusion direction was used. To account for diffusion anisotropy effects in the kidney, each of these acquisitions was performed in three orthogonal diffusion sensitization directions, yielding 15 (5 b-values × 3 directions) acquisitions in total. Respiratory motion artifacts were reduced by triggering the data acquisition based on the respiratory signal trace.

Quantification of water diffusion. *Phantom.* Diffusion coefficient maps were generated for the diffusion phantom by a pixel-wise linear fitting performed after taking the logarithm of the signal intensities obtained at the 5 b-values.

$$S(b) = S_0 . \ e^{-bD} \tag{1}$$

where S is the signal intensity and S_0 is defined as the signal intensity at $b = 0$ s/mm². D is the diffusion coefficient also referred to as the 'apparent diffusion coefficient' (ADC), recognizing that is depends on both, the nature of the media studied and on experimental conditions. ROI analysis was performed to determine the mean diffusion coefficient for the three compounds, which were benchmarked against literature values.

Rat kidney in vivo. The intra-voxel incoherent motion (IVIM) approach was used. This consists of a two compartment bi-exponential model, in order to obtain pure diffusion values, without contamination from pseudo-diffusion (i.e. incoherent movement of water by blood perfusion). According to the IVIM approach, the relation between signal intensity and the b-values can be described as:

$$S(b) = S_0(fe^{-bD_p} + (1 - f)e^{-bD}) \tag{2}$$

where S is the signal intensity, D_p is pseudo-diffusion coefficient, f is flow fraction and D is slow diffusion (pure diffusion) coefficient. S_0 is defined as the signal intensity at $b = 0$ s/mm². For $b \geq 200$ s/mm² no contribution from D_p is assumed because the signal decay of D_p is much faster than D ($D_p \gg D$). Therefore, we calculated the pure diffusion coefficient from a non-linear least square fit to the signal intensities at $b \geq 200$ s/mm², which allowed us to use the simplified Eq. 1. All three directions were averaged to account for diffusion anisotropy.

ROIs were defined according to the morphological features of the kidney using semi-automated kidney segmentation[35]. ROIs were defined on a coronal kidney image: 5 in the renal cortex (COR), 5 in the outer medulla (OM) and 3 in the inner medulla (IM) as previously described[35]. The mean diffusion coefficient of each renal layer (COR, OM, IM) was computed as the average of all ROIs within the layer.

Quantification of geometric distortion. Contours drawn around the cylindrical structures of the phantom in the spin-echo (DW SE) images were defined as the distortion-free reference. For *in vivo* DWI, a contour drawn around the kidney on a gradient-echo image was used instead. These contours were determined by two experienced MR experts, under the supervision of a senior board certified radiologist. To illustrate the extent of geometric distortions in DW ss-EPI and DW Split-echo RARE, we used color-coded difference-maps between the contours drawn in these images and the reference contour.

45
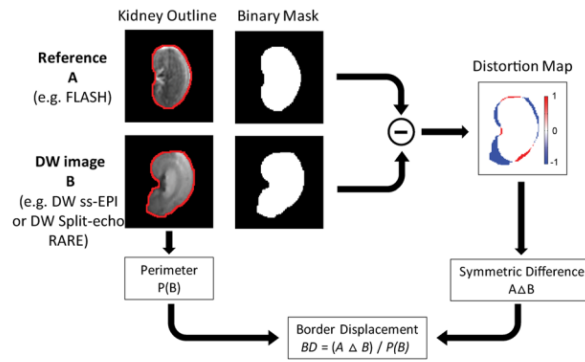
Figure 1. Assessing geometric distortion. The kidney outline (red contour - border of the kidney) was created for the reference image and the DW image. Binary masks were generated for each image using the kidney outline. The distortions maps were calculated by subtracting the binary mask of the DW image from the binary mask of the reference image, a pseudo-colour scale [−1 1] was used from blue (−1) to red (+1). The red pixels of the distortion map represent false negatives, and the blue pixels represent false positives, for the DW image with respect to the reference mask. Border displacement was calculated by dividing the number of pixels of the distortion map ($A \Delta B$) by the perimeter ($P(B)$) of the kidney outline of the DW Image.

Figure 2. The border displacement metric is fairly insensitive to the object's size and shape. Horizontal, vertical and diagonal displacements (5 or 10 pixels) were artificially applied to three objects of different shape and size: a small circle (top row), a large circle (middle row) and a kidney shape (bottom row). The border displacement (BD) is given below each object. While the simulated small and large displacements lead to similarly different BD (compare left and right), the BD varied only little between the three different objects (compare along vertical axes).

Geometric distortions were quantified using an in-house developed method of border displacement analysis (Fig. 1; program written in MATLAB; The Mathworks, Natick, MA, USA). The metric *border displacement* between two contours was based on their *symmetric difference*, an elementary mathematical operation of set theory. The *symmetric difference* of two sets, *A* and *B*, includes all objects (here the pixels) in A and B (here the two contours) that are outside their intersection: $A \Delta B := \{x \mid (x \in A \wedge x \notin B) \vee (x \in B \wedge x \notin A)\}$. For the simple case of two identical contours, there are no pixels outside their intersection, hence the symmetric difference is zero. The greater the geometric difference between contours *A* and *B*, the larger the number of pixels outside their intersection, i.e. the larger their symmetric difference. To permit meaningful comparisons of *border displacements* calculated from images with different spatial resolution, and even from objects of different shape and size (e.g. tubes, organs or other structures) we normalized the symmetric difference to the contour length, i.e. the object's perimeter *P*, and defined the *border displacement* (BD) as

$$BD = (A \Delta B)/P(B) \tag{3}$$

with *A* being the contour to be assessed, *B* the reference contour, and *P(B)* the perimeter of the reference contour; or verbose: *Border displacement = Symmetric difference(Contour, Reference-contour)/Perimeter(Reference-contour)*. This metric yields comparable results for the same extent of distortion applied to objects of different sizes and shapes, as demonstrated with the simulations shown in Fig. 2.

Statistical tests. A normal distribution of the calculated border displacements and diffusion coefficients cannot be assumed, because the susceptibility-induced image distortions influence both in an unpredictable manner. To this end, the results are given as the median together with the minimum to maximum value range (rather than the commonly used mean ± standard deviation). For testing statistical differences we used the non-parametric Mann-Whitney U test with a significance level of 5%. This test does not make any assumptions about the form of the distributions, requiring only that both groups have the same distributions under the null hypothesis.

46
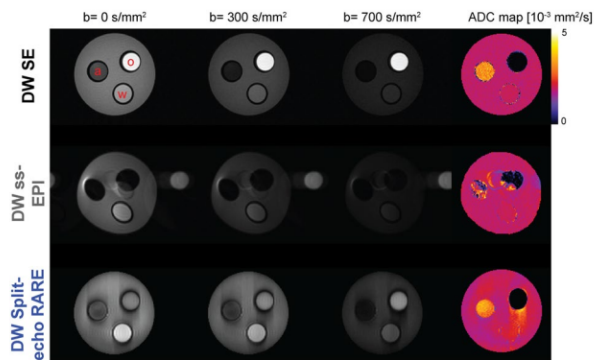
Figure 3. Diffusion weighted images and derived diffusion maps of the test phantom. Selection of images with b-values in the range b = 0 s/mm² to b = 700 s/mm² acquired with DW SE (top row), DW ss-EPI (middle row) and DW Split-echo RARE (bottom row). The right column shows corresponding diffusion maps for each of the three approaches calculated from the series of diffusion-weighted images, a pseudo-color scale [0 5] was used from black (0) via purple, red, orange, yellow to white (5). The cylindrical phantom contains acetone ("a"), water ("w") and vegetable oil ("o") in three tubes within a larger tube with agarose. As expected, one can observe the inherent geometric distortions with DW ss-EPI (due to the low effective bandwidth in phase encoding direction) and blurring with DW Split-echo RARE (due to the effect of the T_2-decay on the point-spread-function and inter-echo spacing). The artifacts along the phase encoding direction obtained for DW split-echo RARE are due to the very sharp boundaries and strong signal intensity changes in the phantom and the length of the echo train (192 × 3.2 ms).
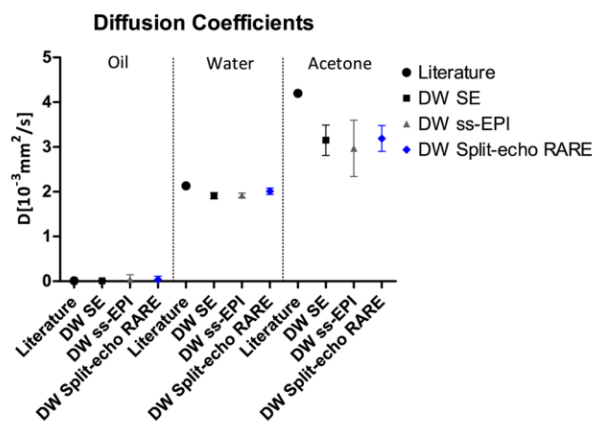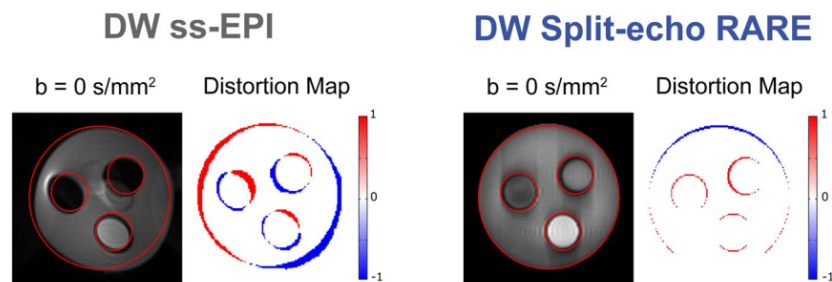

Figure 4. Validation of measured diffusion coefficients for a phantom with known diffusion properties. The diffusion coefficient for vegetable oil, water, and acetone were measured using three diffusion-weighted acquisition techniques: spin-echo (SE; reference, 0.011 ± 0.019, 1.91 ± 0.07 and 3.15 ± 0.34 10^{-3} mm²/s), DW ss-EPI (0.041 ± 0.10, 1.92 ± 0.05 and 2.97 ± 0.63 10^{-3} mm²/s), and DW Split-echo RARE (0.035 ± 0.074, 2.01 ± 0.07 and 3.19 ± 0.29 10^{-3} mm²/s). Results are compared against literature diffusion coefficients values of vegetable oil (0.010 10^{-3} mm²/s)[67] water (2.13 10^{-3} mm²/s)[68] and acetone (4.21 10^{-3} mm²/s)[69,70]. Diffusion coefficient are in units of 10^{-3} mm²/s (mean over ROIs ± standard deviation) for ROIs placed in the diffusion coefficient maps for each respective material.

Results

We acquired experimental data to validate that the diffusion parameters measured with the DW Split-echo RARE are correct, to assess the geometric fidelity of the images, and to detail the diffusion parameters obtained in healthy rat kidneys.

Diffusion measurements. To validate the diffusion weighting of the Split-echo RARE, phantom experiments were conducted at room temperature using a cylindrical phantom containing 3 tubes each loaded with water, vegetable oil and acetone. Figure 3 illustrates diffusion-weighted images for selected b-values and the corresponding parameter maps of the diffusion coefficient (D) calculated for DW SE reference acquisitions as well as DW Split-echo RARE and DW ss-EPI measurements. For a quantitative comparison, the diffusion coefficients derived from these measurements are shown in Fig. 4, together with the literature values. We observed a good agreement between all three DW approaches. However, the DW Split-echo RARE method resulted in diffusion

47

Figure 5. Assessment of geometric fidelity in the test phantom. Images obtained for a structured phantom consisting of three small cylinders within one large one at 9.4 T using DW ss-EPI (left panel) and DW Split-echo RARE (right panel). The overlaid red contour represents the geometry of the DW SE reference image, which was acquired with the same spatial resolution and matrix size. The color-coded difference maps with respect to the DW SE reference visually demonstrate the amount of distortion, a pseudo-color scale [−1 1] was used from blue (−1) via white to red (1). The artifacts along the phase encoding direction obtained for DW Split-echo RARE are due to the very sharp boundaries and strong signal intensity changes in the phantom and the length of the echo train (192×3.2 ms).

coefficients (for water and acetone) that were closer to the literature values than those obtained with the DW ss-EPI and even reference DW SE method.

Geometric fidelity assessment of DWI in phantom experiments. To examine the geometric fidelity of the DWI approaches, the border displacement (BD) analysis was applied to the phantom images of DW Split-echo RARE and DW ss-EPI, without diffusion weighting ($b = 0$ s/mm^2) (Fig. 5). Red contours derived from the DW SE reference image were superimposed onto the DW Split-echo RARE and DW ss-EPI images (Fig. 5). Difference (distortion) maps showed that DW Split-echo RARE yields close to distortion-free images at 9.4 T with a border displacement of 0.50 [0.31; 0.73] (median of 4 circles [minimum; maximum]. On the other hand, pronounced displacements 1.87 [1.37; 2.41] were observed for DW ss-EPI.

Anatomical integrity assessment of *in vivo* renal DWI. To access anatomical distortions *in vivo*, coronal slices of the rat kidney were acquired using ss-EPI and Split-echo RARE, as well as FLASH (as an anatomical reference). Similar to the phantom experiments, Split-echo RARE provided almost distortion-free images at 9.4 T as demonstrated by the distortion maps (Fig. 6). Border displacement analysis yielded BD = 0.75 [0.51; 1.30] pixels for Split-echo RARE. In contrast, the border displacement for ss-EPI was significantly ($p = 0.0006$) higher: 2.60 [1.31; 3.61] pixels (Fig. 7).

Renal *in vivo* diffusion measurements. The *in vivo* MR images (with varying b values) and corresponding parameter maps obtained with the Split-echo RARE method were of markedly better quality and showed fewer artefacts (e.g. susceptibility distortion) than those obtained with the ss-EPI (Fig. 8). Renal IVIM analysis of the *in vivo* DW Split-echo RARE data from seven animals yielded a diffusion coefficient of $D_{COR} = 1.61$ [1.34; 2.07] $\times 10^{-3}$ mm^2/s for the renal cortex, $D_{OM} = 1.78$ [1.50; 2.01] $\times 10^{-3}$ mm^2/s for the outer medulla and $D_{IM} = 1.88$ [1.75; 2.27] $\times 10^{-3}$ mm^2/s for the inner medulla. The results obtained with DW ss-EPI were similar, but varied much more between subjects (Fig. 9), as is evident from the larger difference of [minimum, maximum]: $D_{COR} = 1.57$ [1.05; 2.13] $\times 10^{-3}$ mm^2/s, $D_{OM} = 1.50$ [1.17; 2.02] $\times 10^{-3}$ mm^2/s and $D_{IM} = 1.84$ [1.72; 2.62] $\times 10^{-3}$ mm^2/s.
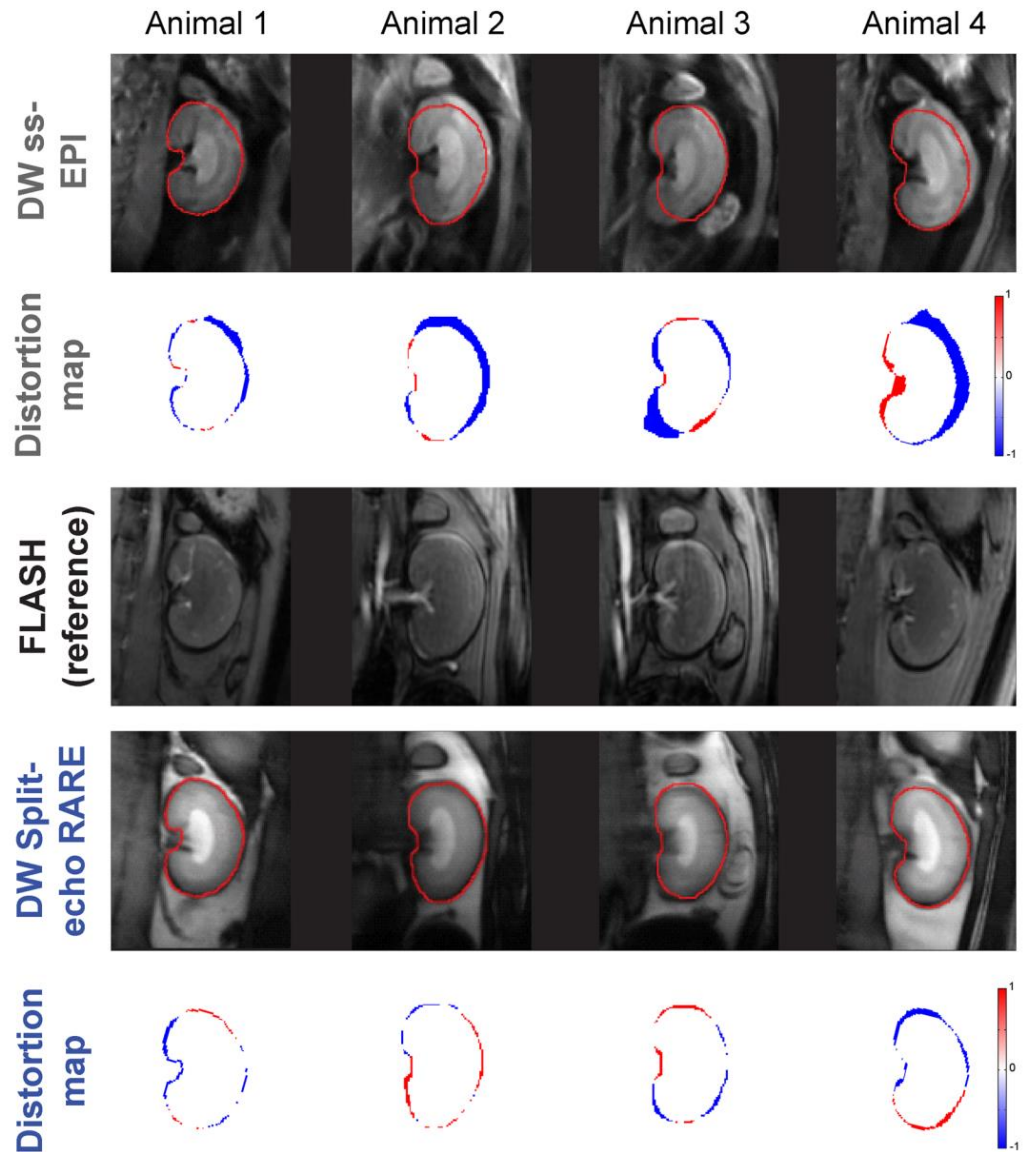
Intra-renal variability and variance. The variability (calculated as SD/mean) and variance (SD^2) of D within each renal layer were calculated as surrogates of measurement quality, based on the assumption that in a healthy kidney the water diffusion properties are similar within the tissue of a given renal layer. The plot of intra-renal diffusion variability in Fig. 10 demonstrates a smaller variability for DW Split-echo RARE (cortex: 0.104 [0.045; 0.182], outer medulla: 0.068 [0.038; 0.118], inner medulla: 0.039 [0.026; 0.081] than for DW ss-EPI (cortex: 0.181 [0.079; 0.259], outer medulla: 0.110 [0.076; 0.149], inner medulla: 0.078 [0.019; 0.093]. This effect is based on the also smaller variance for DW Split-echo RARE (cortex: 0.015, outer medulla: 0.016, inner medulla: 0.005 than for DW ss-EPI (cortex: 0.050, outer medulla: 0.025, inner medulla: 0.020).

High spatial resolution DWI. The high resolution protocol supported an in-plane spatial resolution of (0.35×0.18) mm^2 and provided excellent image quality (Fig. 11), which revealed the more subtle structures of the cortico-medullary transition with better contrast.

Discussion

In this work we demonstrate the feasibility of DW Split-echo RARE for renal diffusion weighted imaging (DWI) in small rodents at 9.4 T. We confirmed our hypothesis that DW Split-echo RARE outperforms the conventional DW ss-EPI method in terms of geometrical/anatomical integrity and measurement variability, especially in the *in vivo* experiments.

IVIM analysis of the DW Split-echo RARE data yielded mean diffusion coefficients of 1.65×10^{-3} mm^2/s in the cortex, 1.75×10^{-3} mm^2/s in the outer medulla, and 1.96×10^{-3} mm^2/s in the inner medulla. These values are

48

Figure 6. Assessment of geometric distortions *in vivo*. Coronal images of rat kidneys obtained in seven animals *in vivo* at 9.4 T using, DW ss-EPI (b = 0 mm/s²) (top row), FLASH (third row) and DW Split-echo RARE (b = 0 mm/s²) (fourth row). The respective distortion map (compared to the FLASH reference) is shown below each MR image (third and fifth row), a pseudo-color scale [−1 1] was used from blue (−1) via white to red (1). The red contour represents the border of the kidney in the FLASH reference images, which have high geometric fidelity. Border displacement was markedly smaller with DW Split-echo RARE than with DW ss-EPI.

consistent with those reported in the literature when using DW-EPI[51–53]. Results obtained from ss-EPI images were similar to those derived from DW Split-echo RARE but showed a larger variability, especially in the outer and inner medulla. This is probably due to the image artifacts that are observed with ss-EPI. The lower variability and variance in the diffusion coefficients increases the effect size (standardized mean difference between two groups) and hence the statistical power to detect small pathophysiological changes, e.g., in x-ray contrast medium-induced AKI, or during initial stages of diabetic kidney disease.

Anatomical integrity was excellent for the Split-echo RARE technique, and far superior to the ss-EPI approach, which resulted in 3.5-fold larger border displacements for ss-EPI. Severe geometric distortions in the presence of magnet field inhomogeneities are expected with EPI, due to its low effective readout bandwidth in phase encoding direction. Echo-planar imaging variants are commonly used for renal DWI but are prone to magnetic susceptibility artifacts induced by the air-filled bowels, cavities and tissue interfaces surrounding the kidneys. Susceptibility artifacts compromise the anatomical integrity of DWI EPI kidney images and are even prevalent at lower magnetic field strengths[46,54,55]. Typically, images with severe distortions that cannot be corrected have to be eliminated from analyses. Due to complexity of non-linear geometric distortions, it is conceivable that such distortions might introduce errors when using (semi)
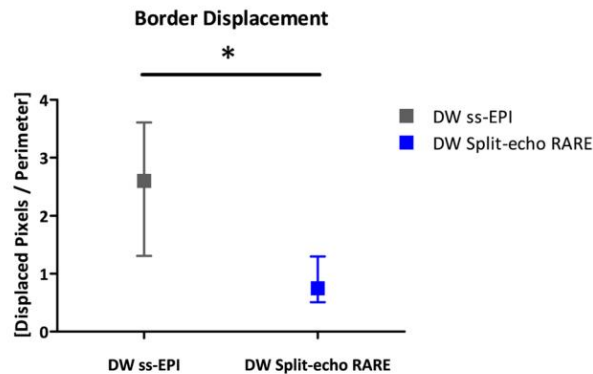
Figure 7. Quantification of border displacement analysis and comparison between DW methods. The median of the measured border displacement (arbitrary units) for DW ss-EPI was significantly larger ($p < 0.05$) than that for the proposed DW Split-echo RARE approach, the error bars indicate minimum and maximum value.
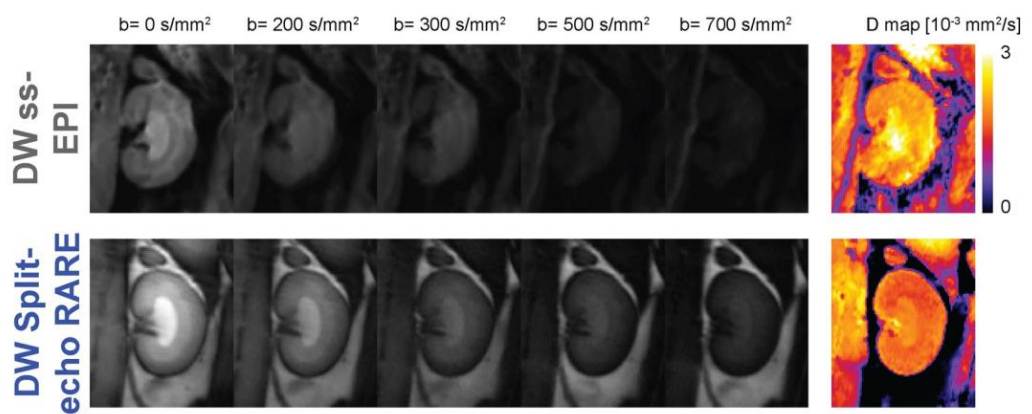


Figure 8. IVIM images examples and corresponding diffusion maps. Images of a rat kidney acquired at 9.4 T with diffusion weightings raging from (0 to 700 s/mm^2) using the conventional DW ss-EPI (top row) or the DW Split-echo RARE (bottom row) method within a total acquisition time of 4.5 minutes. Respective parameter maps of the diffusion coefficient are shown in the right column, a pseudo-color scale [0 3] was used from black (0) via purple, red, orange, yellow to white (3). The quality of the MR images and parameter map was markedly better with DW Split-echo RARE compared with DW ss-EPI in all seven animals.
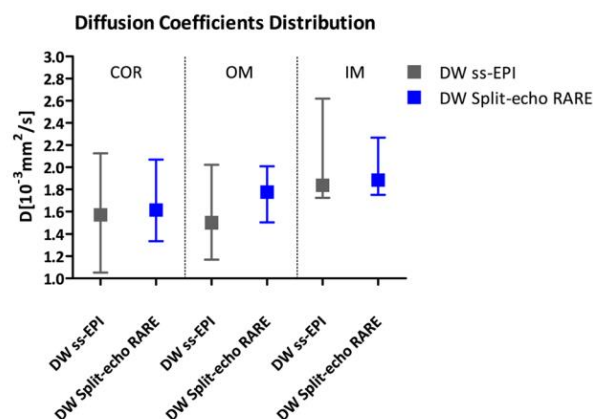
Figure 9. Comparison of D for the renal cortex (COR), outer medulla (OM) and inner medulla (IM) and comparison between DW methods. Data were obtained from seven rats. D median (using DW ss-EPI (grey), D median using DW Split-echo RARE (blue) for each different region on the kidney: COR, OM and IM. The error bars indicate minimum and maximum value. DW Split-echo RARE yielded for all renal compartments a smaller [minimum; maximum] range than the obtained with DW ss-EPI.

50
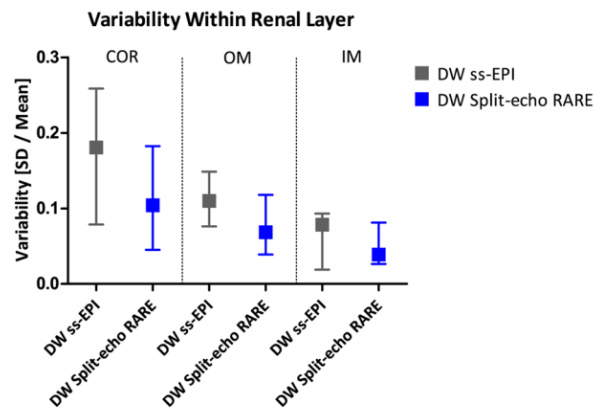
Figure 10. Diffusion variability within each renal layer. Variability [SD/Mean] within the different layers, i.e. cortex (COR), outer medulla (OM), and inner medulla (IM) was calculated as a surrogate of measurement quality. Variability median (using DW ss-EPI (grey), Variability median using DW Split-echo RARE (blue) for each different region on the kidney: COR, OM and IM. The error bars indicate minimum and maximum value. DW Split-echo RARE yielded for all renal compartments a smaller median and [minimum; maximum] range than the obtained with DW ss-EPI.
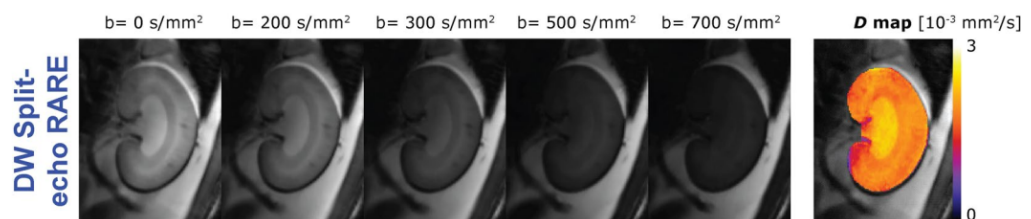
Figure 11. High-spatial resolution IVIM images and diffusion map. DW Split-echo RARE images of a rat kidney acquired *in vivo* at 9.4 T using the high spatial resolution protocol and diffusion weightings of b = 0 to 700 s/mm², together with the respective *D* map, a pseudo-color scale [0 3] was used from black (0) via purple, red, orange, yellow to white (3). The excellent image/map quality obtained with this 18-minute scan makes the DW Split-echo RARE approach attractive for renal steady-state MRI experiments, such as in CKD models.

automated analysis techniques that assume a certain kidney morphology (e.g. the morphology-based placement of ROIs[34,35] or the Twelve-Layer Concentric Objects (TLCO) technique[33]). Yet, these detrimental effects may be reduced when large ROIs are used. Taken together, anatomical distortions can lead to increased variability and even unusable data, which in turn hamper intra- and inter-subject comparisons, and may compromise the statistical power of group analyses. Hence, keeping a good anatomical integrity in DWI is critical in order to achieve reliable results in the healthy as well as diseased kidneys – this is the forte of spin-echo-based techniques such as RARE.

Strategies for reducing geometric distortions resulting from predominantly gradient-echo-based EPI include image registration/unwarping. However, their practical use is somewhat limited, as outlined in the following. Registration of images containing geometric distortions is challenging, since it requires good image contrast and high degrees of freedom. In principle, unwarping (correction of susceptibility-induced distortions) can be done when additional field maps are acquired, however this is not trivial for strongly warped regions that lack a unique solution. Furthermore, unwarping will not be accurate if the distortions change during the relatively long DWI scan.

Segmentation of data collection, i.e. multi-shot acquisition, is another approach to reduce geometric distortions. Segmentation in phase-encoding direction can be applied in a common DW EPI protocol, but segmentation in readout direction requires a dedicated sequence. Readout segmented EPI (rs-EPI) in association with parallel imaging has been shown to reduce susceptibility artifacts in DWI[31,56–59], improve renal DWI quality[55], and correlate better with renal fibrosis[54]. One major drawback of segmented acquisitions is the associated longer acquisition times. Dividing the acquisition into 2 (or 4) segments already doubles (or quadruples) the acquisition duration. Increasing scan time for DWI — that already requires repeated acquisitions for different diffusion weightings and directions — represents a limitation in preclinical studies of physiological dynamics and in clinical routine use. Motion between the acquisitions of different segments in phase-encoding direction can create substantial artifacts. To diminish the shot-dependent nonlinear phase differences that arise from non-rigid motion, navigator readout segments need to be acquired repeatedly throughout the scan. Even though one could argue that the image quality of both, EPI and RARE, benefits significantly from segmentation, and hence multi-shot RARE suffers from the same time-constraints as rs-EPI, we have previously shown that even readout-segmented-EPI is less effective than ultrafast unsegmented RARE approaches for DWI in terms of restoring anatomical integrity[60].

51

The use of refocusing pulses in RARE comes with an increase in the inter-echo time resulting in an increase in the echo train length versus EPI. Therefore the echo-train length used in RARE should receive attention when designing the imaging protocol and should not substantially exceed the T_2 relaxation time of the object under investigation to avoid smearing artifacts along the phase encoding direction which may otherwise impair the ADC assessment. Imaging speed and RF power deposition are also recognized limitations of RARE when compared to EPI. To offset these constraints, Combined Acquisition Techniques (CAT)[61] has been applied to boost imaging speed and reduce RF power deposition by using a modular hybrid approach that integrates a minimum of two imaging strategies. RARE-EPI CAT hybrids have been implemented for abdominal imaging[62] and could hold the promise to further improve renal DWI at (ultra)high fields by combining of advantages of RARE (anatomical integrity) with those of EPI (imaging speed and less RF power deposition). The proposed Split-echo RARE approach is compatible with segmented acquisitions. To address potential motion induced phase changes, Split-echo RARE can be combined with the navigator echo approach[31]. To further enhance imaging speed, single shot and segmented Split-echo RARE can be supported by multiband RF pulses facilitating simultaneous multi-slice imaging. A recently developed multiplexed sensitivity encoding approach[63] is also compatible with Split-echo RARE and affords reconstruction of multi-shot DWI data without the need of navigator echoes.

In our present study we made an experimental comparison between single-shot EPI and RARE protocols using the same short acquisition times. A thorough comparison between both fast protocols is critical for dynamic preclinical studies and when translating DWI into clinical situations that are highly dependent on imaging speed. In scenarios where temporal resolution is less crucial, a segmented approach may be introduced to (i) reduce the point spread function related blurring observed when using RARE with high echo-train-lengths (due to the effect of the T_2-decay on the point-spread-function and the inter-echo time), and (ii) reduce geometric distortions in EPI but may also require additional navigator-based motion correction.

The current Split-echo RARE implementation uses a pair of unipolar Stejskal-Tanner gradients[48], which helps to balance diffusion sensitization time and diffusion sensitization strength. However, pairs of unipolar gradients are not motion compensated and can be prone to eddy current related artifacts. Pairs of bipolar diffusion sensitizing gradients or twice-refocused gradients offer those features but come with a less effective sensitization[40,64,65]. Here, we chose a Split-echo approach using an imbalance in the readout gradient in order to preserve signal-to-noise ratio (SNR). With the Split-echo approach the spatial resolution along the read-out direction is only half of the displaced echo approach, which presents an alternative for avoiding interferences between odd and even echo groups[36,41].

To conclude, this study demonstrates that Split-echo RARE has the capability to acquire distortion-free diffusion-weighted images of the rat kidney at ultrahigh magnetic field strengths. Improving anatomical integrity in DWI is a further step towards advancing the capabilities and robustness of parametric imaging of the kidney. It facilitates the use of semi-automated analysis methods that place ROIs reproducibly at clearly defined locations within the kidney based on kidney border information[33–35]. Identification of the kidney boundary is usually done manually[33], which inevitably adds inter-observer variability to the results. A very valuable refinement to renal DWI would be the use of automated kidney segmentation methods such as the appearance-guided deformable boundary technique, which was recently shown to perform better than several alternative methods[66]. All these (semi-)automated approaches are important directions for further developments, as they help to eliminate any bias introduced by subjective manual interaction.

Adding robust DWI protocols to other MRI-based methods of tissue characterization of the kidney will further assist the non-invasive interrogation and phenotyping of small rodents during physiological interventions or pathological scenarios. Ultimately, the translational approach of the proposed Split-echo RARE method may be exploited for detecting and quantifying early renal disease in patients as well as studying disease mechanisms and renoprotective strategies in the future.

References

1. Zuk, A. & Bonventre, J. V. Acute kidney injury. *Annual review of medicine* **67**, 293–307 (2016).
2. Thakar, C. V., Christianson, A., Freyberg, R., Almenoff, P. & Render, M. L. Incidence and outcomes of acute kidney injury in intensive care units: a Veterans Administration study. *Critical care medicine* **37**, 2552–2558, https://doi.org/10.1097/CCM.0b013e3181a5906f (2009).
3. Thakar, C. V. Perioperative acute kidney injury. *Advances in chronic kidney disease* **20**, 67–75, https://doi.org/10.1053/j.ackd.2012.10.003 (2013).
4. Ali, T. *et al*. Incidence and outcomes in acute kidney injury: a comprehensive population-based study. *Journal of the American Society of Nephrology: JASN* **18**, 1292–1298, https://doi.org/10.1681/ASN.2006070756 (2007).
5. Zarjou, A., Sanders, P. W., Mehta, R. L. & Agarwal, A. Enabling innovative translational research in acute kidney injury. *Clinical and translational science* **5**, 93–101, https://doi.org/10.1111/j.1752-8062.2011.00302.x (2012).
6. Evans, R. G. & O'Connor, P. M. Initiation and progression of chronic kidney disease: can we definitively test the chronic hypoxia hypothesis? *Hypertension* **62**, 827–828, https://doi.org/10.1161/HYPERTENSIONAHA.113.02047 (2013).
7. Persson, P. B. Renoprotection. *Acta Physiologica* **219**, 540–541, https://doi.org/10.1111/apha.12683 (2017).
8. Matejovic, M. *et al*. Renal Hemodynamics in AKI: In Search of New Treatment Targets. *Journal of the American Society of Nephrology: JASN* **27**, 49–58, https://doi.org/10.1681/ASN.2015030234 (2016).
9. Khwaja, A. KDIGO clinical practice guidelines for acute kidney injury. *Nephron. Clinical practice* **120**, c179–184, https://doi.org/10.1159/000339789 (2012).
10. Molitoris, B. A. Urinary Biomarkers: Alone Are They Enough? *Journal of the American Society of Nephrology: JASN* **26**, 1485–1488, https://doi.org/10.1681/ASN.2014111145 (2015).
11. Selby, N. M. *et al*. Magnetic resonance imaging biomarkers for chronic kidney disease: a position paper from the European Cooperation in Science and Technology Action PARENCHIMA. Nephrology Dialysis Transplantation 33, https://doi.org/10.1093/ndt/gfy152 (2018).

52

12. Abdeltawab, H. *et al*. A Novel CNN-Based CAD system for early Assessment of transplanted Kidney Dysfunction. *Scientific reports* **9.1**, 5948 (2019).
13. Hueper, K. *et al*. T2 Relaxation Time and Apparent Diffusion Coefficient for Noninvasive Assessment of Renal Pathology After Acute Kidney Injury in Mice Comparison With Histopathology. 48 (2013).
14. Kang, S. K. *et al*. DWI for renal mass characterization: Systematic review and meta-analysis of diagnostic test performance. *American Journal of Roentgenology* **205**, 317–324, https://doi.org/10.2214/ajr.14.13930 (2015).
15. Aslan, M. *et al*. Diffusion-weighted MRI for differentiating Wilms tumor from neuroblastoma. *Diagnostic and Interventional Radiology* **23**, 403–406, https://doi.org/10.5152/dir.2017.16541 (2017).
16. Lei, Y. *et al*. Diagnostic Significance of Diffusion-Weighted MRI in Renal Cancer. *BioMed Research International* **2015**, 1–12, https://doi.org/10.1155/2015/172165 (2015).
17. Zhang, W. *et al*. HHS Public Access. 133, 48–61, https://doi.org/10.1161/CIRCULATIONAHA.115.017472.Critical (2017).
18. Zhu, Q. *et al*. Value of intravoxel incoherent motion for differential diagnosis of renal tumors. *Acta Radiol* **60**, 382–387, https://doi.org/10.1177/0284185118778884 (2019).
19. Attariwala, R. & Picker, W. Whole body MRI: Improved lesion detection and characterization with diffusion weighted techniques. *Journal of Magnetic Resonance Imaging* **38**, 253–268, https://doi.org/10.1002/jmri.24285 (2013).
20. Zhang, Y. L. *et al*. EADC Values in Diagnosis of Renal Lesions by 3.0 T Diffusion-Weighted Magnetic Resonance Imaging: Compared with the ADC Values. *Applied Magnetic Resonance* **44**, 349–363, https://doi.org/10.1007/s00723-012-0376-z (2013).
21. Franke, M. *et al*. Magnetic resonance T2 mapping and diffusion-weighted imaging for early detection of cystogenesis and response to therapy in a mouse model of polycystic kidney disease. *Kidney International* **92**, 1544–1554, https://doi.org/10.1016/j.kint.2017.05.024 (2017).
22. Friedli, I. *et al*. New Magnetic Resonance Imaging Index for Renal Fibrosis Assessment: A Comparison between Diffusion-Weighted Imaging and T1 Mapping with Histological Validation. *Scientific Reports* **6**, 1–15, https://doi.org/10.1038/srep30088 (2016).
23. Zhao, J. *et al*. Assessment of renal fibrosis in chronic kidney disease using diffusion-weighted MRI. *Clinical Radiology* **69**, 1117–1122, https://doi.org/10.1016/j.crad.2014.06.011 (2014).
24. Mao, W. *et al*. Intravoxel incoherent motion diffusion-weighted imaging for the assessment of renal fibrosis of chronic kidney disease: A preliminary study. *Magnetic Resonance Imaging* **47**, 118–124, https://doi.org/10.1016/j.mri.2017.12.010 (2018).
25. Cai, X. R. *et al*. Use of intravoxel incoherent motion MRI to assess renal fibrosis in a rat model of unilateral ureteral obstruction. *Journal of Magnetic Resonance Imaging* **44**, 698–706, https://doi.org/10.1002/jmri.25172 (2016).
26. Hueper, K. *et al*. Diffusion-Weighted imaging and diffusion tensor imaging detect delayed graft function and correlate with allograft fibrosis in patients early after kidney transplantation. *Journal of Magnetic Resonance Imaging* **44**, 112–121, https://doi.org/10.1002/jmri.25158 (2016).
27. Xie, Y. *et al*. Functional evaluation of transplanted kidneys with reduced field-of-view diffusion-weighted imaging at 3T. *Korean Journal of Radiology* **19**, 201–208, https://doi.org/10.3348/kjr.2018.19.2.201 (2018).
28. Feng, Y. Z. *et al*. Intravoxel incoherent motion (IVIM) at 3.0 T: evaluation of early renal function changes in type 2 diabetic patients. *Abdom Radiol (NY)* **43**, 2764–2773, https://doi.org/10.1007/s00261-018-1555-7 (2018).
29. Liang, L. *et al*. Using intravoxel incoherent motion MR imaging to study the renal pathophysiological process of contrast-induced acute kidney injury in rats: Comparison with conventional DWI and arterial spin labelling. *Eur Radiol* **26**, 1597–1605, https://doi.org/10.1007/s00330-015-3990-y (2016).
30. Mao, W. *et al*. Chronic kidney disease: Pathological and functional evaluation with intravoxel incoherent motion diffusion-weighted imaging. *J Magn Reson Imaging* **47**, 1251–1259, https://doi.org/10.1002/jmri.25861 (2018).
31. Paul, K. *et al*. Diffusion-sensitized ophthalmic magnetic resonance imaging free of geometric distortion at 3.0 and 7.0 T: a feasibility study in healthy subjects and patients with intraocular masses. *Invest Radiol* **50**, 309–321 (2015).
32. Piskunowicz, M. *et al*. A new technique with high reproducibility to estimate renal oxygenation using BOLD-MRI in chronic kidney disease. *Magn Reson Imaging* **33**, 253–261, https://doi.org/10.1016/j.mri.2014.12.002 (2015).
33. Milani, B. *et al*. Reduction of cortical oxygenation in chronic kidney disease: evidence obtained with a new analysis method of blood oxygenation level-dependent magnetic resonance imaging. *Nephrology Dialysis Transplantation* **32**, 2097–2105 (2016).
34. Pohlmann, A. *et al*. High temporal resolution parametric MRI monitoring of the initial ischemia/reperfusion phase in experimental acute kidney injury. *PLoS One* **8**, e57411, https://doi.org/10.1371/journal.pone.0057411 (2013).
35. Pohlmann, A. *et al*. Experimental MRI Monitoring of Renal Blood Volume Fraction Variations En Route to Renal Magnetic Resonance Oximetry. *Tomography* **3**, 188–200, https://doi.org/10.18383/j.tom.2017.00012 (2017).
36. Norris, D. G. Ultrafast low-angle RARE: U-FLARE. *Magn Reson Med* **17**, 539–542 (1991).
37. Norris, D. G., Bornert, P., Reese, T. & Leibfritz, D. On the application of ultra-fast RARE experiments. *Magn Reson Med* **27**, 142–164 (1992).
38. Norris, D. G. & Bornert, P. Coherence and Interference in Ultrafast RARE Experiments. *Journal of Magnetic Resonance* **105**, 123–127 (1993).
39. Niendorf, T., Norris, D. G. & Leibfritz, D. Detection of apparent restricted diffusion in healthy rat brain at short diffusion times. *Magnetic Resonance in Medicine* **32**, 672–677 (1994).
40. Niendorf, T., Dijkhuizen, R. M., Norris, D. G., Van Lookeren Campagne, M. & Nicolay, K. Biexponential diffusion attenuation in various states of brain tissue: Implications for diffusion-weighted imaging. *Magnetic Resonance in Medicine* **36**, 847–857, https://doi.org/10.1002/mrm.1910360607 (1996).
41. Niendorf, T. On the application of susceptibility-weighted ultra-fast low-angle RARE experiments in functional MR imaging. *Magn Reson Med* **41**, 1189–1198 (1999).
42. Heinrichs, U. *et al*. Myocardial T_2^* mapping free of distortion using susceptibility-weighted fast spin-echo imaging: a feasibility study at 1.5 T and 3.0 T. *Magn Reson Med* **62**, 822–828, https://doi.org/10.1002/mrm.22054 (2009).
43. Utting, J. F. *et al*. Feasibility of k-t BLAST For BOLD fMRI With a Spin-Echo Based Acquisition at 3 T and 7 T. *Investigative Radiology* 44 (2009).
44. Hennig, J., Nauerth, A. & Friedburg, H. RARE imaging: a fast imaging method for clinical MR. *Magn Reson Med* **3**, 823–833 (1986).
45. Jin, N. *et al*. Targeted single-shot methods for diffusion-weighted imaging in the kidneys. *J Magn Reson Imaging* **33**, 1517–1525, https://doi.org/10.1002/jmri.22556 (2011).
46. Hilbert, F. *et al*. Comparison of Turbo Spin Echo and Echo Planar Imaging for intravoxel incoherent motion and diffusion tensor imaging of the kidney at 3Tesla. *Z Med Phys* **27**, 193–201, https://doi.org/10.1016/j.zemedi.2016.12.001 (2017).
47. Williams, C. F. M., Redpath, T. W. & Norris, D. G. A novel fast split-echo multi-shot diffusion-weighted MRI method using navigator echoes. *Magnetic Resonance in Medicine* **41**, 734–742 (1999).
48. Stejskal, E. O. & Tanner, J. E. Spin Diffusion Measurements: Spin Echoes in the Presence of a Time-Dependent Field Gradient. *The Journal of Chemical Physics* **42**, 288–292, https://doi.org/10.1063/1.1695690 (1965).
49. Alsop, D. C. Phase insensitive preparation of single-shot RARE: application to diffusion imaging in humans. *Magn Reson Med* **38**, 527–533 (1997).
50. Pohlmann, A. *et al*. Detailing the relation between renal T2* and renal tissue pO2 using an integrated approach of parametric magnetic resonance imaging and invasive physiological measurements. *Invest Radiol* **49**, 547–560 (2014).
51. Notohamiprodjo, M. *et al*. Combined intravoxel incoherent motion and diffusion tensor imaging of renal diffusion and flow anisotropy. *Magn Reson Med* **73**, 1526–1532, https://doi.org/10.1002/mrm.25245 (2015).

53

52. Zhang, X., Ingo, C., Teeuwisse, W. M., Chen, Z. & van Osch, M. J. P. Comparison of perfusion signal acquired by arterial spin labeling-prepared intravoxel incoherent motion (IVIM) MRI and conventional IVIM MRI to unravel the origin of the IVIM signal. *Magn Reson Med* **79**, 723–729, https://doi.org/10.1002/mrm.26723 (2018).
53. Zhang, B. *et al.* Application of noninvasive functional imaging to monitor the progressive changes in kidney diffusion and perfusion in contrast-induced acute kidney injury rats at 3.0 T. *Abdom Radiol (NY)* **43**, 655–662, https://doi.org/10.1007/s00261-017-1247-8 (2018).
54. Friedli, I. *et al.* Comparison of readout-segmented and conventional single-shot for echo-planar diffusion-weighted imaging in the assessment of kidney interstitial fibrosis. *J Magn Reson Imaging* **46**, 1631–1640, https://doi.org/10.1002/jmri.25687 (2017).
55. Friedli, I. *et al.* Improvement of renal diffusion-weighted magnetic resonance imaging with readout-segmented echo-planar imaging at 3T. *Magn Reson Imaging* **33**, 701–708, https://doi.org/10.1016/j.mri.2015.02.023 (2015).
56. Kim, S. G., Hu, X., Adriany, G. & Uğurbil, K. Fast interleaved echo-planar imaging with navigator: high resolution anatomic and functional images at 4 Tesla. *Magn Reson Med* **35**, 895–902, https://doi.org/10.1002/mrm.1910350618 (1996).
57. Jezzard, P. Correction of geometric distortion in fMRI data. *Neuroimage* **62**, 648–651, https://doi.org/10.1016/j.neuroimage.2011.09.010 (2012).
58. Holdsworth, S. J. *et al.* Readout-segmented EPI for rapid high resolution diffusion imaging at 3T. *European Journal of Radiology* **65**, 36–46 (2008).
59. Porter, D. A. & Heidemann, R. M. High resolution diffusion-weighted imaging using readout-segmented echo-planar imaging, parallel imaging and a two-dimensional navigator-based reacquisition. *Magn Reson Med* **62**, 468–475, https://doi.org/10.1002/mrm.22024 (2009).
60. Heidemann, R. M. *et al.* Diffusion imaging in humans at 7T using readout-segmented EPI and GRAPPA. *Magn Reson Med* **64**, 9–14, https://doi.org/10.1002/mrm.22480 (2010).
61. Hillenbrand, C., Hahn, D., Haase, A. & Jakob, P. M. MR CAT scan: a modular approach for hybrid imaging. *MAGMA* **10**, 183–199, https://doi.org/10.1007/bf02590645 (2000).
62. Jakob, P., Hillenbrand, C. M., Kenn, W., Hahn, D. & Haase, A. Abdominal imaging with a modular combination of spin and gradient echoes. *Magnetic Resonance in Medicine: An Official Journal of the International Society for Magnetic Resonance in Medicine* **47**, 425–432 (2002).
63. Chen, N.-kuei *et al.* A robust multi-shot scan strategy for high-resolution diffusion weighted MRI enabled by multiplexed sensitivity-encoding (MUSE). *Neuroimage* **72**, 41–47 (2013).
64. Hong, X. & Thomas Dixon, W. Measuring diffusion in inhomogeneous systems in imaging mode using antisymmetric sensitizing gradients. *Journal of Magnetic Resonance* **99**, 561–570, https://doi.org/10.1016/0022-2364(92)90210-x (1992).
65. Reese, T. G., Heid, O., Weisskoff, R. M. & Wedeen, V. J. Reduction of eddy-current-induced distortion in diffusion MRI using a twice-refocused spin echo. *Magn Reson Med* **49**, 177–182, https://doi.org/10.1002/mrm.10308 (2003).
66. Shehata, M. *et al.* 3D kidney segmentation from abdominal diffusion MRI using an appearance-guided deformable boundary. *PloS one* **13**(7), e0200082 (2018).
67. Deoni, P. Quantitative diffusion imaging with steady-state free precession. *Magnetic Resonance in Medicine* **51**(2), 428–433 (2004).
68. Landolt, Zahlenwerte und Funktionen aus Physik, Chemie, Astronomie, Geophysik und Technik. Berlin Heidelberg New York: Springer-Verlag (1969).
69. Como, G. Relevance of b -values in evaluating liver fibrosis: A study in healthy and cirrhotic subjects using two single-shot spin-echo echo-planar diffusion-weighted sequences. *Journal of Magnetic Resonance Imaging* **28**(2), 411–419 (2008).
70. Schick, F. SPLICE: Sub-second diffusion-sensitive MR imaging using a modified fast spin-echo acquisition mode. *Magnetic Resonance in Medicine* **38**, 638–644, https://doi.org/10.1002/mrm.1910380418 (1997).

Acknowledgements

Author contributions

J.P., A.P., T.N., M.K., E.S., and B.F. conceived and designed the experiments. J.P. and A.P. performed the experiments and analyzed the data. J.P., A.P., K.P., T.H., M.K., Y.J., K.C., T.G., D.G., and E.S. contributed reagents/materials/analysis tools. J.P., A.P., T.N., M.K., and S.W. wrote the paper. All authors reviewed the manuscript.

Competing interests

The authors declare no competing interests.

Additional information

Supplementary information is available for this paper at https://doi.org/10.1038/s41598-019-56184-6.

Correspondence and requests for materials should be addressed to A.P.

Reprints and permissions information is available at www.nature.com/reprints.

Publisher's note Springer Nature remains neutral with regard to jurisdictional claims in published maps and institutional affiliations.

54

Original Article

Continuous diffusion spectrum computation for diffusion-weighted magnetic resonance imaging of the kidney tubule system

João S. Periquito[1,2,3#^], Thomas Gladytz[1#], Jason M. Millward[1^], Paula Ramos Delgado[1,3^], Kathleen Cantow[2^], Dirk Grosenick[4], Luis Hummel[2^], Ariane Anger[2], Kaixuan Zhao[1^], Erdmann Seeliger[2^], Andreas Pohlmann[1^], Sonia Waiczies[1^], Thoralf Niendorf[1,3^]

[1]Berlin Ultrahigh Field Facility (B.U.F.F.), Max Delbrück Center for Molecular Medicine in the Helmholtz Association, Berlin, Germany; [2]Institute of Physiology, Charité - Universitätsmedizin Berlin, Campus Mitte, Berlin, Germany; [3]Experimental and Clinical Research Center, a Joint Cooperation between the Charité Medical Faculty and the Max Delbrück Center for Molecular Medicine in the Helmholtz Association, Berlin, Germany; [4]Physikalisch-Technische Bundesanstalt (PTB), Berlin, Germany

[#]These authors contributed equally to this work.

Correspondence to: Prof. Dr. Thoralf Niendorf. Max Delbrück Center for Molecular Medicine in the Helmholtz Association, Robert-Rössle-Str. 10, 13125 Berlin, Germany. Email: thoralf.niendorf@mdc-berlin.de.

Background: The use of rigid multi-exponential models (with *a priori* predefined numbers of components) is common practice for diffusion-weighted MRI (DWI) analysis of the kidney. This approach may not accurately reflect renal microstructure, as the data are forced to conform to the *a priori* assumptions of simplified models. This work examines the feasibility of less constrained, data-driven non-negative least squares (NNLS) continuum modelling for DWI of the kidney tubule system in simulations that include emulations of pathophysiological conditions.

Methods: Non-linear least squares (LS) fitting was used as reference for the simulations. For performance assessment, a threshold of 5% or 10% for the mean absolute percentage error (MAPE) of NNLS and LS results was used. As ground truth, a tri-exponential model using defined volume fractions and diffusion coefficients for each renal compartment (tubule system: $D_{tubules}$, $f_{tubules}$; renal tissue: D_{tissue}, f_{tissue}; renal blood: D_{blood}, f_{blood}) was applied. The impact of: (I) signal-to-noise ratio (SNR) =40–1,000, (II) number of b-values (n=10–50), (III) diffusion weighting (b-range$_{small}$ =0–800 up to b-range$_{large}$ =0–2,180 s/mm^2), and (IV) fixation of the diffusion coefficients D_{tissue} and D_{blood} was examined. NNLS was evaluated for baseline and pathophysiological conditions, namely increased tubular volume fraction (ITV) and renal fibrosis (10%: grade I, mild) and 30% (grade II, moderate).

Results: NNLS showed the same high degree of reliability as the non-linear LS. MAPE of the tubular volume fraction ($f_{tubules}$) decreased with increasing SNR. Increasing the number of b-values was beneficial for $f_{tubules}$ precision. Using the b-range$_{large}$ led to a decrease in MAPE$_{ftubules}$ compared to b-range$_{small}$. The use of a medium b-value range of b=0–1,380 s/mm^2 improved $f_{tubules}$ precision, and further b_{max} increases beyond this range yielded diminishing improvements. Fixing D_{blood} and D_{tissue} significantly reduced MAPE$_{ftubules}$ and provided near perfect distinction between baseline and ITV conditions. Without constraining the number of renal compartments in advance, NNLS was able to detect the (fourth) fibrotic compartment, to differentiate it from the other three diffusion components, and to distinguish between 10% *vs.* 30% fibrosis.

Conclusions: This work demonstrates the feasibility of NNLS modelling for DWI of the kidney tubule

^ ORCID: João S. Periquito, 0000-0003-3702-9264; Jason M. Millward, 0000-0003-4484-2798; Paula Ramos Delgado, 0000-0003-2009-3024; Kathleen Cantow, 0000-0002-3907-6315; Luis Hummel, 0000-0002-6613-6029; Kaixuan Zhao, 0000-0003-4769-7477; Erdmann Seeliger, 0000-0002-5685-8044; Andreas Pohlmann, 0000-0002-8572-2568; Sonia Waiczies, 0000-0002-9916-9572; Thoralf Niendorf, 0000-0001-7584-6527.

system and shows its potential for examining diffusion compartments associated with renal pathophysiology including ITV fraction and different degrees of fibrosis.

Introduction

Kidney diseases are a major health issue, with increasing incidence and an estimated two million deaths per year worldwide due to acute kidney injury (AKI) (1-7). While several biomarkers are currently being investigated for diagnosis of AKI, to date clinical point-of-care biomarkers for AKI are still lacking (8-11). To address this urgent unmet clinical need, MRI may provide quantitative imaging markers to inform on the different stages of pathophysiology, improve prediction and interception of disease progression and evaluate treatment of AKI (6,12-20).

The renal tubules are a unique anatomical compartment of the kidney, comprising a large fraction of the renal volume. The tubular volume fraction can change due to (I) changes in the glomerular filtration rate, (II) alterations in tubular outflow towards and beyond the renal pelvis, (III) modulation of the transmural pressure gradient and (IV) changes in tubular fluid resorption (21). The tubular volume fraction may develop into a novel marker for clinical diagnostics of kidney diseases, for two reasons. First, MR-based assessment of the tubular volume fraction could serve as a diagnostic tool, for instance to detect glomerular hyperfiltration—a hallmark of early-stage diabetic nephropathy (22). It may also help in the distinction between AKI that is caused by obstructions of the urinary tract and AKI of other origins (23). Tubular atrophy and interstitial fibrosis play a major role in the microstructural changes occurring during kidney pathology e.g., renal allograft injury (24). Being able to assess renal fibrosis and alterations in the tubular volume fraction with non-invasive MRI would be clinically valuable (3,7,22,23,25-28). Second, as the renal capsule is comparatively rigid, changes in the tubular volume fraction will result in opposite changes in the renal blood volume fraction, thereby confounding the relationship between renal blood oxygenation level-dependent (BOLD) T_2^*, oxygen saturation of hemoglobin, and tissue partial pressure of oxygen (21,29). Concomitant assessment of the tubular volume fraction will thus help to

accurately interpret quantitative renal T_2^* data.

Diffusion-weighted MRI (DWI) probes self-diffusion of water in tissue on a microscopic level and reflects micro-morphological and (patho)physiological changes in renal tissue and renal diseases (30,31). When performing DWI of the kidney, the incoherent blood flow in the renal microvasculature contributes to pseudo-diffusion (32-38) resulting in a fast signal decay component. The displacement of water molecules in the renal tissue contributes a slow water diffusion component, according to the two-compartment model (32-38). Acknowledging the morphological and physiological importance of renal tubules, recent studies have shown that the intra-tubular fluid compartment introduces a third component in the renal DWI signal decay. To account for this tubular water diffusion component, a rigid tri-exponential model was proposed to better decipher diffusion MRI signals from the kidney (39,40).

The performance of rigid multi-exponential models is often highly dependent on initial values, and on the upper and lower boundaries of the optimization parameters (41). Fixing some coefficients of the rigid model is common practice to increase fit stability and to improve the sensitivity to physiological changes. This applies particularly to tri-exponential models (with six variables to fit) but runs the risk of introducing a bias (40). To address this limitation, an unbiased data-driven analysis of the diffusion signal decay is required. Non-negative least squares (NNLS) continuum modelling provides an alternative to rigid model fitting techniques, which does not require *a priori* assumptions of the number of components of the signal decay nor starting values (42-44). A predefined basis set of more than 500 exponential components spanning the entire range of feasible diffusion coefficients can be used as input to the NNLS algorithm. As output, the NNLS continuum modelling yields a spectrum of the contributions of all exponential basis vectors to the signal decay. NNLS continuum modelling can be a useful tool to determine the

number of major diffusion compartments actually present in the tissue, and offers a means for their quantification during (patho)physiological changes (43). It has been successfully employed for multicomponent diffusion analysis of microstructural alterations in multicellular tumor spheroids, bone marrow, the central nervous system, and liver as well as in the parenchyma of healthy organs of the upper abdomen (32,45-52).

Notwithstanding this pioneering work, the literature does not include reports on a systematic examination of the performance of NNLS-based multicomponent diffusion analysis of microstructural alterations in the kidney. Recognizing the opportunity and challenges of this task, this work presents a simulation study focusing on NNLS computation for DWI of the kidney tubule system. Such simulations are a crucial precursor to *in vivo* studies, in order to establish the optimal selection of experimental parameters, and to estimate effect sizes for power analysis to ensure appropriate sample sizes of experimental animals. Our numerical simulations center on three metrics including (I) the signal-to-noise ratio (SNR), (II) the number of data points needed for the characterization of the diffusion signal decay, and (III) the range of diffusion sensitization (b-value range), which are essential for renal DWI applications. To meet this objective, detailed numerical simulations were conducted with the goal to optimize renal DWI parameters in order for the NNLS continuum modelling to provide an error of less than 5% and 10%, for the assessment of tubular fluid, intrarenal blood, and renal tissue volume fractions. As ground truth, a tri-exponential and a four-exponential function using defined volume fractions and diffusion coefficients for each renal compartment were applied for baseline renal tissue conditions. To approach a pathophysiological scenario, NNLS continuum modelling was evaluated for conditions that mimic an increase in tubular volume fraction and different degrees of renal fibrosis.

Methods

Multi-compartment model

Two-compartment (bi-exponential) models generally used for representing DWI data of organs other than the kidney were recently shown to be unsuitable for fully representing renal DWI data, as they neglect the impact of the tubular volume fraction (39,40). Therefore, a three-compartment model of the kidney was used, implementing

a tri-exponential decay function with defined parameters according to the following equation:

$$SI = f_{tissue}e^{-b\,D_{tissue}} + f_{tubules}e^{-b\,D_{tubules}} + f_{blood}e^{-b\,D_{blood}} \qquad [1]$$

where SI is the normalized signal intensity as a function of b (b-value), f_{tissue} the signal fraction of the tissue component, D_{tissue} the diffusion coefficient of restricted water diffusion in renal tissue, $f_{tubules}$ the signal fraction of the tubular component, $D_{tubules}$ the pseudo-diffusion coefficient of the tubular fluid component, f_{blood} the signal fraction of the blood component, and D_{blood} the pseudo-diffusion coefficient of the blood component.

Since the number of compartments might change in pathophysiological conditions of the kidney including the development of fibrosis, a fourth compartment was applied.

$$SI = f_{fibrosis}e^{-b\,D_{fibrosis}} + f_{tissue}e^{-b\,D_{tissue}} + f_{tubules}e^{-b\,D_{tubules}} + f_{blood}e^{-b\,D_{blood}} \qquad [2]$$

where $f_{fibrosis}$ is the signal fraction of the fibrotic component, $D_{fibrosis}$ the diffusion coefficient of restricted water diffusion in fibrotic tissue.

The sum of the fractions equals 1 in all multi-compartment models used.

NNLS continuum modelling

A multi-exponential analysis based on the NNLS algorithm of Lawson and Hanson (53) was used. The NNLS MATLAB (The Mathworks Inc., Natick, USA) implementation was adapted from the open-source software AnalyzeNNLS from Bjarnason and Mitchell (43).

The diffusion signal decay y_i can be expressed as a sum of exponential functions:

$$y_i = \sum_{j=1}^{M} s_j e^{-b_i D_j}, i = 1, 2, \cdots, N \qquad [3]$$

where s_j is the relative amplitude for each partitioned D-value D_j, b_i is the b-value that governs the diffusion sensitization for each data point in the signal decay, M is the number of logarithmically spaced D values (300 values were used), and N represents the total number of data points.

The NNLS algorithm is used to minimize:

$$\chi_r^2 = \min\left[\sum_{i=1}^{N} \left| \sum_{j=1}^{M} s_j e^{-b_i D_j} - y_i \right|^2 + \mu \sum_{j=2}^{M-1} \left| s_{j+1} - 2s_j + s_{j-1} \right|^2 \right] \qquad [4]$$

Eq. [4] includes a regularization term with a weighting

factor μ, found using generalized cross validation (54). The regularization term acts as a smoothing constraint that minimizes the curvature of the NNLS spectrum to provide a robust fit in the presence of noise. Another equally valid regularization paradigm used in the literature is L1-norm or sparsity regularization. The curvature regularization approach was chosen because of its analytic solvability, its justifiable assumption on the resulting spectrum and its successful use in the literature (32,45-52).

The output of NNLS is a diffusion coefficient distribution with distinct log-normal-like peaks. Each peak corresponds to a major (pseudo-)diffusion compartment. These peaks can be characterized by (I) area under the spectral curve fraction on the predefined logarithmic scale, and (II) geometric mean D coefficient. The number of peaks was not constrained *a priori*.

Numerical simulations

All numerical simulations were implemented in MATLAB using the open-source tool AnalyzeNNLS (43). The ground truth signal was created assuming a three-compartment or a four-compartment model {Eq. [1] and Eq. [2]} using three sets of parameters:

❖ The first parameter set was used to represent baseline conditions;
❖ The second parameter set was used to represent pathophysiological conditions of increased tubular volume fraction (ITV) ($f_{tubules}$);
❖ The third parameter set was used to represent pathophysiological conditions of two degrees of renal fibrosis ($f_{fibrosis}$).

Figure 1 describes the workflow from simulation of these parameters to visualization and mean absolute percentage error (MAPE) assessment. All parameters used for (I) baseline, (II) increased $f_{tubules}$ and (III) fibrosis (55-57) conditions are presented in *Table 1*. These parameters were obtained from the literature (39) and provide a fair approximation. The volume fractions $f_{fibrosis}$ of 10% and 30% represent grade I (mild) and a low grade II (moderate) of renal fibrosis, respectively, according to grading schemes used in human patients (grade I <25%, grade II >25–50% area) (56). Effects of experimental parameters such as the echo time and the diffusion time were not considered explicitly, but rather implicitly through varying SNR and the b-value range.

For each b-value, Rician noise was added to the signal. The signal SI was then fitted using the NNLS implementation and the common non-linear least squares (LS) fitting routine using a trust region growing algorithm [*fastnnls* routine, N-way toolbox for MATLAB (58)]. This procedure was repeated n=500 times for each (patho) physiological condition (baseline, increased $f_{tubules}$, two fibrotic conditions). Five hundred repetitions lead to error estimates with an uncertainty below 5% of the error magnitude. By using the same 500 realizations of noise for all cases we were able to reduce the impact of random fluctuation on our comparisons even further resulting in robust and interpretable results.

Non-linear least square fitting

The created tri-exponential function was also fitted with the common LS method using a trust region growing algorithm. For this purpose, starting values and parameter ranges were established (40) as summarized in *Table 2* with the starting values for each fraction being balanced between the conditions at baseline and ITV.

SNR

Diffusion decays were simulated at different SNR conditions to explore the impact of the noise for the NNLS and LS approach. For this purpose, Rician noise was added to the synthetic multi-exponential signal decay. SNR was defined as the signal intensity of the first b-value (b=0 s/mm^2), divided by the standard deviation of the noise added. The first b-value was used as an SNR reference, since acquiring b=0 s/mm^2 scans is standard procedure in DWI studies and therefore facilitates comparisons with other studies (30). In order to keep the comparison between different SNR-levels and simulated scenarios free from statistical fluctuations, the same set of noise realizations (n=500) was used for all SNR-levels and scenarios. An SNR range from 40 to 1,000 (SNR =40, 80, 120, 160, 200, 280, 360, 440, 520, 640, 760, 880, 1,000) was chosen to cover the SNR of typical raw images as well as the SNR derived from restoration of DWI data using noise filtering (59-61). The SNR range also covers SNRs obtained from averaging over regions of interest (ROI) where the averaged SNR_{ROI} is proportional to the square root of the number of the pixels included.

Diffusion sensitization

To study the impact of the number of b-values, this parameter was varied from 10 to 50 b-values in increments
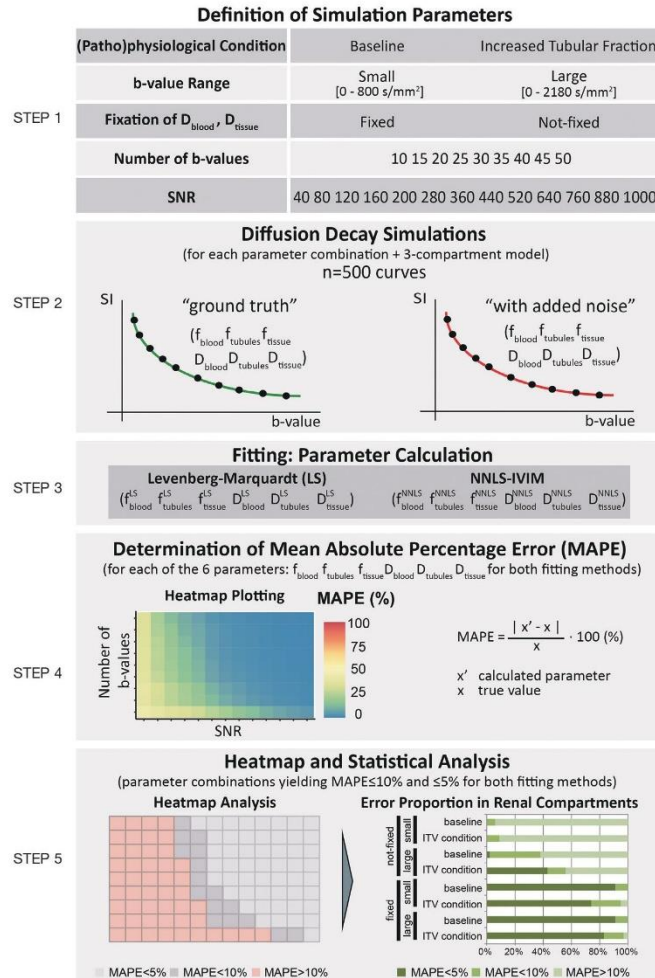
Figure 1 Workflow used for LS and NNLS computation for DWI of the kidney tubule. Numerical simulations were performed and analysed using NNLS continuum modelling. For the ground truth a tri-exponential function using defined volume fractions and diffusion coefficients for each renal compartment were applied. For NNLS and LS computations (patho)physiological conditions (baseline and ITV), range of b-values (from small b-value range: b=0–800 s/mm² to large value range: b=0–2,180 s/mm²) and parameter fixation (D_{blood} and D_{tissue} fixed vs. D_{blood} and D_{tissue} not-fixed) were applied. MAPE was calculated (average n=500) using the ground truth as a reference. The results were displayed using a MAPE heat map showing the difference between the ground truth and the data obtained from NNLS or LS for each condition. From the MAPE heat map the percentage of combinations (SNR/number of b-values) with a difference between the ground truth and the NNLS data or the LS data of less than 5% or less than 10% were quantified and plotted in an error proportion plot. LS, least squares; NNLS, non-negative least squares; DWI, diffusion-weighted MRI; MAPE, mean absolute percentage error; SNR, signal-to-noise ratio; f_{blood}, volume fraction of blood; $f_{tubules}$, volume fraction of tubules; f_{tissue}, volume fraction of tissue; $f_{fibrosis}$, volume fraction of fibrosis; D_{blood}, diffusion coefficient of blood; $D_{tubules}$, diffusion coefficient of tubules; D_{tissue}, diffusion coefficient of tissue; $D_{fibrosis}$, diffusion coefficient of fibrosis; b-value, diffusion weighting.

Table 1 Summary of multi-exponential parameters used for the generation of the synthetic diffusion decay data

Parameters	Baseline (39)	Increase of tubular volume fraction	Fibrotic conditions 10%	Fibrotic conditions 30%
Fraction blood (f_{blood})	0.10	0.05	0.10	0.10
Fraction tubules ($f_{tubules}$)	0.30	0.50	0.30	0.30
Fraction tissue (f_{tissue})	0.60	0.45	0.50	0.30
Fraction fibrotic tissue ($f_{fibrosis}$)	0.00	0.00	0.10 (56)	0.30 (56)
Diffusion blood (D_{blood})	180.0×10^{-3} mm^2/s			
Diffusion tubules ($D_{tubules}$)	5.80×10^{-3} mm^2/s			
Diffusion tissue (D_{tissue})	1.50×10^{-3} mm^2/s			
Diffusion fibrotic tissue ($D_{fibrosis}$)	8×10^{-5} mm^2/s (55,57)			

f_{blood}, volume fraction of blood; $f_{tubules}$, volume fraction of tubules; f_{tissue}, volume fraction of tissue; $f_{fibrosis}$, volume fraction of fibrosis; D_{blood}, diffusion coefficient of blood; $D_{tubules}$, diffusion coefficient of tubules; D_{tissue}, diffusion coefficient of tissue; $D_{fibrosis}$, diffusion coefficient of fibrosis.

Table 2 Summary of LS fitting parameters

| Compartment	Fraction (f)		Diffusion (D)	
	Starting values	Range	Starting values (mm^2/s) (40)	Range (mm^2/s) (40)
Blood	(f_{blood}) 0.075	[0.001; 0.999]	(D_{blood}) 551×10^{-3}	$[9; 1,000] \times 10^{-3}$
Tubules	($f_{tubules}$) 0.400	[0.001; 0.999]	($D_{tubules}$) 9.7×10^{-3}	$[2; 50] \times 10^{-3}$
Tissue	(f_{tissue}) 0.525	[0.001; 0.999]	(D_{tissue}) 1.9×10^{-3}	$[0.01; 7] \times 10^{-3}$

LS, least squares; f_{blood}, volume fraction of blood; $f_{tubules}$, volume fraction of tubules; f_{tissue}, volume fraction of tissue; D_{blood}, diffusion coefficient of blood; $D_{tubules}$, diffusion coefficient of tubules; D_{tissue}, diffusion coefficient of tissue.

of 5. We hypothesized that a larger number of b-values would result in a lower error for both fitting methods. However, increasing the number of b-values prolongs examination times and imaging protocols, which is not always feasible for *in vivo* experiments.

To investigate the impact of the range of b-values, 10 sets of diffusion sensitization ranges were examined. For the first set, a b-value range of b=0 to 800 s/mm^2 (small b-value range) was obtained from consensus-based technical recommendations for clinical translation of renal DWI (30). *Figure 2A* describes the decomposition of the 1st derivative of the diffusion decay together with the 1st derivative of the decay of individual components of a tri-exponential model including intrarenal blood, tubules and renal tissue. For the tubule system the full width half maximum (FWHM) of the 1st derivative encompasses a b-value range of b=40 to 460 s/mm^2. The 1st derivative of the tissue signal component is dominant for b≥250 s/mm^2. For quantification of D_{tissue} and f_{tissue} sampling of this b-range is important to obtain SI(b) and the

1st derivative of SI(b). However, if D_{tissue} is known *a priori* the focus remains on b≤800 s/mm^2 where most of the tubular signal component is decayed. For comparison diffusion sensitization was extended to b=0–1,110 s/mm^2 (10 b-values), b=0–1,380 s/mm^2 (15 b-values, designated as medium b-value range), b=0–1,570 s/mm^2 (20 b-values), b=0–1,710 s/mm^2 (25 b-values), b=0–1,840 s/mm^2 (30 b-values), b=0–1,940 (35 b-values), b=0–2,030 s/mm^2 (40 b-values), b=0–2,110 s/mm^2 (45 b-values) and b=0–2,180 s/mm^2 (50 b-values, designated as large b-value range). For each b-value range the largest b-value was set so that the expected relative signal intensity is equal to (1/number b-values) for the largest b-value (*Figure 2B*). In order to create an unbiased b-scale that does not favor any one component at the expense of any other, each b-value was distributed over the b-value range to yield a constant signal intensity decrement (1/number of b-values) from one b-value to another as outlined in *Figure 2B*, assuming the ground truth values outlined in *Table 1*. Maintaining the signal intensity decay constant
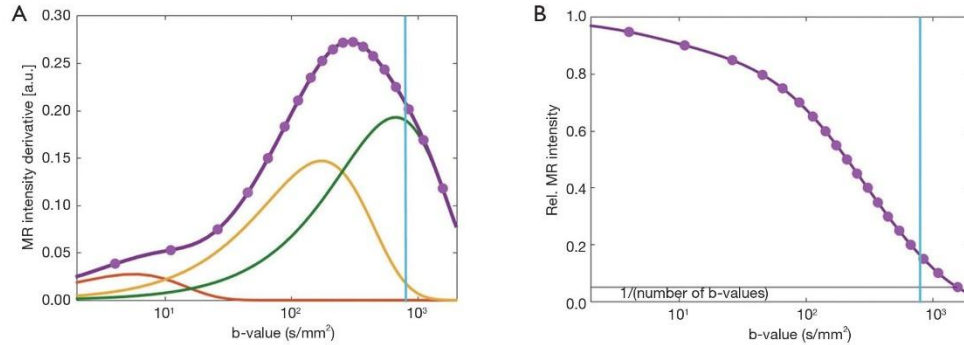
Figure 2 Diffusion sensitization considerations. (A) The 1st derivative of the diffusion decay (purple) together with the 1st derivative of the individual components of a tri-exponential model: blood (red), tubules (orange) and tissue (green). For the tubules system the FWHM of the 1st derivative encompasses a b-value range of b=40–460 s/mm^2. The cyan line marks b=800 s/mm^2. (B) Diffusion decay using a logarithmic scale. The number of b-values (n=20) was set so that the relative signal intensity is equal to (1/number of b-values) for the largest b-value. This approach yields a constant signal intensity decrement (1/number of b-values) from one b-value to the next, to ensure that individual measurements are independent of the signal decay. FWHM, full width half maximum; b-value, diffusion weighting.

from one b-value to the next ensures independence of the individual measurements of the signal decay, and is therefore a reasonable approach for quantification of the individual exponential contributions. The equidistant intensity drop from one b-value to the next was computed by interpolating on a fine evaluation of the tri-exponential decay with exponential weights in between the baseline and the increased tubular fraction case (f_{blood} =0.075; $f_{tubules}$ =0.4; f_{tissue} =0.525).

Under physiological conditions and upon changes in the tubular volume fraction, the physicochemical properties of renal tissue and intrarenal blood are recognized to be essentially invariable (62). It is therefore reasonable to study the effect of fixing the diffusion coefficients D_{tissue} and D_{blood} for these compartments. Fixing fitting parameters to improve the robustness of the fit is common practice (40), especially when dealing with multi-exponential functions, where at least six parameters are needed. We tested the effect of fixing diffusion coefficients on NNLS continuum modelling by setting the diffusion parameter to a predefined value for the slowest and fastest components. A similar simplification was applied for the NNLS continuum modelling by restricting the diffusion-coefficient-basis to the range of the intermediate component between 3×10^{-3} and 33×10^{-3} mm^2/s, and two single exponentials with known diffusion coefficients for the fast and slow components. The two fixed NNLS-basis-vectors were excluded from

curvature regularization. Areas under the continuous diffusion spectrum were determined using the MATLAB function SUM between two adjacent minima in the spectra. Relative areas were obtained by dividing each peak by the total area obtained for all peaks.

MATLAB Code Availability Statement: The MATLAB code will be made openly available in GitHub at https://github.com/JoaoPeriquito/NNLS_computation_of_renal_DWI.

Statistics

For the simulations the MAPE was used to show the percentage difference between the calculated value and the true value, for the 9×13 matrix of b-values and SNR values (*Figure 1*). MAPE is defined as:

$$MAPE = \frac{|x'-x|}{x} \cdot 100 \qquad [5]$$

where x' is the calculated parameter and x the true-value. The Shapiro-Wilk test was used to assess for Gaussian distribution. MAPE values did not conform to a Gaussian distribution, thus non-parametric statistical tests were used including the paired Wilcoxon signed-rank test, the Kruskal-Wallis test and Dunn's *post-hoc* procedure. Differences in MAPE obtained for fixing *vs.* not-fixing the D_{blood} and D_{tissue} diffusion parameters, for the b-value ranges used (b$_{range\_small}$ =0–800 mm^2/s up to b$_{range\_large}$ =0–2,180 mm^2/s),
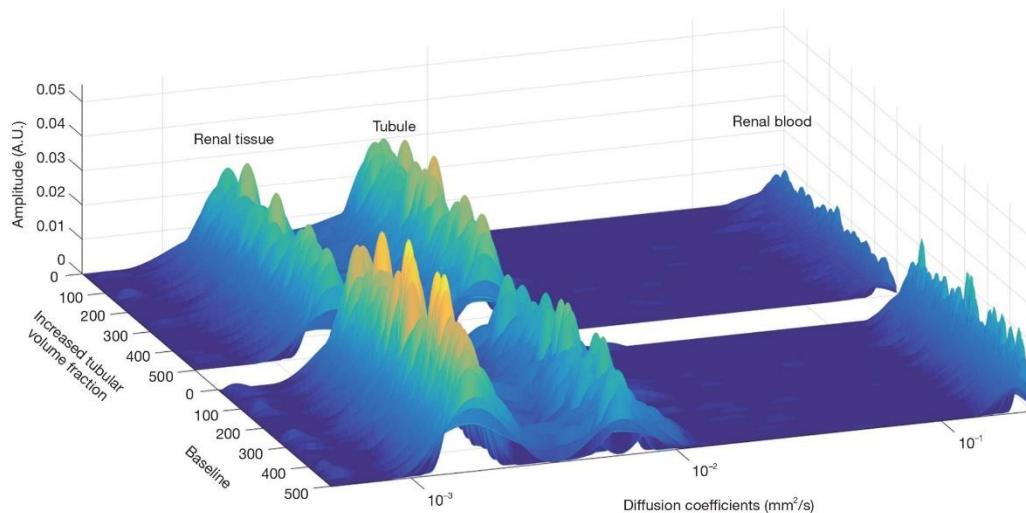
Figure 3 Example of an NNLS spectrum for baseline and for the (patho)physiological condition of an ITV. The spectra were obtained for a signal intensity decay covering 25 b-values using a SNR =360 for b=0 s/mm². The three peaks along the diffusion coefficient direction represent three diffusion decay components: a slow-decay component for renal tissue (left peak), an intermediate-decay component for tubules (middle peak) and a fast-decay component for intrarenal blood (right peak). The (patho)physiological condition of ITV decreased the areas under the left and right peaks and increased the area under the middle peak. NNLS, non-negative least squares; ITV, increased tubular volume fraction; SNR, signal-to-noise ratio; b-value, diffusion weighting.

and for the physiological state (baseline *vs.* ITV) were tested independently using the paired Wilcoxon signed-rank test. Differences in MAPE among the 2^3 permutations of the independent variables volume fraction, b-value and fixation state—with each variable having two levels—were assessed with the Kruskal-Wallis non-parametric ANOVA test. To determine which specific pair-wise comparisons were different, Dunn's *post-hoc* test was performed for selected pairwise comparisons with Holm's correction for multiple comparisons. The accuracy to discriminate between baseline and the pathophysiological conditions of an ITV or renal fibrosis was evaluated using signal intensity-based receiver-operating characteristic (ROC) curves. The area under the curve (AUC) was calculated and compared with DeLong's test (63), using the R packages pROC (64), plotROC (65) and cutpointr (66). The Kruskal-Wallis test was used to compare the AUC of the fibrotic compartment between the simulated conditions of 30%, 10% and no fibrosis. Data analysis was done using the statistical computing environment R (v.3.3.4) (https://www.R-project.org).

Results

NNLS continuum modelling

Analysis of the simulated data with the NNLS continuum modelling resulted in a distribution of diffusion coefficients covering the full range expected for the three components. *Figure 3* demonstrates that it is possible to ascribe each of the three peaks along the diffusion coefficient spectrum to a diffusion decay component. The left peak can be attributed to the slow-decay component of tissue (D_{tissue}: ~1.50×10^{-3} mm²/s), the middle peak to the intermediate-decay component from tubules (D_{tubule}: ~5.80×10^{-3} mm²/s) and the right peak to the fast-decaying component associated with blood (D_{blood}: ~180.00×10^{-3} mm²/s). The graph shows 1,000 NNLS spectra produced from simulations of baseline conditions (n=500) and of ITV conditions (n=500). The change of the intensity ratio of the two slower component peaks is clearly visible when transitioning from baseline conditions to ITV conditions. Similar datasets were acquired for all combinations of SNR, b-value number and b-value

3106

Periquito et al. Diffusion spectrum computation for DWI-MRI of kidney tubules
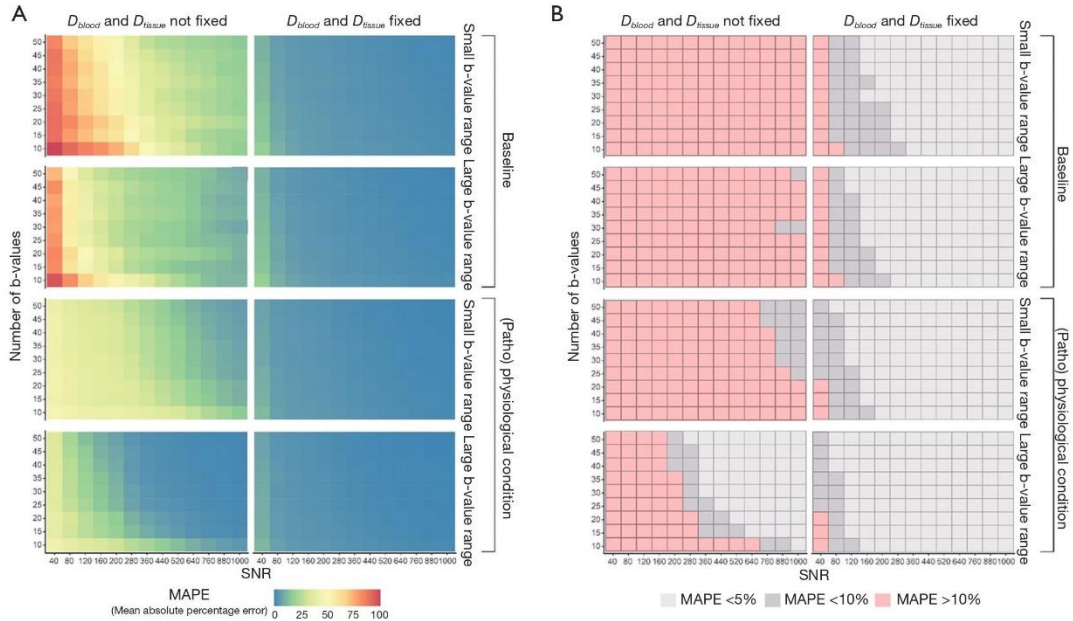
Figure 4 MAPE heat maps for tubular volume fraction for all simulations. (A) MAPE heat maps related to the tubular fraction for all continuum modelling NNLS simulations. Left column: no fixation of D_{blood} and D_{tissue}, right column: fixation of D_{blood} and D_{tissue}. (B) Highlight of the MAPE heat maps related to the tubular fraction for all NNLS continuum modelling simulations with MAPE <5%, <10% and >10%. Left column: no fixation of D_{blood} and D_{tissue}, right column: fixation of D_{blood} and D_{tissue}. MAPE, mean absolute percentage error; NNLS, non-negative least squares; SNR, signal-to-noise ratio; D_{blood}, diffusion coefficient of blood; D_{tissue}, diffusion coefficient of tissue; b-value, diffusion weighting.

range. To process this large amount of data, peak areas and geometric mean positions were first extracted from the spectra and then compared to the ground truth by using the MAPE.

MAPE of tubular volume fraction, blood and renal tissue

MAPE was used as a metric to assess which combination of SNR/number of b-values provides less than 5% or 10% error from the true value. *Figure 4A* shows heat maps of the individual MAPE of the tubular volume fraction. As expected, the error decreases with increasing SNR. Increasing the number of b-values is also beneficial for tubular volume fraction quantification. Correspondingly, using 10 b-values at SNR =80 provides similar MAPE as using 40 b-values at SNR =40 (*Figure 4A*). Furthermore, the benefit of additional b-values diminishes with each

subsequent addition. From 25 b-values onwards, the benefit becomes less apparent. A pronounced increase in the precision is also discernible when the range of b-values is increased (small range, b=0–800 s/mm² *vs.* large range, b=0–2,180 s/mm²). In all cases MAPE is substantially improved when reducing the number of determined parameters from 6 to 4 by fixing the (pseudo-)diffusion coefficients of blood and tissue.

Figure 4B highlights the combinations of SNR/number of b-values that provide a MAPE below 5% (light gray) or 10% (dark gray) for the tubular volume fraction. The percentage of these successful combinations was extracted from each of the MAPE heat maps as the quantitative description of the method's precision for further consideration. The number of combinations with an error below 10% with no fixation used was 0% for baseline-small b-value range, 3% for baseline-large b-value range, 10%

for increased tubular fraction-small b-value range, and 58% for increased tubular fraction-large b-value range. In non-fixed cases, an error below 5% was only found for increased tubular fraction-large b-value range (44% of combinations). The fraction of combinations below 10% error when fixation of D_{blood} and D_{tissue} was used was 91% for baseline and 97% for increased tubular fraction (for both small and large range). An error below 5% was observed in 68% of baseline-small b-value range, 75% of baseline-large b-value range, 81% of ITV-small b-value range, and 86% of ITV-large b-value range combinations.

Figure 5 shows the percentages of excellent (MAPE <5%), good (MAPE <10%) and unsuitable (MAPE >10%) simulation results for each of the eight combination of parameters for the renal blood, tubules and tissue compartments. Here we compare LS with NNLS continuum modelling with respect to different MAPE stratifications for each simulated permutation. By fixing the value of blood diffusion coefficient D_{blood} and tissue diffusion coefficient D_{tissue}, more than 60% of all combinations yielded an error below 10% for all parameters and more than 40% provided an error below 5% for all parameters using NNLS continuum modelling. For LS the use of fixation yielded for more than 70% of all combinations an error below 10% for all parameters. More than 50% of the combinations showed an error below 5% for all parameters.

In addition to improving the proportion of combinations with good and excellent error levels, fixing the blood (D_{blood}) and tissue diffusion (D_{tissue}) coefficients significantly reduced the absolute value of the MAPE of the tubular volume fraction (P=2.13×10^{-78} fixed *vs.* not-fixed, Wilcoxon signed-rank test). Similarly, using a large range of b-values significantly reduced the MAPE in the tubular volume fraction (P=2.78×10^{-77} smallest *vs.* largest b-value range, Wilcoxon signed-rank test).
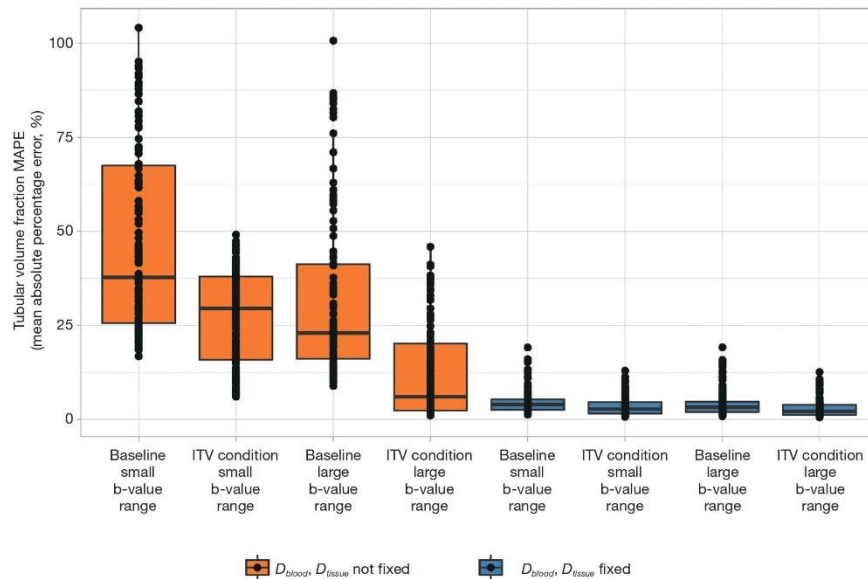
Pathophysiological condition of ITV

For the first pathophysiological condition, we studied the impact of an increase in the tubular volume fraction. This condition does not alter the number of compartments. Increasing tubular volume fraction significantly reduced the MAPE in this compartment, compared to baseline (P=2.15×10^{-78}, Wilcoxon signed-rank test). When considering differences among all permutations of the three simulation conditions (i.e., baseline *vs.* ITV, smallest *vs.* largest b-value range, fixation of D_{blood} and D_{tissue} *vs.* no

fixation—three conditions with two levels each, 2^3=8), the error values differed significantly (Kruskal-Wallis statistic =621.1, eta^2 effect size =0.662, which was independent of the number of simulations, P=7.07×10^{-130}) (*Figure 6*). Pairwise *post-hoc* comparisons corrected for selected multiple comparisons are shown in *Table 3*.

We then proceeded to evaluate the accuracy to discriminate between baseline and increased tubular volume conditions based on the signal intensity. When diffusion coefficients were not fixed, and the b-value range was kept constant at a small value (b=0–800 s/mm^2) increasing the number of b-values significantly improved discrimination accuracy, with the AUC increasing from 0.63 to 0.74 (10 *vs.* 50 b-values, P<2.2×10^{-16}, DeLong's test, *Figure 7A*). The optimal cut-off values, sensitivity and specificity for all ROC curves are listed in *Table 4*. Increasing to a larger range of b-values had a greater impact on discrimination accuracy. Maintaining 10 b-values while increasing the range to b=0–1,100 s/mm^2 improved the AUC to 0.83. Using a medium b-value range of b=0–1,380 s/mm^2 (with 15 b-values) improved the AUC to >0.90, and further increases beyond this range yielded diminishing improvements, although these were statistically significant (AUC =0.91 *vs.* 0.96, medium b-value range 0–1,380 *vs.* maximum b-value range 0–2,180 s/mm^2, P<2.2×10^{-16}, DeLong's test, *Figure 7B*, *Table 4*). Based on our empirical testing illustrated in *Figure 7A,B* and *Figure 4A*, we conclude that a minimum number of 10 b-values is right at the limit of yielding an appropriate description of the tri-exponential decay. When D_{blood} and D_{tissue} were not fixed, SNR had a more profound impact on discrimination accuracy. At SNR =40, the discrimination between baseline and ITV was rather poor, with an AUC of 0.66 for the ROC curve. This performance increased steadily with increasing SNR, achieving a maximum discrimination accuracy of 0.94 at a maximum SNR of 1,000. However, the magnitude of this improvement diminished at higher SNR values. While the increase in discrimination accuracy from SNR 880 to SNR 1,000 was significant, the improvement was nevertheless marginal (AUC =0.93 *vs.* 0.94, P=1.1×10^{-5}, DeLong's test, *Figure 7C*, *Table 4*). Fixing the diffusion coefficients for blood and renal tissue had a profound effect on discrimination accuracy. Considering all numbers of b-values, b-value ranges and SNR levels, the AUC was 0.83. When D_{blood} and D_{tissue} were fixed, the discrimination accuracy was near perfect, with AUC of 0.99 (not fixed *vs.* fixed, P<2.2×10^{-16}, DeLong's test, *Figure 7D*, *Table 4*).
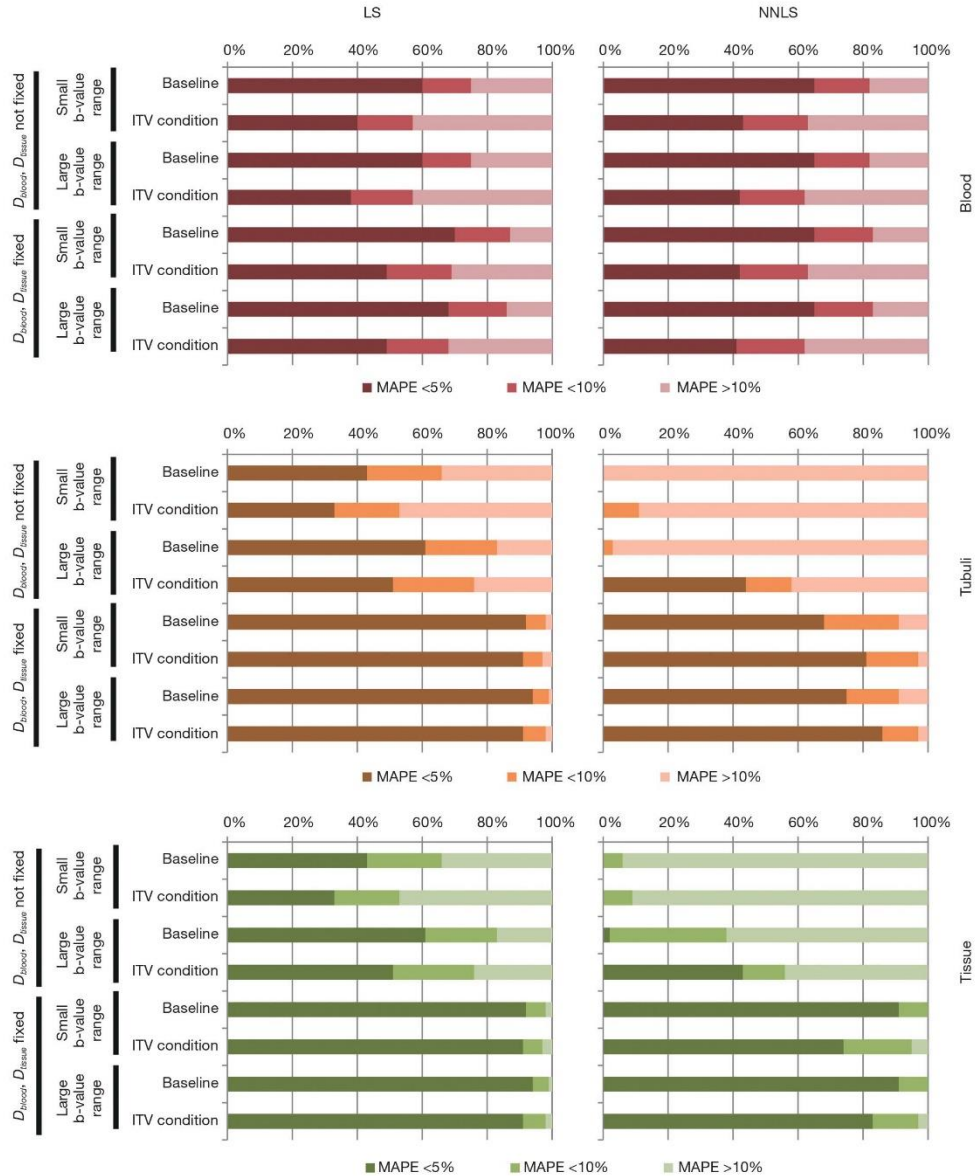
Figure 5 Survey of the results obtained from error analysis. The error proportion plots show the percentage of combinations with the MAPE below 5% or below 10% using non-linear LS fitting (left column) and NNLS continuum modelling (right column) for all kidney fractions: intrarenal blood, tubule and renal tissue. MAPE, mean absolute percentage error; LS, least squares; NNLS, non-negative least squares; ITV, increased tubular volume fraction; D_{blood}, diffusion coefficient of blood; D_{tissue}, diffusion coefficient of tissue; b-value, diffusion weighting.

Figure 6 Statistical comparison of the effects of (I) fixation of D_{blood} and D_{tissue} (not-fixed *vs.* fixed), (II) of the (patho)physiological condition (baseline *vs.* increased tubular volume) and (III) of the b-value range (small *vs.* large b-value range). MAPE analysis of the tubular volume fraction from NNLS continuum modelling was compared between all permutations of the simulation conditions: fixation of D_{blood} and D_{tissue} (fixed or not-fixed), (patho)physiological condition (baseline *vs.* increase in tubular volume) and range of b-values (small b-value range over large b-value range). Each of these three factors had significant effects on the error values when considered independently. Comparing among the permutations showed significant differences in MAPE (P=7.07×10^{-130}, Kruskal-Wallis non-parametric ANOVA, followed by Dunn's procedure with Holm's correction for multiple comparisons). Selected pairwise comparisons are summarized in *Table 3*. MAPE, mean absolute percentage error; NNLS, non-negative least squares; ITV, increased tubular volume fraction; D_{blood}, diffusion coefficient of blood; D_{tissue}, diffusion coefficient of tissue; b-value, diffusion weighting.

Pathophysiological condition of fibrosis

Next, we simulated pathophysiological conditions that mimic grade I (mild, 10%) and low grade II (moderate, 30%) interstitial renal fibrosis, thereby adding another component that may be considered as an additional renal compartment ($f_{fibrosis}$). Using data with the maximum b-value range of 0–2,180 s/mm^2 (50 b-values), NNLS continuum modelling was able to detect the diffusion component of the fibrotic compartment, to differentiate it from the other three diffusion components, and to distinguish 10% from 30% fibrosis (*Figure 8A*). Furthermore, this was also the case when the medium b-value range of 0–1,380 s/mm^2 (15 b-values) was used (*Figure 8B*). For both the large and the medium b-value ranges, the AUC (signal intensity) of the fibrotic

compartment was significantly greater under both the simulated conditions of grade I and grade II fibrosis (affecting 10% and 30% of the renal area, respectively) compared to the fibrosis-free condition. The signal intensities obtained for grade II were significantly higher than for grade I. This distinction improved with increasing SNR (*Figure 8A,B*, P<2.2×10^{-16}, Kruskal-Wallis non-parametric ANOVA, followed by Dunn's procedure with Holm's correction for multiple comparisons). Discrimination between either 30% or 10% fibrosis or non-fibrosis based on the signal intensity of the fibrotic compartment was near perfect. The ROC curves show AUC =0.98, 1.00 (medium b-value range), and 0.99, 0.99 (large b-value range), for 30% and 10% fibrosis, respectively (*Table 4*).

3110

Periquito et al. Diffusion spectrum computation for DWI-MRI of kidney tubules

Table 3 Pairwise post-hoc comparisons of the MAPE

Effect of	Fixation of D_{blood} and D_{tissue}	B-value range	(Patho)physiological condition[a]	Adjusted P value[b]	Significance
Fixation of D_{blood} and D_{tissue}	Not-fixed	Small	Baseline	$3.2×10^{-38}$	****
	Fixed				
	Not-fixed	Small	ITV condition[a]	$4.9×10^{-36}$	****
	Fixed				
	Not-fixed	Large	Baseline	$4.5×10^{-31}$	****
	Fixed				
	Not-fixed	Large	ITV condition	$1.4×10^{-9}$	****
	Fixed				
B-value range	Not-fixed	Small	Baseline	$5.8×10^{-2}$	NS
		Large			
	Not-fixed	Small	ITV condition	$3.7×10^{-13}$	****
		Large			
	Fixed	Small	Baseline	$7.3×10^{-1}$	NS
		Large			
	Fixed	Small	ITV condition	$7.3×10^{-1}$	NS
		Large			
(Patho)physio-logical condition	Not-fixed	Small	Baseline	$5.8×10^{-2}$	NS
			ITV condition		
	Not-fixed	Large	Baseline	$3.1×10^{-13}$	****
			ITV condition		
	Fixed	Small	Baseline	$1.3×10^{-1}$	NS
			ITV condition		
	Fixed	Large	Baseline	$1.3×10^{-1}$	NS
			ITV condition		

[a], ITV condition refers to an increase in the tubular volume fraction; [b], Dunn's post-hoc test with Holm correction for multiple comparisons; ****, P<0.00001. MAPE, mean absolute percentage error; D_{blood}, diffusion coefficient of blood; D_{tissue}, diffusion coefficient of tissue; b-value, diffusion weighting.

Discussion

This study is the first report on a systematic examination of NNLS computation for DWI of the kidney tubule system. Our results demonstrate the feasibility of NNLS continuum modelling for renal DWI as a less constrained, data-driven alternative for monitoring changes in the tubular volume fraction and the degree of tissue fibrosis. Our numerical simulations demonstrate the impact of SNR, the number of b-values needed for characterization of the diffusion signal decay and the range of diffusion sensitization on NNLS continuum modelling-based renal DWI applications. We show that while the error inherent to the NNLS continuum modelling is not superior to conventional fitting approaches using rigid multi-exponential models *per se*, it strongly depends on the specific parameter combinations applied during renal DWI. Our simulations present DWI-MRI parameters that ensure an error of less than 10% and 5%, respectively, for NNLS continuum modelling of the tubular

67
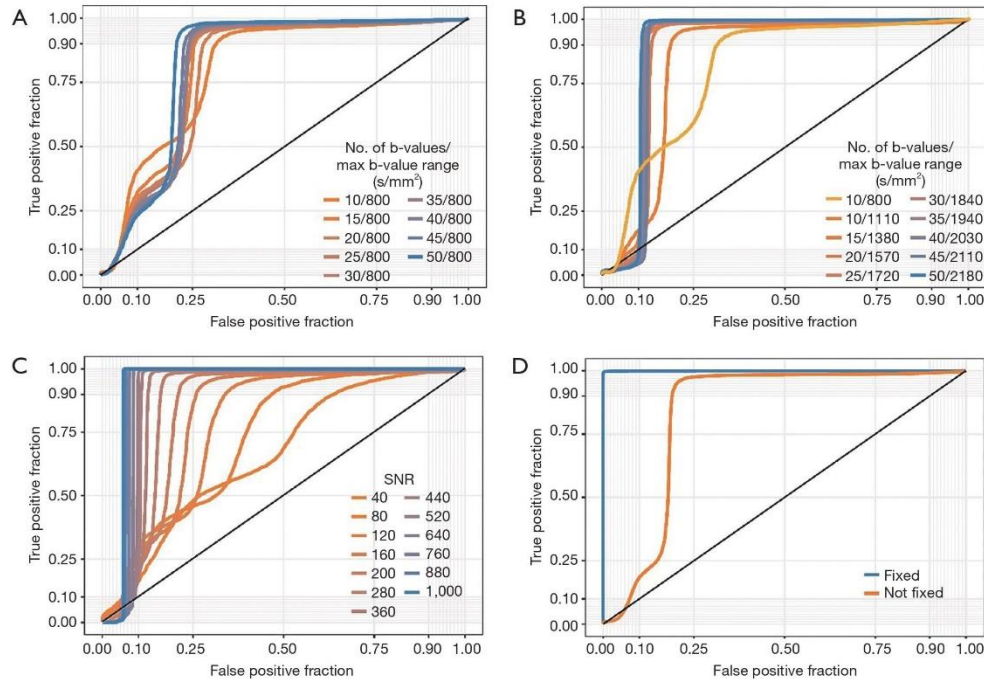
Figure 7 Effects of number of b-values, range of b-values, SNR and fixation of D_{blood} and D_{tissue} (fixed *vs.* not-fixed) on accuracy to discriminate baseline and ITV. ROC curves show the accuracy of discriminating between baseline renal tubular volume conditions and pathophysiological conditions that mimic an ITV, based on signal intensity. (A) When diffusion coefficients were not fixed, and the b-value range was kept constant at a small value (b=0–800 s/mm²) increasing the number of b-values significantly improved discrimination accuracy, with the AUC increasing from 0.63 to 0.74 (10 *vs.* 50 b-values, P<2.2×10⁻¹⁶, DeLong's test). (B) Increasing to a larger range of b-values had a greater impact on discrimination accuracy. Maintaining 10 b-values while increasing the range to b=0–1,100 s/mm² improved the AUC to 0.83. Using a medium b-value range of b=0–1,380 s/mm² improved the AUC to >0.90, and further increases beyond this range yielded diminishing improvements (AUC =0.91 *vs.* 0.96, maximum b-value range 1,380 *vs.* 2,180 s/mm², P<2.2×10⁻¹⁶, DeLong's test). (C) When D_{blood} and D_{tissue} were not fixed, SNR had a pronounced impact of discrimination accuracy: At low SNR of 40 the AUC was 0.664, increasing to 0.942 at the highest SNR of 1,000 (P<2.2×10⁻¹⁶, DeLong's test). (D) Fixing the diffusion coefficients for blood and renal tissue had a profound effect on discrimination accuracy. Considering all numbers of b-values, b-value ranges and SNR levels, the AUC was 0.83. When D_{blood} and D_{tissue} were fixed, the discrimination accuracy was near perfect, with AUC of 0.99 (not fixed *vs.* fixed, P<2.2×10⁻¹⁶, DeLong's test). All values for AUC, optimal cut-off, sensitivity and specificity are listed in *Table 4*. SNR, signal-to-noise ratio; ITV, increased tubular volume fraction; ROC, receiver-operating characteristic; AUC, area under the curve; b-value: diffusion weighting.

volume fraction when compared to the ground truth given by the tri-exponential model.

Most renal DWI studies report two compartments: pseudo-diffusion related to incoherent water motion in the microvasculature, and true diffusion attributed to restricted diffusion in the tissue. Analysis of DWI using this approach, along with tracking of pathological changes, requires *a priori* assumptions in conjunction with rigid bi-exponential models. The fitting routine forces the data to conform to a bi-exponential behavior, and consequently, linear segmentation is frequently performed based on a given b-value threshold, assuming a bi-exponential behavior. Alternatively, parameters used for data acquisition may be customized by designing the diffusion sensitization with a

Table 4 Summary of ROC curve comparisons

Condition type[a]	Condition value	Area under curve	Optimal cut-off[b]	Sensitivity	Specificity
Small b-value range[c] (number of b-values/ maximum b-value)	10/800[d]	0.63	0.33	0.40	0.84
	15/800	0.68	0.33	0.53	0.84
	20/800	0.70	0.34	0.54	0.86
	25/800	0.70	0.34	0.58	0.86
	30/800	0.71	0.34	0.58	0.87
	35/800	0.73	0.35	0.60	0.90
	40/800	0.72	0.33	0.62	0.86
	45/800	0.73	0.34	0.63	0.87
	50/800	0.74	0.34	0.65	0.88
Large b-value range[c] (number of b-values/ maximum b-value)	10/800[d]	0.63	0.33	0.40	0.84
	10/1,110	0.83	0.32	0.77	0.89
	15/1,380	0.91	0.34	0.88	0.93
	20/1,570	0.93	0.34	0.91	0.93
	25/1,710	0.94	0.34	0.92	0.94
	30/1,840	0.95	0.35	0.92	0.95
	35/1,940	0.96	0.36	0.94	0.96
	40/2,030	0.96	0.34	0.95	0.95
	45/2,110	0.96	0.35	0.95	0.96
	50/2,180	0.96	0.36	0.95	0.96
SNR[c]	40	0.66	0.34	0.88	0.38
	80	0.72	0.37	0.91	0.52
	120	0.78	0.40	0.92	0.64
	160	0.81	0.40	0.94	0.72
	200	0.84	0.41	0.96	0.77
	280	0.86	0.42	0.97	0.82
	360	0.88	0.42	0.99	0.86
	440	0.90	0.43	0.99	0.88
	520	0.90	0.43	0.99	0.90
	640	0.92	0.41	1.00	0.91
	760	0.93	0.40	1.00	0.92
	880	0.94	0.38	1.00	0.93
	1,000	0.94	0.38	1.00	0.94
D_{blood} and D_{tissue} not fixed	–	0.83	0.40	0.96	0.79
D_{blood} and D_{tissue} fixed	–	0.99	0.40	0.99	1.00
Fibrosis (%)[e]/maximum b-value range	10/2,180[d]	0.99	0.02	0.96	0.96
	30/2,180	0.99	0.08	1.00	0.94
	10/1,380	0.98	0.01	0.96	0.93
	30/1,380	1.00	0.11	1.00	1.00

[a], accuracy to discriminate baseline and ITV based on signal intensity; [b], optimum cut-off determined by maximize metric; [c], ROC curves calculated on data without parameter fixation; [d], mm/s²; [e] accuracy to discriminate fibrosis component *vs.* no fibrosis based on signal intensity. ROC, receiver-operating characteristic; D_{blood}, diffusion coefficient of blood; D_{tissue}, diffusion coefficient of tissue; b-value, diffusion weighting; SNR, signal-to-noise ratio; ITV, increased tubular volume fraction.
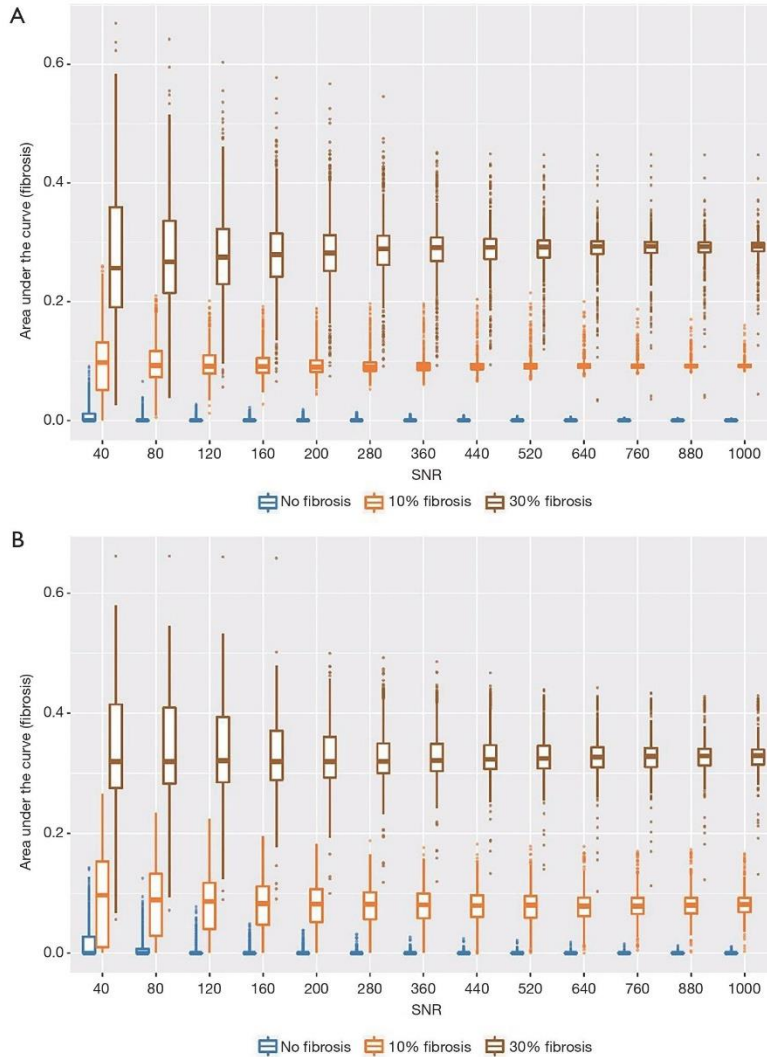
Figure 8 NNLS detection of simulated fibrosis component. The simulations included baseline (no fibrosis) and a pathophysiological condition to mimic fibrosis, thus adding a fourth renal compartment. (A) NNLS could readily detect this additional compartment, when using a large b-value range of 0–2,180 s/mm². (B) This result was also true when a medium b-value range of 0–1,380 s/mm² was used. For both the large and medium b-value ranges, the AUC (signal intensity) of the fibrotic compartment was significantly greater under both the simulated conditions of grade I (mild) and grade II (moderate) fibrosis (affecting 10% and 30% of the renal area, respectively) compared to the non-fibrosis condition. The signal intensities obtained for grade II were significantly higher than for grade I. This distinction improved with increasing SNR (P<2.2×10⁻¹⁶, Kruskal-Wallis non-parametric ANOVA, followed by Dunn's procedure with Holm's correction for multiple comparisons; whiskers denote ±1.5× interquartile range). NNLS, non-negative least squares; AUC, area under the curve; AUC, area under the curve; SNR, signal-to-noise ratio.

specific number and magnitude of b-values (32-38).

Recently it was shown that a three-compartment model is more appropriate for representation of the diffusion properties of the kidney assuming that incoherent renal water motion is linked to three sources: (I) tissue water diffusion, (II) incoherent blood motion, and (III) incoherent tubular fluid motion (39,40). The rigid bi-exponential and tri-exponential models share a common limitation: they may not accurately reflect the complex nature of renal water diffusion, because the data are forced to conform to simplified models. This limitation could introduce a bias that runs the risk of obscuring (patho)physiological changes inherent to incoherent water motion probed with renal DWI. NNLS continuum modelling does not suffer from this limitation. Because NNLS continuum modelling does not presume that only three compartments or sources are associated with renal incoherent water motion, it allows for the detection of additional sources such as lesions, tumors, or fibrosis. This advantage is particularly relevant for DWI-MRI of the kidney, as the number of compartments or sources cannot necessarily be known in advance, and might change during the progression, interception or therapeutic treatment of renal disease. An alternative framework for determining co-existing diffusion compartments without prior assumptions on their number has been recently demonstrated for DWI of the brain and is conceptually appealing for renal DWI (67).

Our data indicate that increasing the b-value range alone is not sufficient to ensure reliable measurements of the tubular volume fraction. However, even modest increases above the lowest b-value range of 0–800 s/mm^2 resulted in substantial improvements in discrimination accuracy. While we simulated a series of b-value ranges extending up to 0–2,180 s/mm^2, we observed that a medium b-value range of 0–1,380 s/mm^2 yielded the majority of the benefits, and that further increases in b-value range had diminishing returns. Using the large b-value range resulted in a clear distinction between mild and moderate fibrosis. Furthermore, the medium b-value range was also sufficient to discriminate between mild and moderate fibrosis with a high degree of accuracy. This medium b-value range is achievable on clinical grade MRI systems, where the progress in gradient coil technology has triggered the implementation of high performance whole body gradients offering $G_{max\,combined}$ =100 mT/m (68) or G_{max} =113 mT/m (69). In addition, the SNR had a pronounced effect. At low SNR, the accuracy to discriminate between baseline and ITV was poor but improved steadily with increasing SNR.

Our data suggest that a minimum number of 10 b-values is at the limit for reliable and robust diffusion coefficient fitting with NNLS under baseline conditions and with pathological changes. The use of 15 b-values significantly improved the fitting results and can be considered as an appropriate minimum number of b-values for reliable and robust diffusion coefficient fitting with NNLS. Increasing the number of b-values further would prolong the scan time, with diminishing benefits. Arguably, this extra scan time burden can be compensated by using acceleration techniques such as parallel imaging or compressed sensing approaches (70,71). Our simulations used an SNR range of 40–1,000 for b=0 s/mm^2 which meets the minimum SNR levels suggested for advanced renal DWI (30). Using the SNR obtained for higher b-values or for the largest b-value presents a viable alternative.

Beyond the effects of SNR and b-value numbers and ranges, we investigated the effects of fixing the blood diffusion coefficient D_{blood} and the tissue diffusion coefficient D_{tissue}. With this approach we obtained superior results, compared to the non-fixed value approach. Acceptable errors levels (<10%) were achieved in the majority of the combinations studied (>89%). Data superiority (errors levels <5%) was achieved in more than 60% of the SNR/number of b-values combinations, in both (patho) physiological conditions and when using small and large b-value ranges. The fixation of the two diffusion coefficients did not prevent the appearance of multiple peaks in the continuous region, where the curvature regularization was kept active. Fixing these coefficients led to near perfect sensitivity and specificity to discriminate between the baseline and increased tubular volume conditions based on signal intensity. The approach to fix the diffusion coefficients of blood and tissue is advisable in situations where one can presume that (patho)physiological conditions or interventions do not dramatically change the physicochemical properties of blood and tissue.

The common non-linear LS fitting method using the trust region growing algorithm is considered the gold standard for fitting the DWI decay. After fixing D_{blood} and D_{tissue}, NNLS continuum modelling showed a similar degree of reliability as the non-linear LS with some slight differences in the case of tubules and tissue. 89% of combinations had acceptable error levels <10%, and more than 50% of SNR/b-values had errors below 5% for all parameters, compared to 40% on NNLS continuum modelling. While both approaches showed a similar degree of error, rigid models like LS can introduce a bias in the

71

analysis, since the number of compartments (number of exponential decays), must be specified *a priori*. Furthermore, starting values are crucial, and each additional exponential (additional compartment) included in the model requires two additional variables. Multi-exponential models with too many variables suffer from poor fit stability (40). NNLS continuum modelling is less constrained than LS. NNLS can delineate the complex nature of water diffusion and possible (patho)physiological changes with far fewer *a priori* assumptions. NNLS continuum modelling yields a distribution of diffusion coefficients rather than a unique value, which has the potential to better reflect the complex characteristics of biological tissues. This potential is underscored by the demonstration that the NNLS approach could detect simulated renal fibrosis. By not constraining the number of renal compartments in advance, NNLS could detect a fourth fibrosis compartment when this was introduced. Moreover, NNLS proved capable to distinguish between simulated 10% *vs.* 30% fibrosis.

This work lays the foundation for preclinical studies aimed at further elucidating the pathophysiology of various kidney diseases, as well as studies that aim to establish MR markers for diagnostics of those disorders. Renal tissue hypoxia is generally regarded as an early pivotal element in the pathophysiology of AKI, the possible progression of AKI to chronic kidney disease (CKD), and diabetic nephropathy. In virtually all of these disorders, the tubular volume fraction is altered, either due to changes in glomerular filtration rate, the tubular outflow towards the renal pelvis and beyond, in the transmural pressure gradient, or in tubular fluid resorption (3,7,22,23,25).

Because changes in the tubular volume fraction likely change the blood volume fraction, they result in changes in renal T_2^* independent of changes in blood oxygenation. Indeed, the tubular volume fraction is a confounding factor influencing the relationship between renal T_2^* mapping, oxygen saturation of hemoglobin, and tissue oxygen tension (21,29). Hence, DWI-based assessments of changes in the tubular volume fraction are highly relevant for elucidating the mechanisms of renal pathophysiology. Concomitant DWI-based measurements of the tubular volume fraction will help to accurately determine the pathophysiological role of changes in renal oxygenation as assessed by renal T_2^*.

This work also provides potential insights for translational research into MR-based diagnostic tools, as changes in the tubular volume fraction are present in a multitude of kidney disorders. Such changes are prominent in AKI as induced by disturbed systemic hemodynamics, by intravascular administration of X-ray contrast media, and by obstructions of the urinary tract and diabetic nephropathy (3,7,22,23). CKD of most origins is marked by fibrosis in addition to reduced glomerular filtration, which contributes to a decrease in the tubular volume fraction (46). In addition to pathological changes in the tubular volume, our simulations revealed that NNLS continuum modelling for renal DWI may also be useful for detection and treatment monitoring of renal fibrosis, which is an important biomarker of CKD and a powerful predictor of renal outcome (26,28). These same considerations likely apply to pathologies such as kidney lesions, polycystic kidney disease, or tumors.

A relevant caveat of this study is that the effect of kurtosis at high b-values (b>1,000 s/mm²) was not considered. At high b-values, the probability distribution of the diffusion displacement deviates from a Gaussian distribution. This is considered to be a consequence of the restrictions on water molecule displacement imposed by microstructures (72). However, the main focus of this work was to assess the kidney tubule system, where the absence of organelles and cell boundaries that might hinder diffusion renders the kurtosis effect less relevant (73,74).

The use of deep learning neural networks could potentially achieve the same or even better accuracy in disentangling the different DWI decay components at low SNR regimes with a low number of b-values. Neural networks could be trained to extract the water diffusion-related components of the tubules from the DWI decay directly, without complex pre- and post-processing methods. However, neural networks depend heavily on having a large body of ground truth training data, covering the entire range of biological variability and potential pathophysiological conditions.

The present study relies on numerical simulations, as a prelude to the acquisition of *in vivo* data. In the interests of time, resources, and adherence to the 3Rs principles to minimize the use of experimental animals, we consider that such in silico studies are a necessary precursor before proceeding to *in vivo* experiments, and that the results of these simulations must be disseminated to the community. The insights gained from the current study regarding the appropriate selection of experimental parameters will enhance the robustness and reproducibility of subsequent *in vivo* studies, which are the logical next step for future investigations of renal diffusion properties.

3116

Periquito et al. Diffusion spectrum computation for DWI-MRI of kidney tubules

Conclusions

In conclusion, our results demonstrate the implications of using NNLS continuum modelling with specific DWI acquisition and data processing protocols to provide assessment of the kidney tubule volume fraction with less than 5% or 10% error, and to offer the potential to detect diffusion compartments associated with renal pathology.

Footnote

Conflicts of Interest: All authors have completed the ICMJE uniform disclosure form (available at http://dx.doi.org/10.21037/qims-20-1360). TN, AP, TG, ES, SW, KC report funding provided by the German Research Foundation [Gefoerdert durch die Deutsche Forschungsgemeinschaft (DFG), Projektnummer 394046635, SFB 1365, RENOPROTECTION. Funded by the Deutsche Forschungsgemeinschaft (DFG, German Research Foundation), Project number 394046635, SFB 1365, RENOPROTECTION]. The other authors have no conflicts of interest to declare.

Ethical Statement: Ethical approval and written informed consent are not applicable to this manuscript, because it does not include any human or animal data.

References

1. Hoste EAJ, Kellum JA, Selby NM, Zarbock A, Palevsky PM, Bagshaw SM, Goldstein SL, Cerda J, Chawla LS. Global epidemiology and outcomes of acute kidney injury. Nat Rev Nephrol 2018;14:607-25.
2. Selby NM, Taal MW. Long-term outcomes after AKI-a major unmet clinical need. Kidney Int 2019;95:21-3.
3. Zuk A, Bonventre JV. Recent advances in acute kidney injury and its consequences and impact on chronic kidney disease. Curr Opin Nephrol Hypertens 2019;28:397-405.
4. Glassock RJ, Warnock DG, Delanaye P. The global burden of chronic kidney disease: estimates, variability and pitfalls. Nat Rev Nephrol 2017;13:104-14.
5. Fortrie G, de Geus HRH, Betjes MGH. The aftermath of acute kidney injury: a narrative review of long-term mortality and renal function. Crit Care 2019;23:24.
6. Levin A, Tonelli M, Bonventre J, Coresh J, Donner JA, Fogo AB, et al. Global kidney health 2017 and beyond: a roadmap for closing gaps in care, research, and policy. Lancet 2017;390:1888-917.
7. Fähling M, Seeliger E, Patzak A, Persson PB. Understanding and preventing contrast-induced acute kidney injury. Nat Rev Nephrol 2017;13:169-80.
8. van Duijl TT, Ruhaak LR, de Fijter JW, Cobbaert CM. Kidney injury biomarkers in an academic hospital setting: where are we now? Clin Biochem Rev 2019;40:79-97.
9. Luft FC. Biomarkers and predicting acute kidney injury. Acta Physiol (Oxf) 2021;231:e13479.
10. Schrezenmeier EV, Barasch J, Budde K, Westhoff T, Schmidt-Ott KM. Biomarkers in acute kidney injury - pathophysiological basis and clinical performance. Acta Physiol (Oxf) 2017;219:554-72.
11. Molitoris BA. Urinary biomarkers: alone are they enough? J Am Soc Nephrol 2015;26:1485-8.
12. Simms R, Sourbron S. Recent findings on the clinical utility of renal magnetic resonance imaging biomarkers. Nephrol Dial Transplant 2020;35:915-9.
13. Pickkers P, Ostermann M, Joannidis M, Zarbock A, Hoste E, Bellomo R, Prowle J, Darmon M, Bonventre JV, Forni L, Bagshaw SM, Schetz M. The intensive care medicine agenda on acute kidney injury. Intensive Care Med 2017;43:1198-209.
14. Matejovic M, Ince C, Chawla LS, Blantz R, Molitoris BA, Rosner MH, Okusa MD, Kellum JA, Ronco C. Renal hemodynamics in AKI: in search of new treatment targets. J Am Soc Nephrol 2016;27:49-58.
15. Khwaja A. KDIGO clinical practice guidelines for acute

kidney injury. Nephron Clin Pract 2012;120:c179-84.

16. Grenier N, Merville P, Combe C. Radiologic imaging of the renal parenchyma structure and function. Nat Rev Nephrol 2016;12:348-59.

17. Zarjou A, Sanders PW, Mehta RL, Agarwal A. Enabling innovative translational research in acute kidney injury. Clin Transl Sci 2012;5:93-101.

18. Evans RG, O'Connor PM. Initiation and progression of chronic kidney disease: can we definitively test the chronic hypoxia hypothesis? Hypertension 2013;62:827-8.

19. Cantow K, Hummel L, Flemming B, Waiczies S, Niendorf T, Seeliger E. Imagine physiology without imaging. Acta Physiol (Oxf) 2020;230:e13549.

20. Niendorf T, Frydman L, Neeman M, Seeliger E. Google maps for tissues: Multiscale imaging of biological systems and disease. Acta Physiol (Oxf) 2020;228:e13392.

21. Niendorf T, Pohlmann A, Arakelyan K, Flemming B, Cantow K, Hentschel J, Grosenick D, Ladwig M, Reimann H, Klix S, Waiczies S, Seeliger E. How bold is blood oxygenation level-dependent (BOLD) magnetic resonance imaging of the kidney? Opportunities, challenges and future directions. Acta Physiol (Oxf) 2015;213:19-38.

22. Premaratne E, Verma S, Ekinci EI, Theverkalam G, Jerums G, MacIsaac RJ. The impact of hyperfiltration on the diabetic kidney. Diabetes Metab 2015;41:5-17.

23. Barasch J, Zager R, Bonventre JV. Acute kidney injury: a problem of definition. Lancet 2017;389:779-81.

24. Mengel M. Deconstructing interstitial fibrosis and tubular atrophy: a step toward precision medicine in renal transplantation. Kidney Int 2017;92:553-5.

25. He L, Wei Q, Liu J, Yi M, Liu Y, Liu H, Sun L, Peng Y, Liu F, Venkatachalam MA, Dong Z. AKI on CKD: heightened injury, suppressed repair, and the underlying mechanisms. Kidney Int 2017;92:1071-83.

26. Ferguson CM, Eirin A, Abumoawad A, Saad A, Jiang K, Hedayat AF, Misra S, Glockner J, Textor SC, Lerman LO. Renal fibrosis detected by diffusion-weighted magnetic resonance imaging remains unchanged despite treatment in subjects with renovascular disease. Sci Rep 2020;10:16300.

27. Zhao J, Wang ZJ, Liu M, Zhu J, Zhang X, Zhang T, Li S, Li Y. Assessment of renal fibrosis in chronic kidney disease using diffusion-weighted MRI. Clin Radiol 2014;69:1117-22.

28. Hysi E, Yuen DA. Imaging of renal fibrosis. Curr Opin Nephrol Hypertens 2020;29:599-607.

29. Pohlmann A, Arakelyan K, Hentschel J, Cantow K, Flemming B, Ladwig M, Waiczies S, Seeliger E, Niendorf

T. Detailing the relation between renal T2* and renal tissue pO2 using an integrated approach of parametric magnetic resonance imaging and invasive physiological measurements. Invest Radiol 2014;49:547-60.

30. Ljimani A, Caroli A, Laustsen C, Francis S, Mendichovszky IA, Bane O, et al. Consensus-based technical recommendations for clinical translation of renal diffusion-weighted MRI. MAGMA 2020;33:177-95.

31. Caroli A, Schneider M, Friedli I, Ljimani A, De Seigneux S, Boor P, Gullapudi L, Kazmi I, Mendichovszky IA, Notohamiprodjo M, Selby NM, Thoeny HC, Grenier N, Vallee JP. Diffusion-weighted magnetic resonance imaging to assess diffuse renal pathology: a systematic review and statement paper. Nephrol Dial Transplant 2018;33:ii29-40.

32. Wurnig MC, Germann M, Boss A. Is there evidence for more than two diffusion components in abdominal organs? - A magnetic resonance imaging study in healthy volunteers. NMR Biomed 2018. doi: 10.1002/nbm.3852.

33. Fan M, Xing Z, Du Y, Pan L, Sun Y, He X. Quantitative assessment of renal allograft pathologic changes: comparisons of mono-exponential and bi-exponential models using diffusion-weighted imaging. Quant Imaging Med Surg 2020;10:1286-97.

34. Sułkowska K, Palczewski P, Furmańczyk-Zawiska A, Perkowska-Ptasińska A, Wójcik D, Szeszkowski W, Durlik M, Gołębiowski M, Małkowski P. Diffusion weighted magnetic resonance imaging in the assessment of renal function and parenchymal changes in chronic kidney disease: a preliminary study. Ann Transplant 2020;25:e920232.

35. Kuai ZX, Liu WY, Zhu YM. Effect of multiple perfusion components on pseudo-diffusion coefficient in intravoxel incoherent motion imaging. Phys Med Biol 2017;62:8197-209.

36. Schneider MJ, Dietrich O, Ingrisch M, Helck A, Winter KS, Reiser MF, Staehler M, Casuscelli J, Notohamiprodjo M. Intravoxel incoherent motion magnetic resonance imaging in partially nephrectomized kidneys. Invest Radiol 2016;51:323-30.

37. Barbieri S, Donati OF, Froehlich JM, Thoeny HC. Impact of the calculation algorithm on biexponential fitting of diffusion-weighted MRI in upper abdominal organs. Magn Reson Med 2016;75:2175-84.

38. Le Bihan D, Breton E, Lallemand D, Aubin ML, Vignaud J, Laval-Jeantet M. Separation of diffusion and perfusion in intravoxel incoherent motion MR imaging. Radiology 1988;168:497-505.

39. van Baalen S, Leemans A, Dik P, Lilien MR, Ten Haken B,

Froeling M. Intravoxel incoherent motion modeling in the kidneys: comparison of mono-, bi-, and triexponential fit. J Magn Reson Imaging 2017;46:228-39.

40. van der Bel R, Gurney-Champion OJ, Froeling M, Stroes ESG, Nederveen AJ, Krediet CTP. A tri-exponential model for intravoxel incoherent motion analysis of the human kidney: in silico and during pharmacological renal perfusion modulation. Eur J Radiol 2017;91:168-74.

41. Niendorf T, Dijkhuizen RM, Norris DG, van Lookeren Campagne M, Nicolay K. Biexponential diffusion attenuation in various states of brain tissue: implications for diffusion-weighted imaging. Magn Reson Med 1996;36:847-57.

42. Whittall KP, MacKay AL. Quantitative interpretation of NMR relaxation data. J Magn Reson (1969) 1989;84:134-52.

43. Bjarnason TA, Mitchell JR. AnalyzeNNLS: magnetic resonance multiexponential decay image analysis. J Magn Reson 2010;206:200-4.

44. Wiggermann V, Vavasour IM, Kolind SH, MacKay AL, Helms G, Rauscher A. Non-negative least squares computation for in vivo myelin mapping using simulated multi-echo spin-echo T2 decay data. NMR Biomed 2020;33:e4277.

45. Smouha E, Neeman M. Compartmentation of intracellular water in multicellular tumor spheroids: diffusion and relaxation NMR. Magn Reson Med 2001;46:68-77.

46. Nezamzadeh M. Diffusion time dependence of magnetic resonance diffusion signal decays: an investigation of water exchange in human brain in vivo. MAGMA 2012;25:285-96.

47. Marchand AJ, Hitti E, Monge F, Saint-Jalmes H, Guillin R, Duvauferrier R, Gambarota G. MRI quantification of diffusion and perfusion in bone marrow by intravoxel incoherent motion (IVIM) and non-negative least square (NNLS) analysis. Magn Reson Imaging 2014;32:1091-6.

48. Gao J, Jiang M, Magin RL, Gatto RG, Morfini G, Larson AC, Li W. Multicomponent diffusion analysis reveals microstructural alterations in spinal cord of a mouse model of amyotrophic lateral sclerosis ex vivo. PLoS One 2020;15:e0231598.

49. Gambarota G, Hitti E, Leporq B, Saint-Jalmes H, Beuf O. Eliminating the blood-flow confounding effect in intravoxel incoherent motion (IVIM) using the non-negative least square analysis in liver. Magn Reson Med 2017;77:310-7.

50. Wong SM, Backes WH, Drenthen GS, Zhang CE, Voorter PHM, Staals J, van Oostenbrugge RJ, Jansen JFA. Spectral diffusion analysis of intravoxel incoherent

motion MRI in cerebral small vessel disease. J Magn Reson Imaging 2020;51:1170-80.

51. Liu J, Gambarota G, Shu H, Jiang L, Leporq B, Beuf O, Karfoul A. On the identification of the blood vessel confounding effect in intravoxel incoherent motion (IVIM) Diffusion-Weighted (DW)-MRI in liver: an efficient sparsity based algorithm. Med Image Anal 2020;61:101637.

52. Keil VC, Madler B, Gielen GH, Pintea B, Hiththetiya K, Gaspranova AR, Gieseke J, Simon M, Schild HH, Hadizadeh DR. Intravoxel incoherent motion MRI in the brain: Impact of the fitting model on perfusion fraction and lesion differentiability. J Magn Reson Imaging 2017;46:1187-99.

53. Lawson CL, Hanson RJ. Solving least squares problems. Englewood Cliffs: Prentice-Hall, 1974.

54. Golub GH, Heath M, Wahba G. Generalized cross-validation as a method for choosing a good ridge parameter. Technometrics 1979;21:9.

55. Friedli I, Crowe LA, Berchtold L, Moll S, Hadaya K, de Perrot T, Vesin C, Martin PY, de Seigneux S, Vallee JP. New magnetic resonance imaging index for renal fibrosis assessment: a comparison between diffusion-weighted imaging and T1 mapping with histological validation. Sci Rep 2016;6:30088.

56. Chen PS, Li YP, Ni HF. Morphology and evaluation of renal fibrosis. Adv Exp Med Biol 2019;1165:17-36.

57. Hauge A, Wegner CS, Gaustad JV, Simonsen TG, Andersen LMK, Rofstad EK. Diffusion-weighted MRI-derived ADC values reflect collagen I content in PDX models of uterine cervical cancer. Oncotarget 2017;8:105682-91.

58. Andersson CA, Bro R. The N-way Toolbox for MATLAB. Chemom Intell Lab Syst 2000;52:5.

59. Aja-Fernandez S, Niethammer M, Kubicki M, Shenton ME, Westin CF. Restoration of DWI data using a Rician LMMSE estimator. IEEE Trans Med Imaging 2008;27:1389-403.

60. Veraart J, Novikov DS, Christiaens D, Ades-Aron B, Sijbers J, Fieremans E. Denoising of diffusion MRI using random matrix theory. Neuroimage 2016;142:394-406.

61. Wang H, Zheng R, Dai F, Wang Q, Wang C. High-field mr diffusion-weighted image denoising using a joint denoising convolutional neural network. J Magn Reson Imaging 2019;50:1937-47.

62. De Wardener HE. The kidney: an outline of normal and abnormal structure and function. 4th ed. Edinburgh & New York: Churchill Livingstone, 1973.

63. DeLong ER, DeLong DM, Clarke-Pearson DL.

75

Comparing the areas under two or more correlated receiver operating characteristic curves: a nonparametric approach. Biometrics 1988;44:837-45.

64. Robin X, Turck N, Hainard A, Tiberti N, Lisacek F, Sanchez JC, Muller M. pROC: an open-source package for R and S+ to analyze and compare ROC curves. BMC Bioinformatics 2011;12:77.

65. Sachs MC. plotROC: a tool for plotting ROC curves. J Stat Softw 2017;79:2.

66. Lopez-Raton M, Rodriguez-Alavarz MX, Cadarso Suarez C, Gude-Sampedro F. OptimalCutpoints: An R Package for Selecting Optimal Cutpoints in Diagnostic Tests. J Stat Softw 2014;61:1-36.

67. De Luca A, Leemans A, Bertoldo A, Arrigoni F, Froeling M. A robust deconvolution method to disentangle multiple water pools in diffusion MRI. NMR Biomed 2018;31:e3965.

68. Siemens-Healthineers. Embrace human nature at 3T MAGNETOM Vida with BioMatrix. 2020. Available online: https://static.healthcare.siemens.com/siemens_hwem-hwem_ssxa_websites-context-root/wcm/idc/groups/public/@global/@imaging/@mri/documents/download/mda5/nzgw/~edisp/siemens_healthineers_mr_magnetom_vida-07268000.pdf (Accessed November 14th 2020).

69. U.S. Food & Drug Administration. 2020. Available online: https://www.accessdata.fda.gov/cdrh_docs/pdf20/K201615.pdf (Accessed November 22th 2020).

70. Wu Y, Zhu YJ, Tang QY, Zou C, Liu W, Dai RB, Liu X, Wu EX, Ying L, Liang D. Accelerated MR diffusion tensor imaging using distributed compressed sensing. Magn Reson Med 2014;71:763-72.

71. Zhang C, Arefin TM, Nakarmi U, Lee CH, Li H, Liang D, Zhang J, Ying L. Acceleration of three-dimensional diffusion magnetic resonance imaging using a kernel low-rank compressed sensing method. Neuroimage 2020;210:116584.

72. Jensen JH, Helpern JA, Ramani A, Lu H, Kaczynski K. Diffusional kurtosis imaging: the quantification of non-gaussian water diffusion by means of magnetic resonance imaging. Magn Reson Med 2005;53:1432-40.

73. Pentang G, Lanzman RS, Heusch P, Müller-Lutz A, Blondin D, Antoch G, Wittsack HJ. Diffusion kurtosis imaging of the human kidney: a feasibility study. Magn Reson Imaging 2014;32:413-20.

74. Huang Y, Chen X, Zhang Z, Yan L, Pan D, Liang C, Liu Z. MRI quantification of non-Gaussian water diffusion in normal human kidney: a diffusional kurtosis imaging study. NMR Biomed 2015;28:154-61.

10. Curriculum Vitae (CV)

My curriculum vitae does not appear in the electronic version of my paper for reasons of data protection.

My curriculum vitae does not appear in the electronic version of my paper for reasons of data protection.

My curriculum vitae does not appear in the electronic version of my paper for reasons of data protection.

11. List of Publications

Original peer-reviewed publications

1.   **Periquito J**, Gladytz T, Millward J, Ramos P, Cantow K, Grosenick D, Hummel L, Anger A, Zhao K, Seeliger E, Pohlmann A, Waiczies S, Niendorf T. Continuous Diffusion Spectrum Computation for Diffusion Weighted MRI of the Kidney Tubule System. QIMS (accepted)

2.   **Periquito J**, Paul K, Huelnhagen T, Ku K, Ji Y, Cantow K, Gladytz T, Grosenick D, Flemming B, Seeliger E, Waiczies S, Niendorf T, Pohlmann A. Diffusion-weighted Renal MRI at 9.4 Tesla Using RARE to Improve Anatomical Integrity. Sci Rep 2019; https://doi.org/10.1038/s41598-019-56184-6

3.   Ljimani A, Caroli A, Laustsen C, Francis S, Mendichovszky IA, Bane O, Nery F, Sharma K, Pohlmann A, Dekkers IA, Vallee J-P, Derlin K, Notohamiprodjo M, Lim RP, Palmucci S, Serai SD, **Periquito J**, Wang ZJ, Froeling M, et al. Consensus-based Technical Recommendations for Clinical Translation of Renal Diffusion-weighted MRI. Magn Reson Mater Physics, Biol Med. 2019 Nov 1; https://doi.org/10.1007/ s10334-019-00790-y

4.   Waiczies S, Rosenberg JT, Kuehne A, Starke L, Delgado PR, Millward JM, Prinz C, **dos Santos Periquito J**, Pohlmann A, Waiczies H, Niendorf T. Fluorine-19 MRI at 21.1 T: Enhanced Spin–lattice Relaxation of Perfluoro-15-crown-5-ether and Sensitivity as Demonstrated in Ex Vivo Murine Neuroinflammation. Magn Reson Mater Physics Biol Med. 2018 Nov 12; DOI: 10.1007/s10334-018-0710-z

5.   Pohlmann A, Cantow K, Huelnhagen T, Grosenick D, **dos Santos Periquito J**, Boehmert L, Gladytz T, Waiczies S, Flemming B, Seeliger E, Niendorf T. Experimental MRI Monitoring of Renal Blood Volume Fraction Variations en Route to Renal Magnetic Resonance Oximetry. Tomography 2017, 3(4):188–200

6.   Winter L, Oezerdem C, Hoffmann W, Lindt T, **Periquito J**, Ji Y, Ghadjar P, Budach V, Wust P, Niendorf T. Thermal magnetic resonance: physicsconsiderations and electromagnetic field simulations up to 23.5 Tesla (1GHz). Radiation Oncology 2015; DOI 10.1186/s13014-015-0510-9

12. Acknowledgments